MASSACHUSETTS INSTITUTE OF TECHNOLOGY
CENTER FOR SPACE RESEARCH
CAMBRIDGE, MASSACHUSETTS 02139-4307

Final report for NAGW-1841
"Astronomy In the Region Between 1mm and 0.1 mm Wavelength"

May 25, 1994

The research under this grant resulted in the measurement of anistotropy of the Cosmic Microwave Background Radiation (CMBR) on angular scales from 90 degrees to 0.3 degrees. A bolometric radiometer was built with a sensitivity of better than 500 $\mu K/\sqrt{Hz}$.

The measurements complement the COBE anisotropy measurement in two ways. The large scale measurements were shown to cross-correlate with the COBE DMR anisotropy detection, confirming the results. The small scale measurements further the understanding of the structure in the CMBR on scales where we can begin to model the early stages in galaxy and galaxy cluster formation.

No patented inventions were created under this grant.

Papers published in refereed journals are listed here.

1. "A large-Scale Cosmic Microwave Background Anisotropy Measurement At Millimeter and Submillimeter Wavelengths" L. A. Page, E. S. Cheng and S. S. Meyer. (1990) Ap. J. Lett. 355:L1

2. " A Measurement of the Large-Scale Cosmic Microwave Background Anisotropy at 1.8 Millimeter Wavelength" S. Meyer, E. Cheng and L. Page (1991) Ap J. Lett 371:L7

3. "Resonant Cryogenic Chopper" L. Page, E. Cheng and S. Meyer (1992) Appl. Optics 31,95

4. " Cross-Correlation Survey Map and the *COBE* Differential Microwave Radiometer First-Year Maps" (1993) Ap J. Lett. 410,L57

5. "Millimeter-submillimeter m" L. Page, E. Cheng, B Golubovic, J Gundersen, and S. Meyer (1994) Appl. Optics 33,11

6. " A Measurement of the Medium-Scale Anisotropy in the Cosmic Microwave Background Radiation" E. Cheng, C. Cottingham, D. Fixsen, C. Inman, M. Kowitt, S. Meyer, L. Page J. Puchalla, R. Silverberg (1994) Ap J. Lett 422,L37

7. " The Amplitude and Spectral Index of the Large Angular Scale Anisotropy in the Cosmic Microwave Background Radiation" K. Ganga, L.Page, E. Cheng, S. Meyer (1994 accepted) Ap J. Lett

THE ASTROPHYSICAL JOURNAL, 355:L1–L4, 1990 May 20

A LARGE-SCALE COSMIC MICROWAVE BACKGROUND ANISOTROPY MEASUREMENT AT MILLIMETER AND SUBMILLIMETER WAVELENGTHS

LYMAN A. PAGE, EDWARD S. CHENG, AND STEPHAN S. MEYER
Massachusetts Institute of Technology
Received 1989 December 26; accepted 1990 March 2

ABSTRACT

We report on a balloon-borne experiment to measure the anisotropy of the cosmic microwave background (CMB) radiation at angular scales of $\geq 4°$. The instrument simultaneously measures in four spectral bands centered on 5.6 (1.8), 8.7 (1.1), 15.8 (0.63), and 22.5 (0.44) cm^{-1} (mm). We present three results: (1) the 95% confidence limit for monochromatic anisotropies is $\Delta T/T \leq 1 \times 10^{-4}$ on angular scales of 10°; (2) the Galactic plane dust emission at $l = 42°$ is consistent with a ν^2 emissivity law at frequencies above 15 cm^{-1}; below 15 cm^{-1}, we detect excess emission; and (3) atmospheric ozone at an altitude of 35 km may form clumps as large as Δ emissivity/emissivity = 0.002.

Subject headings: cosmic background radiation — interstellar: grains

I. INTRODUCTION

Measurements of the anisotropy of the cosmic microwave background (CMB) radiation at angular scales $\geq 3°$ have the potential for providing the most model-independent view of the structure of the early universe. Foreground emission of both Galactic and zodiacal origin make data on these large angular scales difficult to analyze at sensitivity levels of $\Delta T/T \leq 10^{-5}$ mainly because the spatial and spectral characteristics of these foreground sources are not known to the necessary accuracy. Galactic dust emission is nearly unexplored off the Galactic plane at frequencies below the *Infrared Astronomical Satellite* (*IRAS*) 100 μm band, although it is known to exist and may ultimately limit the sensitivity of CMB anisotropy measurements. Despite the increased Galactic foreground, millimeter wavelength measurements are essential because they offer the possibility of observing the Planckian nature of CMB anisotropies.

We have built and flown a new balloon-borne instrument which simultaneously measures celestial radiation in four passbands, labeled 1 through 4, centered on 5.6, 8.7, 15.8, and 22.5 cm^{-1} respectively (Fig. 1; Table 1). The two high-frequency passbands measure Galactic dust emission, while the two low-frequency bands measure predominantly the CMB. Combined, the four are optimized to permit the separation of dust from CMB emission. We report here on the first flight of the instrument which, while of short duration, did observe the Galaxy and can place limits on the CMB anisotropy.

II. APPARATUS

The instrument input beam is formed by a thermally stable lens-cone system (Collares-Periera, Rabl, and Winston 1977) cooled below 20 K (Page, Cheng, and Meyer 1990). An ambient temperature radiation shielding horn, outside the main beam, improves the side lobe rejection, and an aluminum ground screen further shields the experiment from Earth's radiation. The beam has a 3°.7 FWHM. The optical throughput of the system is 0.5 cm^2 sr.

A cryogenic mechanical chopper operating at 4.5 Hz modulates the radiation on the detectors, alternately illuminating them with the sky and then an internal reference load. The temperature of the internal load is set to nearly null the signal. Each detector output is chopper-synchronously sampled with four integrated samples per cycle. Demodulation is performed on the ground.

The four passbands are determined by a system of dichroic and band-defining filters. The latter are of resonant mesh double-halfwave design (Cunningham 1983). High-frequency, out-of-band radiation is blocked by 28.6, 13.2, 3.2, and 3.2 mm of Fluorogold in channels 1, 2, 3, and 4, respectively. After the flight, we discovered that Fluorogold is a good blocker only up to 100 cm^{-1} (Halpern 1983); at higher frequencies it has some transmission windows. Each detector is a monolithic silicon bolometer (Downey *et al.* 1984) cooled to 0.24 K with a pumped ^{3}He refrigerator. A typical NEP is 3×10^{-16} W $Hz^{-1/2}$; the sensitivities are given in Table 1.

III. OBSERVATIONS AND DATA REDUCTION

The gondola was launched from the NSBF base in Fort Sumner, New Mexico on 1988 October 15. Hanging 370 m below the balloon at an altitude of 35 km, the instrument observes at a 45° zenith angle while scanning continuously in azimuth at two revolutions per minute. The zenith position for this flight is $\alpha = 21^h.69$, $\delta = 34°.3$ ($l = 84°.6$, $b = -14°.0$) with positional accuracy of $\pm 1°$. Due to a balloon failure, only 8.7 minutes of astrophysical data and one calibration were obtained.

a) *Instrumental and Atmospheric Effects*

The detectors are sensitive to cosmic rays which deposit energy in the bolometers resulting in thermal spikes. The spikes are found by searching for points at more than 4 σ from the local average. These points were replaced by the average of the two nearest points. About 30 of the 2336 points per channel were replaced in this way.

The demodulated signal consists of a celestial part and an instrumental-atmospheric part. The latter is a function of time and is modeled separately for each channel as

$$S_i(t) = a_0 + a_1 t + a_2 p(t) + a_3 \Theta_z(t) p(t) ,$$

where $S_i(t)$ is the atmospheric-instrumental signal, a_0, a_1, a_2, and a_3 are fit parameters, t is the time, and $p(t)$ is the atmospheric pressure as measured by an onboard pressure sensor.

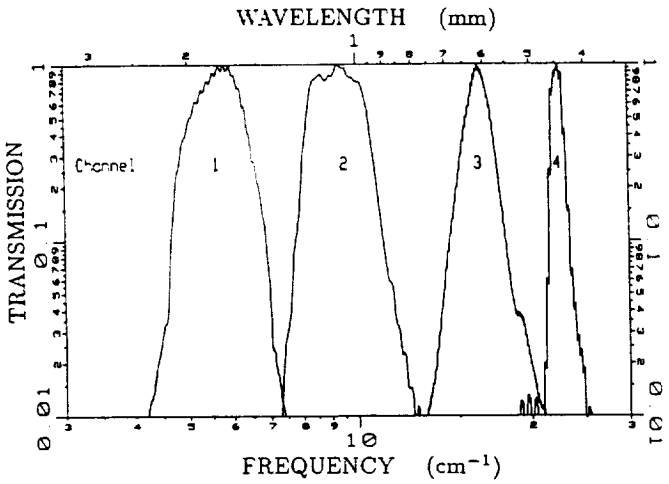

FIG. 1.—The measured normalized spectral response of the four passbands to a Rayleigh-Jeans source. The bands are determined by a system of high-frequency blocking, dichroic, and double-halfwave band-defining filters.

Changes in zenith angle, $\Theta_z(t)$, cause changes in the atmospheric contribution. For this flight, the variations were $\sim 0.^{\circ}4$ rms. Data from a three-axis magnetometer are used to construct a kinematic model of the gondola motion. The residuals to the model are $\sim 0.^{\circ}06$ rms, a result limited by the digitization noise in the magnetometer signal.

$S_i(t)$ is subtracted from the raw signal and the result is binned in azimuth, *az*. The average and standard deviation of the signal in each bin is plotted in Figure 2. None of the channels are limited by detector noise in this flight. Channel 1 is limited by the digitization noise; channel 2 developed microphonic problems soon after launch; and channels 3 and 4 are limited by the residuals in the zenith angle model.

b) Zodiacal Emission and High-Frequency Leakage

The large signal in channels 3 and 4 between $az \sim 60°$ and $az \sim 290°$ is high-frequency leakage of the zodiacal dust emission (ZDE). The expected signal is ~ 30 times less (Halpern *et al.* 1988). We skim the ecliptic, $\beta = 0° \pm 1.^{\circ}5$, from azimuth $az = 132°$, elongation $El = 154°$ to $az = 174°$, $El = 124°$. In the bottom panel of Figure 2, we show the 25 μm *IRAS* data, which is mostly ZDE, for our sky coverage. We have searched for evidence of leakage in the two low-frequency channels

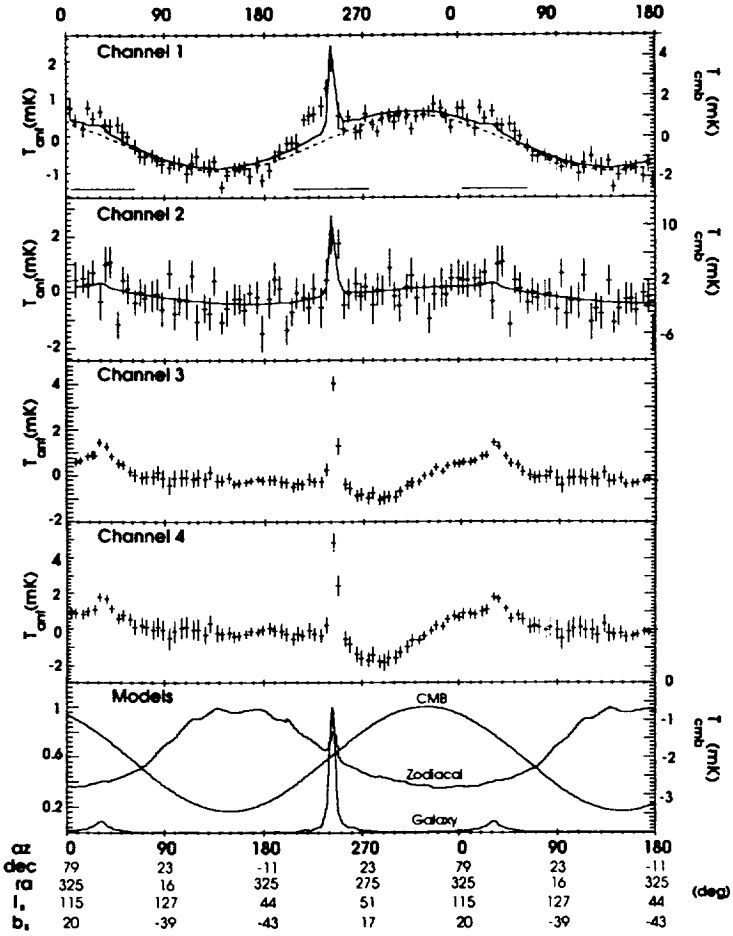

FIG. 2.—The first four panels show the rotation-averaged signals of the four channels. The left ordinate is the antenna temperature and for channels 1 and 2, and the right ordinate is the thermodynamic temperature for a 2.74 K emitter. The solid line in the top two panels is the fit to a galaxy-plus-dipole model. For channel 1, the dashed line is the best-fit dipole found by excluding data within 20° (marked by the solid horizontal bars) of the Galactic plane. The three dominant sources of astrophysical radiation in our frequency range for our beam path are shown in the bottom panel. Both the Galactic and zodiacal contributions are normalized to 1. The Galactic term is the *IRAS* data with the zodiacal component removed (Boulanger 1989); the zodiacal term is taken as the 25 μm *IRAS* data. Both have been convolved with our beam shape. The CMB dipole is from Boughn *et al.* (1989); its ordinate is on the right. The zero point for this scale is set so that $T_{CMB} = 0$ on the dipole equator.

TABLE 1

PASSBAND AND DETECTOR CHARACTERISTICS

	Effective Frequency and Bandwidth[a] (cm^{-1})		Detector Sensitivity[b] ($\mu K\ Hz^{-1/2}$)		Fraction of Total Atmospheric Emission[c]			Achieved Observational Sensitivity[d] ($mK\ s^{1/2}$)	
Channel (1)	$\langle\nu\rangle$ (2)	$\Delta\nu$ (3)	Antenna (4)	CMB (5)	H_2O (6)	O_2 (7)	O_3 (8)	Antenna (9)	CMB (10)
1.....	5.6	1.2	160	300	0.11	0.02	0.87	0.6	1.1
2.....	8.7	1.7	78	270	<0.005	<0.005	1.0	2.8	9.5
3.....	15.8	1.8	12	660	0.08	0.18	0.74	0.6	30.
4.....	22.5	1.3	76	...	0.01	0.01	0.98	1.3	...

[a] The effective frequency is $\langle\nu\rangle = \int \nu B(\nu, T)\tau(\nu)d\nu / \int B(\nu, T)\tau(\nu)d\nu$, and effective bandwidth is $\Delta\nu = \int B(\nu, T)\tau(\nu)d\nu / B(\langle\nu\rangle, T)$, where $\tau(\nu)$ is the spectral response function. For $T > 5$ K, both $\langle\nu\rangle$ and $\Delta\nu$ are independent of Planck temperature to $< 5\%$.

[b] The radiation NET as derived from the radiation responsivity and laboratory voltage noise.

[c] Derived from an atmosphere model and passbands.

[d] The radiation NET achieved during the flight referenced to a 1 s integration on the sky. This number includes the contribution from zenith angle uncertainty.

using a model of the ZDE. Both channels are consistent with no leakage.

c) *Calibration*

The instrument is calibrated in flight by placing a piece of Mylar into the beam. The geometry is arranged so that both reflected and transmitted radiation come from the sky at a 45° zenith angle. The calibration signal, amounting to $T_{ant} \sim 0.2$ K in channels 1 and 2, is referenced to the known temperature and emissivity of the plastic. The uncertainty in our current laboratory measurement of Mylar's emissivity at low frequencies limits the usefulness of this method for channel 1. For purposes of analyzing this flight, it is calibrated using the CMB dipole.

Because channels 3 and 4 exhibit clear signs of high-frequency leakage, some of the calibration signal could be due to out-of-band radiation. Upper limits on the calibration error were obtained in the laboratory by replacing the input optics with an internal blackbody load. The final calibration errors in channels 2, 3, and 4 are ±20%, +35%/−25%, and +50%/−30%, respectively.

Channel 1 is calibrated using the CMB dipole. A fit is made to $b_0 + b_1 \sin(az) + b_2 \cos(az)$ for data with $|b| > 20°$. The χ^2 is 48 for 40 degrees of freedom. Boughn *et al.* (1989) (see also Lubin *et al.* 1985, which additionally contains an all-sky determination of the CMB dipole) give a CMB dipole of $T_{\rm CMB\ dipole} = 3.3$ mK ± 3% in the direction $\alpha = 11^h.03$ and $\delta = -5°.82$ with a pointing accuracy of ±2°. After correcting for Earth's orbital velocity, the azimuth of the warmest point for our sky coverage is expected to be $az = 301° \pm 2°$, our fit to b_1 and b_2 gives $az = 310° \pm 3°.5$. The resulting total calibration error in channel 1 is 11% for thermal emitters at 2.7 K and 16% for Rayleigh-Jeans emitters (the additional error is the result of uncertainties in the passband shape).

IV. RESULTS

a) *Atmosphere*

The zenith antenna temperature of the atmosphere at 35 km (4.3 torr pressure) is $T_{ant} = 67$, 130, 500, and 800 mK in channels 1–4, respectively. The signal from the 0°.4 zenith angle fluctuations is $T_{ant} = 0.65$, 1.3, 5.0, and 7.9 mK for channels 1–4. Ozone emission dominates in all the channels. Table 1 shows the proportions of atmospheric emission in each passband as determined from a model (Weiss 1980).

Figure 2 shows a strong source in channels 3 and 4 between $az = 300°$ and $az = 45°$. The spectrum of the source is consistent with ozone and would constitute a fluctuation of $\Delta\epsilon_{O_3}/\epsilon_{O_3} = 0.002$, where ϵ_{O_3} is the emissivity of the ozone column. Preliminary analysis of a subsequent flight in 1989 October is not consistent with the strength of this source, confirming its atmospheric origin. At the same position, Owens, Muehlner, and Weiss (1979) report a "northern spur," but because of the strength of the ozone we cannot substantiate their source.

b) *Cosmic Microwave Background*

The residuals to the channel 1 dipole fit (Fig. 3) are analyzed for anisotropy using a likelihood ratio test (Lawrence, Readhead, and Myers 1988 and Cottingham 1987). We test the hypothesis that variations in the CMB are described by a monochromatic correlation function, that is $\langle T(\vartheta, \varphi)T(\vartheta', \varphi')\rangle = (\Delta T)^2 P_L \cos(\theta)$, where θ is the angle between the two

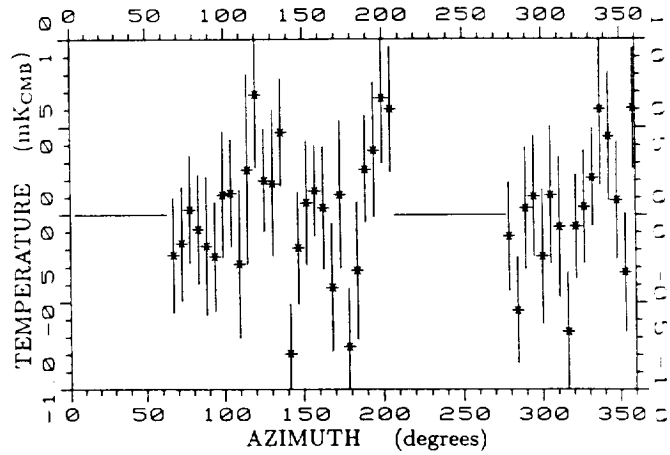

FIG. 3.—The residuals of the dipole fit to the channel 1 rotation average. These data are analyzed for CMB anisotropy. The blank regions were excluded from the fit due to the proximity of the Galaxy. The ordinate is in thermodynamic temperature relative to a 2.74 K Planck emitter; the zero point is arbitrary.

sky positions and P_L is the Legendre polynomial with mode L. against the hypothesis that the CMB is isotropic. The correlation length is $\theta_C = [2/L(L+1)]^{1/2}$. As is customary, we test at the 95% confidence level. Our best limit is $\Delta T/T \leq 9.3 \times 10^{-5}$ (power = 0.7) at mode $L = 8$; for $L = 3$ to $L = 11$, $\Delta T/T \leq 1.25 \times 10^{-4}$.

c) *Galaxy*

The scan crossed the Galaxy at $l = 42°$ ($az = 243°$) and $l = 128°$ ($az = 33°$). Only the $l = 42°$ plane crossing is analyzed here. The Galactic plane width in channel 1 is clearly broader than in the other channels. We have not found the cause of this signal and have made a preliminary check of the data from the new flight in 1989 October. While the strength of the Galaxy crossing in the new flight is consistent with that reported here, the broad shoulder centered on $az = 220°$ is not present in the new data. The Galaxy signal at $l = 42°$ is $T_{ant} = 2.6 \pm 0.7$, 3.1 ± 1.4, $3.0^{+1.4}_{-1.5}$, and $5.4^{+3.6}_{-3.2}$ mK in channels 1–4. These correspond to $\nu I(\nu)$ of 3.6×10^{-13}, 1.6×10^{-12}, 9.9×10^{-12}, and 5.5×10^{-11} W cm^{-2} sr^{-1}. Statistical, calibration, and high-frequency leakage errors are included in the error bounds.

Channels 1 and 2 are fitted to a four-parameter model consisting of an offset, a sinusoid (the CMB dipole), and a model of the Galaxy: $c_0 + c_1 \sin(az) + c_2 \cos(az) + c_3 G(az)$, where $G(az)$ is the *IRAS* 100 μm data with the ZDE removed (Boulanger 1989) and convolved with our beam profile. Channels 3 and 4, while containing no appreciable CMB dipole, are affected by ZDE from the high-frequency leakage and by atmospheric signals. To obtain the antenna temperature at the Galactic plane crossing for channels 3 and 4, a linear baseline referenced at $az = 210°$ and $az = 280°$ is subtracted from the data in Figure 2. The high-frequency leakage in channels 3 and 4 is estimated by comparing the ZDE emission to the Galactic dust emission in the *IRAS* 25 μm band. Upper bounds on the leakage are 0.4 and 0.8 mK for channels 3 and 4, respectively.

A simple dust model of the Galaxy with the specific intensity given by $I(\nu) = \epsilon_0 \nu^2 B(\nu, T_{dust})$, where B is the Planck function and ν is the frequency, is fitted to channels 3 and 4 along with other observers' data (Fig. 4). All the data are for $l = 42°$ and have been adjusted for our beam size. The best-fit dust parameters are $T_{dust} = 22.1 \pm 0.7$ K and $\epsilon_0 = 1.1 \times 10^{-6}(1/\text{cm}^{-1})^2$.

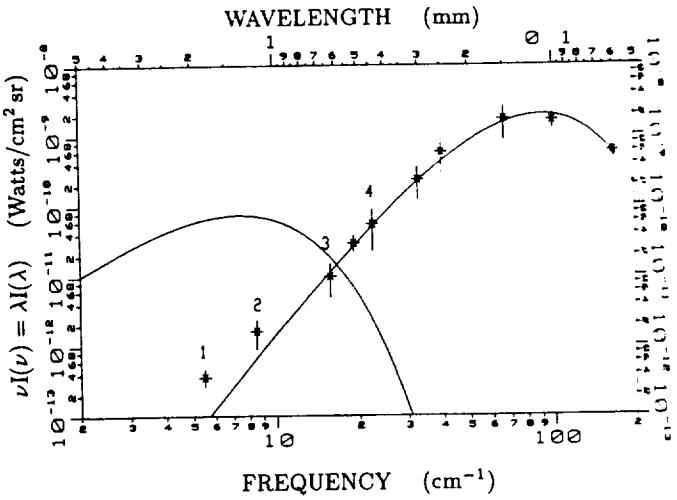

FIG. 4.—Galactic emission at $b = 0°$ and $l = 42°$. Our data are marked with the channel numbers; the point between channels 3 and 4 is from Owens *et al.* (1979). The three points after channel 4 are from Hauser *et al.* (1984). The points at 100 μm and 60 μm are from the *IRAS* data (Boulanger 1989 and Sodroski *et al.* 1987, respectively). All data are averaged to our beam size and the Owens *et al.* (1979) effective frequency recomputed for this emission model. The curve which peaks at 100 cm^{-1} is a ν^2 dust emission model with $T_{dust} = 22.1$ K and $\epsilon_0 = 1.1 \times 10^{-6}(1/\text{cm}^{-1})^2$. The spectrum of the CMB (shown as a 2.74 K Planck emitter) is plotted for reference.

Channels 1 and 2 show excess emission over what would be expected from a simple extrapolation of the high-frequency data. Pajot *et al.* (1986, 1989) observe a similar excess at 11 cm^{-1} nearer the center of the Galaxy. The free-free emission at 5.6 cm^{-1} may be estimated with a $\nu^{-0.1}$ extrapolation of the 4.875 GHz data of Altenhoff *et al.* (1978). After averaging over our beam, the result is $\nu I(\nu) \approx 3 \times 10^{-15}$ W cm^{-2} sr^{-1}, far too little to explain the excess. If the excess were produced by a second colder ν^2 dust emitter, its parameters would be $T_{dust} \sim 4$ K and $\epsilon_0 \sim 4 \times 10^{-5}(1/\text{cm}^{-1})^2$. This is an uncomfortably low temperature and high column density but is consistent with the data of Lubin *et al.* (1985) at 90 GHz. A more plausible interpretation of the low-frequency excess is that there are dust grains with nonspherical geometries (for example, needles [Wright 1982] or fractals [Wright 1987]) or that the grains have an enhanced emissivity at low frequencies (for example, > 1 μm graphite grains; Draine and Lee 1984, Fig. 4*b*).

We thank Boris Golubovic, Josh Gunderson, James King, Mark Lim, and Jennifer Sokolowski for devoting a great deal of time to this project. We thank François Boulanger for providing the 100 μm *IRAS* data with the zodiacal light removed. We are grateful for many enlightening discussions with Rai Weiss and David Cottingham. One of us (L. P.) was supported by a NASA GRSP fellowship. This work was partially supported by NASA grant NGR 22-009-526.

REFERENCES

Altenhoff, W. J., Downes, D., Pauls, T., and Schraml, J. 1978, *Astr. Ap. Suppl.*, **35**, 23.
Boughn, S. P., Cheng, E. S., Cottingham, D. A., Fixsen, D. J., and Wilkinson, D. T. 1989, *Ap. J.*, submitted.
Boulanger, F. 1989, private communication.
Collares-Periera, M., Rabl, A., and Winston, R. 1977, *Appl. Optics*, Vol. **16**, No. 10, p. 245.
Cottingham, D. A. 1987, Ph.D. thesis, Princeton University.
Cunningham, C. T. 1983, *Infrared Phys.*, Vol. **23**, No. 4, p. 207.
Downey, P. M., *et al.* 1984, *Appl. Optics*, **23**, Vol. No. 6, p. 910.
Draine, B. T., and Lee, H. M. 1984, *Ap. J.*, **285**, 89.
Halpern, M. 1983, Ph.D. thesis, Massachusetts Institute of Technology.
Halpern, M., Benford, R., Meyer, S. S., Muehlner, D., and Weiss, R. 1988, *Ap. J.*, **332**, 596.
Hauser, M. G., Silverberg, R. F., Stier, M. T., Kelsal, T., Gezari, D. Y., Dwek, E., Walser, D., and Mather, J. C. 1984, *Ap. J.*, **285**, 74.
Lawrence, C. R., Readhead, A. C. S., and Myers, S. T. 1988, in *The Post-Recombination Universe*, ed. N. Kaiser and A. N. Lasenby (Dordrecht: Kluwer), p. 173.
Lubin, P., Villela, T., Epstein, G., and Smoot, G. 1985, *Ap. J. (Letters)*, **298**, L1.
Owens, D. K., Muehlner, D. J., and Weiss, R. 1979, *Ap. J.*, **231**, 702.
Page, L. A., Cheng, E. S., and Meyer, S. S. 1990, in preparation.
Pajot, F., *et al.* 1986, *Astr. Ap.*, **154**, 55.
Pajot, F., *et al.* 1989, preprint.
Sodroski, T. J., Dwek, E., Hauser, M. G., and Kerr, F. J. 1987, *Ap. J.*, **322**, 101.
Weiss, R. 1980, *Ann. Rev. Astr. Ap.*, **18**, 489.
Wright, E. L. 1982, *Ap. J.*, **255**, 401.
———. 1987, *Ap. J.*, **320**, 818.

EDWARD S. CHENG: Code 685, Goddard Space Flight Center, Greenbelt MD 20771

STEPHAN S. MEYER and LYMAN A. PAGE: Room 20F-001, Department of Physics, Massachusetts Institute of Technology, Cambridge, MA 02139

THE ASTROPHYSICAL JOURNAL, 371:L7–L9, 1991 April 10

A MEASUREMENT OF THE LARGE-SCALE COSMIC MICROWAVE BACKGROUND ANISOTROPY AT 1.8 MILLIMETER WAVELENGTH

STEPHAN S. MEYER, EDWARD S. CHENG,[1] AND LYMAN A. PAGE
Room 20F-001, Department of Physics, Massachusetts Institute of Technology, Cambridge, MA 02139
Received 1990 October 29; accepted 1991 January 22

ABSTRACT

This measurement of the large-scale cosmic microwave background radiation (CMBR) anisotropy places the most stringent constraints to date on fluctuations in the CMBR on angular scales greater than $\sim 4^\circ$. Using a four-channel bolometric radiometer operating at 1.8, 1.1, 0.63, and 0.44 mm, the diffuse sky brightness over half of the northern hemisphere has been mapped with an angular resolution of 3°.8. Analysis of the sky map at the longest wavelength for Galactic latitudes $|b| \geq 15^\circ$ yields a 95% confidence level upper limit on fluctuations of the CMBR at $\Delta T/T \leq 1.6 \times 10^{-5}$ with a statistical power of 92% for Gaussian fluctuations at a correlation angle of 13°. Between 3° and 22°, the upper limit of fluctuations is $\Delta T\ T \leq 4.0 \times 10^{-5}$ (95% confidence level). An anisotropy is detected in the map, but it cannot yet be attributed to primordial sources. The ultimate sensitivity for this experiment is $\Delta T/T \sim 7 \times 10^{-6}$ (95% confidence level) over this angular range for Gaussian fluctuations.

Subject headings: cosmic background radiation — cosmology

1. INTRODUCTION

We describe an initial result in a search for cosmic microwave background radiation (CMBR) anisotropy. Following a flight in 1988 October 15 reported in Page, Cheng, & Meyer (1990a), the MIT radiometer (Page, Cheng, & Meyer 1991) has been reflown twice (1989 October 6 and 1990 May 15) with two substantive changes to the instrumentation of the gondola: the addition of a sensitive vertical gyroscope to measure the orientation of the optical axis with respect to the zenith, and the addition of an input blocking filter effective at wavelengths shortward of 20 μm.

The bolometric radiometer has four channels operating at 1.8, 1.1, 0.63, and 0.44 mm wavelength, known as channels 1 through 4, with widths of 0.4, 0.2, 0.07, and 0.03 mm, respectively. The beam FWHM is 3°.8. In channel 1, the sensitivity to variations in the CMBR temperature in the sky is 0.63 mK for each 1 s integration. In this *Letter*, only data from the channel 1 of the 1989 October 6 flight are discussed.

2. OBSERVATIONS

The gondola was launched from the National Scientific Balloon Facility (NSBF) in Fort Sumner, NM on 1989 October 6 at 21:00 UT. Of the 10 hr of data, a total of 2.3×10^4 s were used to produce a map of the sky covering about half the northern hemisphere. The remaining time was devoted to calibration and checking for systemaic errors. At an average altitude of 36.3 km, the gondola rotates in azimuth once per 40 s with the beam at a zenith angle of 44°. During the flight the zenith position changed from $\alpha = 21^h13$, $\delta = 34^\circ.5$ to $\alpha = 3^h.63$, $\delta = 34^\circ.6$. In Galactic coordinates, the map lies within the region from approximately $l = 45^\circ$ to 200° and $b = +60^\circ$ to -80°.

[1] Postal address: Code 685, NASA Goddard Space Flight Center, Greenbelt, MD 20771.

3. DATA REDUCTION

3.1. *Producing the Map*

The data stream in each channel consists of four synchronously integrated samples per 4.5 Hz chopper cycle. Each integration is thus 56 ms in length. The bolometric detectors, sensitive to all forms of thermal power, respond to cosmic rays with a positive spike of variable strength depending on the deposited energy. To remove the spikes, the data are filtered after having the sky contribution subtracted. One second of data is removed for each detected event since the detectors and signal electronics require some time to recover. Roughly 7% of the total data set is removed as a result of cosmic-ray hits.

The data are divided into six 1 hr sections by 12 minute calibration sequences. Each hour of the spike-removed data is digitally high-pass filtered with a cutoff frequency corresponding to two gondola rotations. This removes the drift in the offset which is due to both the changing atmospheric pressure (the gondola altitude varies with a period of about 8 minutes or 12 rotations) and the slow cooling of the input optics. The data are binned into 1°.3 × 1°.3 pixels on the sky. The variance in each sky pixel is minimized by fitting a cubic spline to the time ordered data with one breakpoint for every eight rotations.

The full map of the sky is made by concatenating these 1 hr segments. For the data in channel 1, the best calibration comes from the detection of the CMBR dipole (the dipole is detected in channels 2 and 3 as well). An inflight calibrator is carried on the gondola but is not used in this *Letter*. The high-pass filter has removed the information on the DC level of the signal so the data at Galactic latitudes greater than 15° are fit to a dipole with fixed amplitude and unknown direction. The value of the dipole amplitude is assumed to be 3.3 mK (Cottingham 1990; Lubin et al. 1985; Smoot et al. 1991). There is one multiplicative and one additive fit parameter for each 1 hr segment and two parameters for the direction of the dipole. The 6 hr of data are thus fitted with 14 parameters. The calibration remained constant within 15% over the length of the

flight. The dipole direction, after correcting to the solar frame, is $\alpha = 10^h.68 \pm 0^h.19$ and $\delta = -1°.3 \pm 3°.0$ with the error being dominated by a $\pm 3°$ pointing uncertainty. This can be compared to $\alpha = 11^h.6$ and $\delta = -6°.9$, the average of the dipole results of Cottingham (1990), Lubin et al. (1985), and Smoot et al. (1991).

After removing data with Galactic latitude $|b| \leq 15°$, the map has 3500 pixels each with a temperature and variance. The average error is $\sqrt{\langle \sigma^2 \rangle} = 0.26$ mK, where σ is the standard deviation of the average value in a given pixel determined from the variance of the data samples which fell in the pixel over the 1 hr intervals. The χ^2 of the fit to the dipole is 1.7 per degree of freedom. The statistical probability of this is vanishingly small. The variance in each pixel is 1.2 times what is expected from ground measurements of the radiometer NET indicating no large contribution from residual atmospheric noise.

3.2. *Analysis of Anisotropy*

The map is analyzed for anisotropy using a modified likelihood ratio test. In this initial analysis only Gaussian fluctuation models over a range of correlation angles from 3° to 22° are tested. Following the method and implementation of Cottingham (1987) and Boughn et al. (1990), a statistic, S, is formed which is related to the likelihood ratio, λ of Lawrence, Readhead, & Myers (1988). The calculation of the formal likelihood ratio is intractable for a data set with several thousand correlated points on the sky. The distribution of S is determined with a Monte Carlo simulation of the experiment with the sky coverage, beam profile, and variance in each pixel taken into consideration. For each correlation angle, 300 manifestations of the experiment are created with no CMBR fluctuations and 300 with fluctuations of amplitude η, where η is the total rms fluctuation predicted by a model $\langle T(\Theta_i)T(\Theta_j)\rangle = \eta^2 C(\theta_{ij})$, with the correlation function, C, normalized so that $C(0) = 1$. θ_{ij} is the angle between directions Θ_i and Θ_j. For this analysis the correlation function is Gaussian and the correlation angle is $\theta_0^{-2} = -[(1/c)(d^2C/d\theta^2)]_{\theta=0}$. When $\eta = \eta_0$ is chosen such that the value of S from the Monte Carlo simulations is higher than the observations 95% of the time, then this value is the 95% confidence level upper limit for fluctuations at this correlation angle. The distribution of S, assuming no fluctuations, is used to determine the statistical power of the test, defined as the fraction of this null distribution below S for the data. The values of η_0 are shown in Figure 1 for each tested correlation angle. The power is greater than 90% for each upper limit plotted in Figure 1. Also plotted in Figure 1 is the ultimate sensitivity of the experiment. This is the value $\eta = \eta_s$ for which 95% of the simulations exceed the mean S for the null distribution. In other words, if the sky were isotropic to a level well below the ultimate sensitivity, η_s is the most probable 95% confidence level upper limit this measurement would produce.

The single-frequency map has not been analyzed for a quadrupole anisotropy. The sky coverage, being centered on the Galactic plane and having less than one-quarter sky coverage, is not suitable for solving separately for a dipole and a quadrupole component.

4. DISCUSSION

The reason for the relatively high statistical power of the upper limits at each correlation angle is that the observed map has more structure than is statistically likely. This can be seen from the reduced χ^2 for the fit to the dipole. A value of $\chi^2/\nu = 1.7$ is statistically unlikely. Also, the 95% sensitivity is more than a factor of 2 lower than the upper limits. There is a clear detection of some sort of anisotropy. There are several possible sources: Galactic emission due to high Galactic latitude dust; nonisotropic stationary emission from the atmosphere; systematic errors due either to instrumental effects or Earth in the sidelobes of our beam; and the CMBR. Each of these is discussed below.

Galactic emission at high Galactic latitude is a source which cannot be ruled out with the data at only this one wavelength. The *IRAS* 100 μm map scaled to 1.8 mm using Figure 4 in Page et al. (1990a), suggests structure at the $\Delta T/T_{\rm CMBR} \sim 10^{-5}$ level.

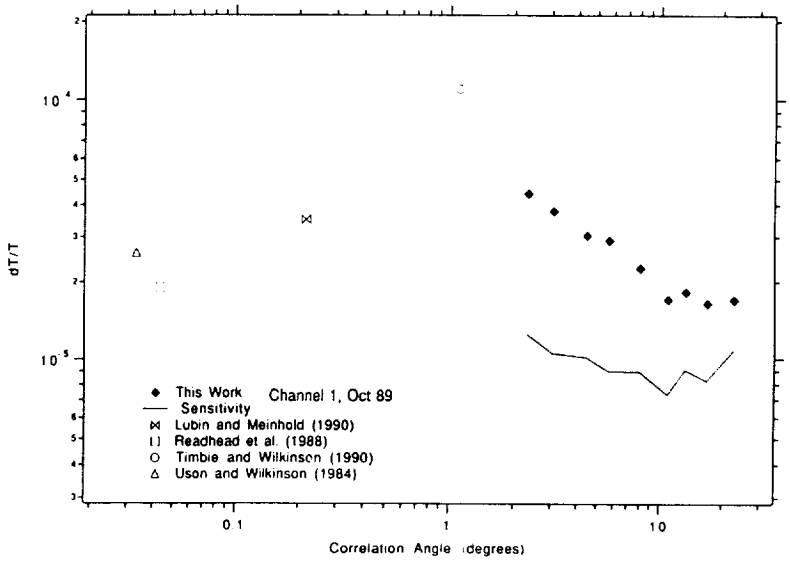

FIG. 1.—The 95% confidence level upper limits for Gaussian fluctuations in the CMBR as a function of correlation angle. The black diamonds are the 95% confidence level upper limits of this work; the line is the sensitivity of this experiment. The statistical power of the test for each of these points is over 90%. Also plotted are published values for the Gaussian limits of others.

Residual atmospheric emission, seen with high signal-to-noise ratio in channel 3, could also give rise to apparent anisotropy. The atmosphere must be stationary over the time of the observation of a pixel (5 minutes at the shortest). Any variation over the time scale of 5 minutes will decrease the sensitivity of the experiment. A residual atmospheric "cloud," stationary in position, could produce the observed signal. In the 1988 October flight, such a cloud was observed. In the first hour of the 1989 October flight, similar clouds were observed; however, after an hour at the observing altitude their contrast diminished considerably.

The instrument has several characteristics which could result in systematic errors. There is a geomagnetic sensitivity due to the magnetic nature of our cryogenic chopper drive (Page, Cheng, & Meyer 1990b). This effect could produce an apparent dipole at a level of ≤ 0.3 mK. Any dipole is subtracted from the map before analysis for anisotropy and could potentially cause a 10% error in the calibration along with a small error in dipole direction. Significant higher moments are not produced by this mechanism. The instrument is also sensitive to gondola swinging which causes a variable observed air mass along the line of sight and also modulates the cryogenic chopper which is not perfectly balanced. The gyroscopes measure this swinging to 1'. To detect the variation of the chopper operation we carefully measure the chopper coil EMF during the flight. Using laboratory calibrations, we can limit the size of the chopper and airmass effects to < 0.03 mK. Diffracted earthshine could produce anisotropy signals. The total brightness of Earth diffracted over the edge of the ground screens is $T_{ant} \sim 6.0$ μK, and only variations in this could produce detected effects. Radiometric contributions from the balloon and ground screen emission are smaller.

The characteristics of the map production have been tested by dividing the full map into two pieces and determining the upper limits for each piece separately. The results were similar to those for the total map but with the sensitivity averaging 1.5 higher for each piece and the 95% confidence level upper limit higher by a few percent. In addition, maps using only 5 of the 6 hr of flight data were made, and the expected results were obtained. From this it is clear that there is no one position on the sky which is giving rise to the detected signal. The algorithms for the detection of anisotropy from the maps have also been tested by forming a simulated map which has the same σ in each pixel and the same sky coverage as the flight data. The simulated map is produced so that the signal is Gaussian-distributed with the correct σ in each pixel. This null map, when fitted to zero, has a $\chi^2 = 0.98$ and produces a very low 95% confidence level upper limit with no statistical power when analyzed in the same manner as the flight data.

Finally, the detected signal or some part of it could be of cosmological origin. A change in the CMBR temperature produces a unique spectral signature in the four channels and can be confirmed by further multispectral analysis. In addition, the 1990 May flight has 30% overlap with the 1989 October flight. This will aid in the separation of atmospheric from CMBR and Galactic sources.

5. CONCLUSIONS

There is clearly some sort of anisotropy in the data at the level of $\Delta T/T = 1\text{–}3 \times 10^{-5}$ at scales greater than 4°. However, reasonable extrapolations of dust emission from the *IRAS* data and previous measurements of the atmosphere suggest that these are possible sources for the signal. Whatever the cause, the upper limit determined from this experiment serves to constrain CMBR anisotropy at new levels. Since these measurements are not limited by instrument sensitivity, further analysis which includes the shorter wavelength data will clarify the origin of the anisotropy.

We wish to thank David Cottingham for many helpful discussions and the use of his routines to analyze the maps for anisotropy. Many people helped in the construction of the instrument. We thank the undergraduate students whose work helped make this flight possible: Michael Chandross, Deborah Dougherty, and Emmin Shung. We thank the National Scientific Balloon Facility for a flawless flight.

L. A. P. was partially supported by a NASA Graduate Student Fellowship. This research was supported by NASA grant NAGW-1841.

REFERENCES

Boughn, S. P., Cheng, E. S., Cottingham, D. A., Fixsen, D. J., and Wilkinson, D. T. 1990, ApJ, submitted
Cottingham, D. A. 1987 Ph.D. thesis, Princeton University
———. 1990, private communication
Lawrence, C. R., Readhead, A. C. S., and Myers, S. T. 1988, in The Post Recombination Universe, ed. N. Kaiser & A. N. Lasenby (Dordrecht: Kluwer), p. 173
Lubin, P., & Meinhold, P. R. 1990, ApJ, submitted
Lubin, P., Villela, T., Epstein, G., & Smoot, G. 1985, ApJ, 298, L1
Page, L. A., Cheng, E. S., & Meyer, S. S. 1990, ApJ, 355, L1
———. 1990b, Appl. Optics, submitted
———. 1991, in preparation
Readhead, A. C. S., Lawrence, C. R., Myers, S. T., Sargent, W. L. W., Hardebeck, H. E., & Moffet, A. T. 1989, ApJ, 346, 556
Smoot, G. F., et al. 1991, ApJ, 371, L1
Timbie, P. T., & Wilkinson, D. T. 1990, ApJ, 353, 140
Uson, J. M., & Wilkinson, D. T. 1984, ApJ, 283, 471

Resonant cryogenic chopper

Lyman A. Page, Edward S. Cheng, and Stephan S. Meyer

We describe the design, construction, and performance of a resonant cryogenic chopper that operates at 4.2 K. The chopper is mechanically and thermally robust; it can occult a 2.54-cm aperture at 4.5 Hz while dissipating ~1 mW. Both the stator and rotor magnetic fields are controllable to allow for performance optimization and to help in measuring any possible interference effects. Data on long-term amplitude stability are presented.

Introduction

A thermally and mechanically stable cryogenic chopper is an indispensable optical component for many infrared and submillimeter radiometers. In these instruments the signal offset and effective gain are functions of the chopper amplitude and temperature. Any variations in these can mask or mimic the desired signal or lead to difficult *post facto* modeling or analysis. In addition chopper motion may microphonically couple to the detectors and introduce undesired noise. We report on the design, construction, and performance of a resonant cryogenic chopper with high-amplitude stability, constant temperature, and low microphonic coupling to the rest of the experiment.

We built and flew a balloonborne far-infrared experiment to measure the anisotropy in the cosmic microwave background radiation[1] by mapping the sky at an angular resolution of ~4° in four spectral bands simultaneously. The chopper, a torsional oscillator, is used to direct radiation alternately from the sky and from a thermal reference source to a set of detectors[2] as indicated in Fig. 1. The detector outputs are synchronously demodulated at the chopping frequency ν_{chop} of 4.5 Hz. Secondary modulation of the radiation from the sky is provided by rotating the experiment at 2 rpm. Therefore we require the chopper amplitude to be stable on time scales of less than a few rotations or ~250 s (0.004 Hz).

The chopper assembly has four major components: (1) a stator to produce a constant magnetic field (Fig. 2); (2) a rotor that makes the alternating magnetic field (Fig. 3); (3) a chopper blade; (4) and a piano wire axle. The rotor and chopper blade are attached to the middle of the piano wire. The chopper completely modulates a 2.54-cm-diameter aperture from an axis that is 3.65 cm away from the optical axis with an amplitude of oscillation of 35°. The dimensions are given in Table I.

Both the stator and rotor magnetic fields are produced by room-temperature current sources. There are no permanent magnets, which allows us to optimize the operating conditions and to ensure that the chopper's magnetic fields are not interfering with the rest of the experiment.

A variety of choppers have been used in other radiometers. Peterson[3] uses a resonant torsional chopper built from a taut-wire meter movement; it can occult a 1-cm aperture at 13 Hz. The principle of operation is similar to the one described in this paper. The major differences are that his stator is a permanent magnet, and the entire assembly is submerged in liquid helium (LHe). Murakami and Lange[4] also use a resonant torsional chopper to occult a 1-cm aperture. It operates in vacuum and at 3.8 Hz. In a manner almost opposite to the chopper described here, the torque is produced by mounting a permanent magnet on the rotor and modulating the stator field. Continuously rotating motors are sometimes used when the chopper blade can be submerged in LHe. With these the size of the blade is almost unlimited, and essentially any frequency can be attained; however, bearing noise is often a problem. In addition, if the blade is not submerged, it cannot be thermally stabilized and it will slowly warm. For higher modulation frequencies (>20 Hz) and small

When the research was performed the authors were with the Department of Physics, Massachusetts Institute of Technology, Room 20F-001, Cambridge, Massachusetts 02139. L. A. Page is now with the Department of Physics, Princeton University, Jadwin Hall, P. O. Box 708, Princeton, New Jersey 08544-0708. E. S. Cheng is with the Goddard Space Flight Center, National Aeronautics and Space Administration, Code 685, Greenbelt, Maryland 20771.

Received 31 July 1990.
0003-6935/92/010095-06$05.00/0.

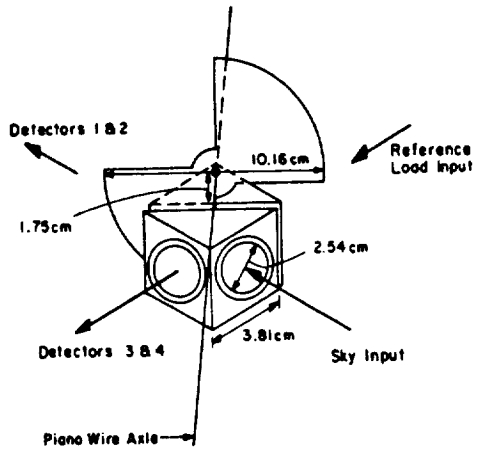

Fig. 1. Schematic view of the optical layout and chopper; the stator and rotor windings are not shown. The blade oscillates around the piano wire axle. When it is in (rotated 35° counterclockwise) radiation from the sky is reflected to detectors 3 and 4 and radiation from the reference load is reflected to detectors 1 and 2. When it is out (rotated 35° counterclockwise) radiation from the sky is transmitted to detectors 1 and 2 and radiation from the reference load is transmitted to detectors 3 and 4. The radiation is guided by 2.54-cm-diameter aperture Winston cones and light pipe. All the components shown are at 4.2 K; the detectors are at 0.24 K.

apertures ($< 1\ \text{cm}^2$), tuning fork choppers are commercially available.[5] They have been successfully used in a number of radiometers. they currently provide the modulation for the Diffuse Infrared Microwave Experiment, one of the three experiments aboard NASA's Cosmic Background Explorer satellite.

Our chopper oscillation frequency is determined by the torsional spring constant of the piano wire axle and the rotor moment of inertia I_R according to

$$\nu_{res} = \frac{1}{2\pi}\left(\frac{\pi G d^4}{8 l I_R}\right)^{1/2},$$

where G is the torsional modulus of the piano wire, l is the length of the wire, and d is its diameter. The ν_{res} increases by 10% when the chopper is cooled from 300 to 4.2 K.

An alternating current through the rotor at a frequency just below ν_{res} produces a torque of magnitude $|\mu_R \times B_S|$, where B_S is the stator magnetic field. The magnetic moment of the rotor μ_R is $N_R A_R i(t)$, where N_R is the number of turns, A_R is the area of the rotor loop, and $i(t)$ is the drive current. For amplitudes of $< 10°$ the motion is well approximated by the linear model:

$$\theta(t) = \frac{\mu_R \times B_S / I_R}{4\pi^2[(\nu_{res}^2 - \nu^2)^2 + \nu^2 \nu_{res}^2/Q^2]^{1/2}} \operatorname{Re}[\exp(-i\delta)\exp(i2\pi\nu t)]$$
$$\equiv \Theta_{max} \operatorname{Re}[\exp(-i\delta)\exp(i2\pi\nu t)],$$

where δ is the phase difference between the drive current and the motion and Θ_{max} is the amplitude of the motion. For small amplitudes Q is ~500. At larger amplitudes geometric considerations and damping terms enter, and this approximation becomes less precise.

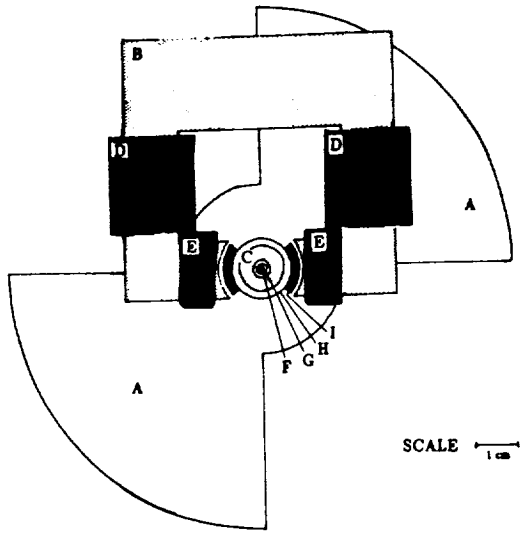

Fig. 2. Stator assembly as viewed looking down the axle: A is the chopper blade. B is the stator yoke, which is made of laminated Cryoperm[6] and thermally sunk to a LHe cold stage. C is the stator plug; it is also made of laminated Cryoperm. D and E are the potted superconducting wires.[6] Each of the D sections has 1350 windings, each of the E sections has 150. The piano wire axle F runs through a hole in the center of G, the copper stator plug heat sink. A side view of the stator plug is shown in Fig. 3. H is the stainless-steel rotor winding substrate. I is an end view of the rotor windings. A magnetic field flux line following the path of minimum reluctance passes from the stator body, through the rotor windings, through the stator plug, again through the rotor windings, and back into the stator body.

Stator

Design

The stator produces the stationary magnetic field by using a high permeability yoke and plug. The current through the superconducting windings around the yoke produces a constant magnetic field B_S, which is directed by a high permeability metal to the vicinity of the rotor. By using superconducting wire,[6] resistive heating is minimized. The reluctance of the magnetic path is dominated by the gap between the yoke and the plug in which the rotor moves. The geometry of the surfaces at the gap determines the spatial structure of the field. In particular the curve surface of the yoke and the cylindrical plug ensure that most of the field lines pass through the rotor windings perpendicular to the current and rotor motion.

Construction

Both the yoke and the plug are made of laminated Cryoperm 10,[7] a soft magnetic material whose permeability is maximum near 4.2 K. The shapes are cut by wire electrical discharge machining. They are laminated in a Teflon mold using Stycast 2850 FT epoxy[8] with catalyst 11. Each of the 90 pieces is 0.1 mm thick. They are glued together to produce a piece that is 1.27 cm thick. To ensure that the yoke is isothermal and to provide a good heat sink for the windings, the outermost laminae are 1-mm thick copper. The

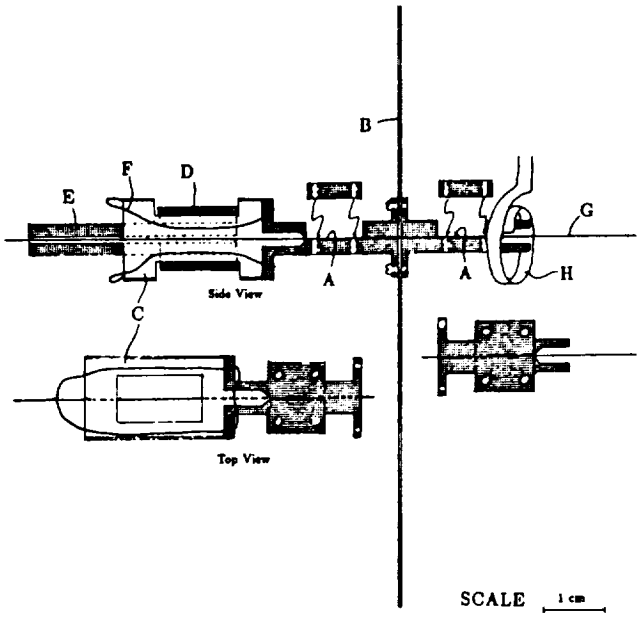

Fig. 3. Rotor assembly with top and side views. A regions are the copper axle clamping areas. Brass 2-56 screws and epoxy affix the tops of the clamps to the clamping area. B is a side view of the chopper blade. C is the stainless-steel rotor winding substrate; this is soldered to the copper clamp. D and E comprise a side view of the stator plug and copper stator plug heat sink. F is an example of a single-rotor winding. The windings are thermally sunk by passing over the end of the copper clamp. The winding path farthest from the blade must allow for the insertion of the stator plug. G is the piano wire axle. H is a perspective view of the copper rotor heat sink. One end is soldered to the copper clamp; the other is thermally sunk to a LHe cold stage.

yoke is thermally sunk by clamping the copper to a 4.2-K stage with an indium gasket.

Before the windings are added the yoke is coated with a thin layer of Stycast 2850 to ensure that the wire will have an electrically insulated base. After that has cured the wire is wound on by hand with a periodic application of Stycast 2850. A total of 3000 windings was used as indicated in Fig. 2.

The plug is a cylinder of laminates 1.27 cm long and 1.02 cm in diameter with a 0.33-cm hole. A copper rod epoxied into the hole provides the heat sink for the laminates and a way to hold the plug in place. The piano wire runs through a 0.13-cm diam hole in the copper rod. Data on the materials are presented in Table I.

Rotor

Design

The rotor is the oscillating part of the chopper and consists of four pieces: the chopper blade, rotor coil, axle clamps, and heat sink. The blade and rotor coil are attached to the piano wire with the axle clamps; the heat sink thermally links the rotor assembly to the LHe cold stage.

The blade is made of gold-coated aluminum. A good approximation to the optical absorptivity is $\alpha(\nu) = 40\pi\,\delta\,\nu \approx 5 \times 10^{-4}$, where δ is the skin depth and ν is the frequency of the incident radiation in wave numbers. The factor of 10 above the classical expression $4\pi\,\delta\,\nu$ comes from the anomalous skin effect and the 45° incident angle. In our spectral passband at 9.5 cm^{-1} (1.05 mm), a change in temperature of the chopper blade of 15 mK at 4.2 K would mimic a change in the cosmic microwave background of $\Delta T_{CMB}/T_{CMB} = 10^{-5}$. A resistive heater and a diode thermometer mounted on the rotor allow us to quantify this effect in the laboratory. Over 8 h the temperature changes by <40 mK, the digitization limit for our thermometers. The thermal time constant is ~5 s or 20 chopper cycles.

Clearly it is important to keep the blade cold and thermally stable. This is accomplished with robust heat sinking and by minimizing the power dissipation. A flat strip of temper-6 oxygen-free high-conductivity copper, 5 cm long, 0.5 cm wide, and

Table I. Chopper Construction and Operation

Construction		
$G_{300\,K} = 8.3 \times 10^{11}$ dyn/cm²		$I_R = 110$ g cm²
$\nu_{res} = 4.47$ Hz with $d = 0.046$ cm		$l = 20$ cm
$\nu_{res} = 8.8$ Hz with $d = 0.064$ cm		$l = 20$ cm
$A_R = 2.5$ cm²		
Blade	Diameter = 10.16 cm	Thickness = 0.064 cm
		Gold coating ≈ 2000 Å
Windings	Supercon T48B fine wire	
	Core diameter = 0.051 mm, core + copper = 0.0813 mm	
	Net diameter (wire + insulation) = 0.107 mm	
	$T_{crit} = 10$ K	$B_{crit} = 100$ kG
	$N_R = 180$	$R_{300\,K} = 45\ \Omega$
	$N_{tot} = 3000$	$R_{300\,K} = 955\ \Omega$
Cryoperm 10	$B_{sat} = 9000$ G	$\mu_{4.2\,K} = 60{,}000$
		Thickness/laminant = 0.1 mm
Operation		
$\nu_{res\ at\ 4.2\,K} = 4.474$ Hz		$\nu_{chop} = 4.466$ Hz
$i_s = 250$ mA		$B_s = 1000$ G
$i(t) = 9.3\cos(2\pi\nu_{chop}\,t)$ mA		Amplitude = 35 deg

0.005 cm thick, is loosely wound around the axle 1.5 times in a watch spring configuration. One end is attached to the clamps that hold the rotor and blade; the other is sunk to 4.2 K. The thermal conductance of the heat sink is 1.7 mW/K. The rotor power dissipation is minimized by using superconducting windings and by keeping good electrical conductors as far away from the magnetic fields as possible. When the chopper is operated with a 35° amplitude, it dissipates ~1 mW. Because of the superconducting wires, the chopper may be operated only below 8 K.

The two primary loss mechanisms on the rotor assembly are superconducting hysteresis and eddy currents. Hysteresis arises because the rotor wires must periodically expel the stator field. This forces part of the superconductor to go normal. Wilson[9] provides a thorough treatment of the process; he describes this loss as the viscous motion of quantized flux lines. We estimate the effect by computing the magnetic energy inside the superconductor and multiplying it by twice the chopping frequency:

$$P_h = \Gamma \frac{B_S^2}{8\pi} \times V_s 2\nu_{chop} = 2.6\Gamma \text{mW},$$

where V_s is the volume of the superconductor and Γ is a factor of the order of 0.5. Wilson computes it for a variety of geometries. Eddy currents are the second loss mechanism. When a good conductor moves through a magnetic field, the dissipated power is

$$P_e \approx V_c \sigma_c (v/c)^2 B_S^2 = 0.2\text{mW},$$

where V_c is the volume of the conductor, σ_c is the conductivity of the conductor, v is its velocity, and c is the speed of light. We have assumed that motion is at right angles to the field. In our geometry P_e is dominated by the copper cladding on the superconducting wire. The stainless substrate on which the rotor coil is wound does not contribute, and we may neglect fringing fields.

The rotor assembly must be statically balanced. That is, the center of mass should lie on the axle. An imbalance will cause a change in the resonant frequency with a change in chopper orientation. This effect may be modeled as

$$\nu_{res}^2 = \nu_0^2 + (\delta\nu)^2 \cos(\theta_c + \phi),$$

where ν_0 is the nominal resonant frequency, θ_c is the angle of orientation of the entire chopper assembly, ϕ is a phase that depends on the geometry, and $(\delta\nu)^2$ is the amplitude of the effect where $\delta\nu$ depends on the magnitude of the mass imbalance. For a mass imbalance of 1.6 g cm, we found $\delta\nu = 0.034$ Hz. By adding trim weights, this is reduced to 0.006 Hz.

As a result of small asymmetries in the rotor construction, the largest principal moment of inertia of the rotor assembly is not perfectly aligned with the chopper axle; that is, the rotor is not dynamically balanced. This produces forces at the axle support points at the chopping frequency. Therefore the resonant frequencies of the support structure must be well above that of the chopper. The tension of the wire axle is set so that the transverse frequency is 50 Hz at 300 K, well above any large cryostat resonances. The detectors and signal train are mounted on a completely separate structure, further isolating them from the chopper. The total optical noise is consistent with zero microphonic coupling from the chopper.

Construction

The rotor coil is the most difficult piece of the chopper to make. To serve as a substrate for the windings, a 1.27-cm-diameter by 2.54-cm-long thin wall stainless tube is soldered to one of the copper clamps. The wires follow the path shown in Fig. 3. The coil has two redundant windings wired in parallel of 150 turns each. Note that the strator plus has to slip inside the stainless-steel tube and that the coils must slip into the hole in the stator yoke. Also note that the windings in the vicinity of the stator must run parallel to the axle. All windings are potted in Stycast 2850 FT. Again a Teflon mold to train the wires is indispensable.

The bond between the rotor assembly and axle is accomplished with the axle clamps and a dab of Stycast 2850 FT. Size 2-56 brass screws hold the top of the clamp to the base; stainless steel should not be used because its thermal contraction coefficient is less than that of copper.

Performance

The chopper has run flawlessly for more than 500 h at 4.5 Hz and has survived three balloon flights. There are no discernible differences in operation from one cooling cycle to the next. A good measure of changes in the chopper amplitude is the emf, V_E generated by the coil motion in the stator field. By using four wires from the rotor, V_E may be measured without the effects of the drive current in the lead resistance. During operation both V_E and the rotor temperature are continuously monitored.

The chopper response is characterized by measuring V_E versus the rotor drive current for a range of frequencies near resonance. At a constant amplitude drive current, $d\Theta_{max}/d\nu$ is smallest for $\nu < \nu_{res}$. To minimize the sensitivity to drive frequency drifts, we set $\nu_{chop} = \nu_{res} - 0.008$ Hz. The optimal magnitude of the stator and rotor currents is empirically found to be $i_S = 250$ mA and $i_R = 9.3 \cos(2\pi\nu_{chop}t)$ mA, respectively.

The amplitude of the motion was directly measured in the laboratory by using an electrical contact to the edge of the blade at the desired amplitude Θ_{max}. The amplitudes reported here are inferred from the emf characterized during this measurement; the absolute accuracy in Θ_{max} is ±6%. Both i_S and i_R are unchanged from cycle to cycle. The next generation chopper uses the blade as part of a variable capacitor in an ac bridge circuit as a direct amplitude monitor.

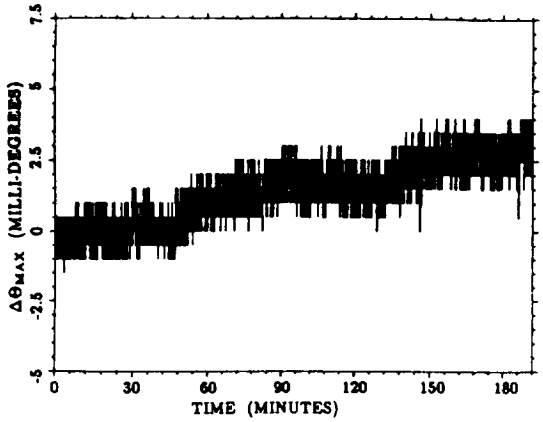

Fig. 4. Measurement of the chopper stability. The ordinate scale is obtained by assuming that the amplitude is proportional to the emf V_E, which is the measured quantity. V_E is sampled at 4.466 Hz with an integrating lock-in amplifier. The data were taken with a cryostat containing the chopper sitting on the laboratory floor. No special attempts at vibration isolation were made. As noted in the text the drift is an upper limit to chopper variations.

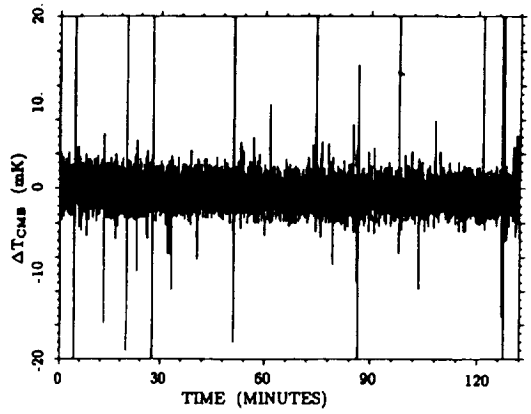

Fig. 6. Detector output during the last 2 h of the measurement in Fig. 4. The ordinate is given in terms of the change in the temperature of a Planck emitter at 2.75 K. What is actually measured is the change in power from a 5 K Planck emitter. The absolute value is accurate to 15%. Just as with V_E the detector output is sampled at 4.466 Hz with an integrating lock-in amplifier. The spikes are due to cosmic ray hits and local interference. During a balloon flight there is less noise.

Modulated external magnetic fields such as those of the earth in the frame of a rotating platform can add to B_S and alter the chopper motion. The size of the effect in V_E is proportion to $2\Delta B_{ext}/B_{sta}$, since $V_E \propto B_S^2$. Therefore with magnetic shielding (for example, superconducting lead) and a large stator field the interference may be minimized. The effect is easily tested by modulating a field in the region of the chopper with Helmholtz coils and monitoring V_E. We find that with our amount of shielding, which is minimal but adequate, $d\Theta_{max}/dB_{ext} = 0.01°/G$. The resonant nature of the chopper smooths over changes in the field with a time constant of 3.3 s.

Since variations in the blade amplitude produce a change in signal, the chopper is driven so that the edge of the blade at Θ_{max} is well outside the optical path. This is accomplished by making the blade move in a slit, approximately four blade widths wide, but into the lightguide (Fig. 1). At the end of its travel the blade's edge is in an open radiation cavity and outside the geometric beam. If the amplitude does not correspond to 100% modulation ($\Theta_{max} < 28°$), there is a correlation betweeen the signal and amplitude variations. However, when $\Theta_{max} > 30°$, the correlation disappears.

The stability is tested by driving the chopper and measuring V_E with a lock-in amplifier. The time series of the lock-in output and the power spectrum are shown in Fig. 4 and 5, respectively. The slow drift in V_E may be due to a change in chopper amplitude; thus these data may be used to set an upper limit on changes. For 2 h during the same period the output of one of the bolometers with the ordinate calibrated in T_{CMB} is shown in Fig. 6. The drift here is most likely caused by thermal drifts in the radiation loads. The spikes are due to cosmic ray hits on the bolometer and local rf interference. The data were taken with the experiment sitting on the laboratory floor. The high-altitude balloon environment is much more benign.

In the course of the astrophysical data analysis,[1] we saw no effects that could be associated with the chopper. For the flight made in October 1989 the effects of the Earth's field can be seen in V_E. However, using laboratory measurements we can rule out the possibility that this will contaminate the data to the level of $\Delta T_{CMB}/T_{CMB} < 8 \times 10^{-5}$ for measurements of the CMB dipole. For smaller angular scales the limits are much better. All indications are that this type of chopper can be used for the next more sensitive generation of experiment.

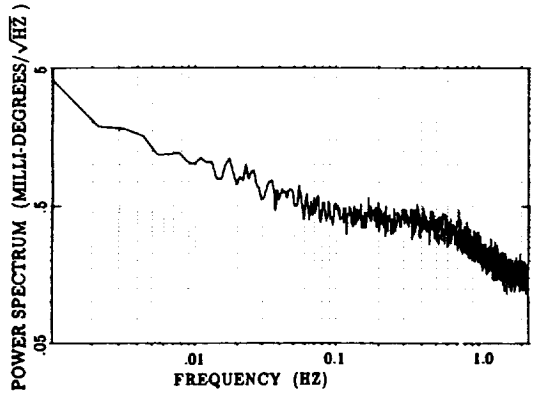

Fig. 5. Power spectrum of the data in Fig. 4. During a balloon flight secondary modulation is provided by rotating the experiment at 0.004 Hz.

Lyman Page was generously supported by a NASA Graduate Student Research Program fellowship. This work was partially supported by NASA grant NAGW-1841.

References

1. L. A. Page, E. S. Cheng, and S. S. Meyer, "A large-scale cosmic microwave background anisotropy measurement at millimeter and submillimeter wavelengths," Astrophys. Lett. 355, L1–L4 (1990).

2. P. M. Downey, A. D. Jeffries, S. S. Meyer, and R. Weiss, "Monolithic silicone bolometers," Appl. Opt. **23**, 910–000 (1984).
3. J. B. Peterson, "The spectrum of the cosmic background radiation from 2.3 cm^{-1} to 11 cm^{-1}," Ph.D. Thesis, Department of Physics, University of California at Berkeley (Apr. 1985).
4. H. Murakami and A. E. Lange, "A low frequency beam switch," in A. E. Lange," An Attempt to Measure the Diffuse Brightness of the Sky at Submillimeter Wavelengths," Ph.D. dissertation Department of Physics, University of California, Berkeley, Berkeley (January 1987).
5. Frequency Control Products, Inc., Calif., 61-20 Woodside Ave., Woodside, N.Y. 11377; (212) 458-5811. This company also makes a taut band chopper for large apertures.
6. Supercon, Inc., 830 Boston Turnpike, Shrewsbury, Mass. 01545; (617) 842-0174.
7. Emerson & Cuming, Inc., Canton, Mass. 02021.
8. Vacuumschmelze, 186 Wood Ave. South, Iselin, N.J. 08830; (201) 321-4791.
9. M. N. Wilson, *Superconducting Magnets* (Clarendon, Oxford, 1983).

a reprint from Applied Optics

Millimeter–submillimeter wavelength filter system

Lyman A. Page, Edward S. Cheng, Boris Golubovic, Joshua Gundersen, and Stephan S. Meyer

We describe the design, fabrication, measurement, and performance of a set of cryogenic millimeter–submillimeter wavelength filters used in a balloonborne bolometric radiometer. The set contains single resonant mesh grids used as dichroic beam splitters, resonant meshes in a double quarter-wave configuration, a commercial inductive grid filter, and high-frequency blocking filters. The resultant system has passbands at λ = 1.73, 1.05, 0.61, 0.44 mm with $\delta\lambda/\lambda$ = 0.23, 0.23, 0.12, 0.06. Limits on high-frequency leakage are deduced from laboratory measurements and from the analysis of flight data. The filter set response to three different sources of radiation is presented to show the method and limitations of our characterization. The key element of the filter system is a resonant periodic array of cross-shaped holes etched in thin aluminum. We give an empirical scaling law for the resonant wavelength as a function of structure parameters for aluminum on 25-μm-thick Mylar. Plots of the transmittance for normally incident radiation and the transmittance and reflectance for a 45° incident radiation are presented.

1. Introduction

Cryogenic bolometers are the detectors of choice for the measurement of low-background broadband radiation from 2 to 100 cm^{-1} (100–5000 μm). For most astrophysical applications,[1–4] bolometers require the use of band-defining filters to restrict the radiation reaching the detectors. Instrumental, terrestrial, and astrophysical foreground sources with high surface brightness can easily overwhelm a signal if the filter system lacks sufficient out-of-band rejection. To show the magnitude of the problem, consider a broadband IR source whose power per unit bandwidth increases as ν^3. A 1-cm^{-1}-wide filter at 5 cm^{-1} with a transmittance of 1.0 collects as much power as a 10-cm^{-1}-wide filter at 10 cm^{-1} with a transmittance of 0.01. The leakage outside the desired band must be carefully characterized to prevent the misinterpretation of results because of unanticipated radiation from known sources.

Ulrich[5–7] describes three types of filter: (1) A capacitive grid consisting of a periodic array of metallic squares on a dielectric substrate. This grid acts as a low-pass filter. (2) An inductive mesh that is a two-dimensional wire screen, the complement to the capacitive grid. This mesh acts as a high-pass filter. (3) A resonant grid that is a periodic array of cross-shaped holes that act as a bandpass filter. Following Nolte *et al.*, we term such an array an inductive cross mesh (ICM). The geometry is shown in Fig. 1.

Beneficial effects for all three types of filter are obtained when they are resonantly coupled. Excellent low-pass filters are made with stacks of capacitive grids.[6,7] Many researchers have used these stacks of grids to enhance the cutoff of an inadequate passband filter. Or, with the addition of a high-pass filter and proper selection of the spacing and grid parameters, capacitive grids can be part of a bandpass filter.[7,9] Inductive meshes are used to make double-half-wave narrow-bandpass filters[10,11] when three are spaced at $\lambda/2$. A convenient feature is the predictability of the response; however, there are higher harmonics that must be blocked with additional filters. Three ICM grids spaced $\lambda/4$ of their center wavelength[12] make a high-transmittance, low-leakage filter called a double quarter wave (DQW).

We have built and flown a balloonborne experiment designed to measure the anisotropy of the cosmic microwave background radiation (CMB) in the pres-

L. A. Page is with the Department of Physics, Jadwin Hall, P.O. Box 708, Princeton University, Princeton, New Jersey 08544. E. S. Cheng is with the Goddard Space Flight Center, Code 685, National Aeronautics and Space Administration, Greenbelt, Maryland 20771. B. Golubovic and S. S. Meyer are with the Department of Physics, Room 201F-001, Massachusetts Institute of Technology, Cambridge, Massachusetts 02139. J. Gundersen is with the Department of Physics, University of Santa Barbara, Santa Barbara, California 93106.

Received 31 July 1992; revised manuscript received 10 May 1993.
0003-6935/94/010011-13$06.00/0.

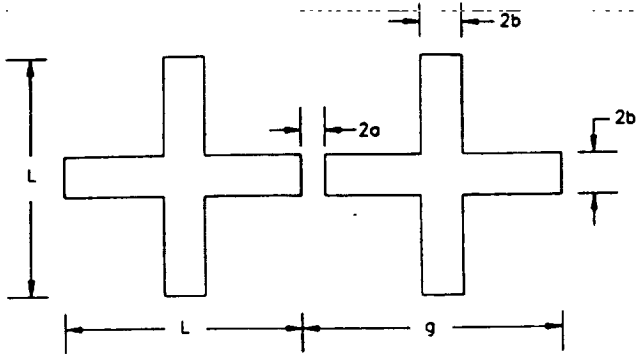

Fig. 1. Geometry for the ICM. The outlined region is the shape of the hole, L is the cross-arm length, g is the period of the array, $2b$ is the cross width, and $2a$ is the separation.

ence of spectrally steep foreground sources.[4,13] Four passbands, labeled channels 1–4, are centered at 5.8, 9.5, 16.5, and 22.5 cm^{-1} (λ = 1.7, 1.1, 0.61, 0.44 mm), respectively. They were chosen to avoid large atmospheric emission lines, provide broad spectral coverage, and give maximum sensitivity to the CMB. The throughput of the system is 0.5 cm^2 sr. The filters are placed in a 2.54-cm-diameter circular lightguide giving a beam half-angle on the filter of 11° (f/2.8). Our radiometer employs all the filters described above, and, although data are presented for each application, we focus on the design, construction, and evaluation of the ICM's. The optical layout is shown in Figs. 9 and 10. In the configuration of the experiment described here, incoming radiation is referenced to an internal load, and the high- and low-frequency sides are divided by an oscillating chopper blade.[14] [In an alternative mode of operation, a composite capacitive grid filter replaces the chopper blade to act as a dichroic beam splitter at 45° incidence (see Fig. 6).] After this first split, both arms are further split with single-layer ICM filters, since they provide excellent efficiency in both transmission and reflection (especially just above the resonance band) at 45° incidence. The band-defining filters for channels 1, 2, and 3 are DQW's. The band-defining filter for channel 4 is a multilayer inductive mesh filter purchased from Cochise Instruments.[15] The high-frequency blocking is done with absorption filters.

The filters are robust; they have been cooled from room temperature to 0.24 K more than 40 times and have survived three balloon flights where they experienced 8-g accelerations. The system passbands have been measured half a dozen times and at least once after each flight. No change in the passband shape has been detected to within 5%.

In the following, first we discuss various filter models and summarize empirical scaling relations for ICM's. In Section 3 we describe the fabrication, and in Section 4 we describe the measurement procedure. A detailed look at the filter responses is presented in Section 5 where plots are shown of the transmittance of an ICM, a DQW, and a capacitive grid with radiation incident both normally and at 45°. In Section 6 we describe the layout and assembly of the radiometer filter set. Finally, in Section 7 the performance of the filter system is analyzed. Tests for high-frequency leakage, the transmission budget, and the computed response to three different sources are discussed. Throughout this paper wavelength and

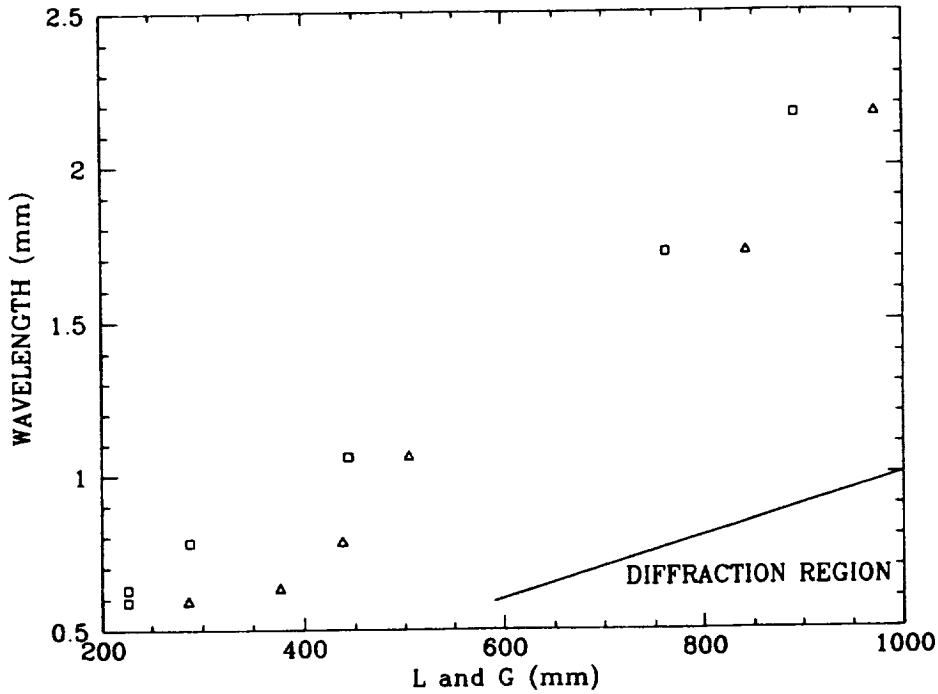

Fig. 2. Plot of the cross-arm length (squares) and the period of the array (triangles) versus λ_{res} for ICM's. The error bars are of the order of the size of the symbols. There is a slightly better correlation of λ_{res} with L than with g. When $\lambda_{res} > g$ diffraction processes dominate.

Table 1. Resonant Mesh Characteristics

Grid[a]	ν_{res}[b] (cm^{-1})	$\delta\nu/\nu_{res}$	T[c]	L[d] (μm)	g[d] (μm)	a[d] (μm)	b[d] (μm)
ICM 1	4.6	0.35	0.91	892	972	40	56
ICM 2	5.8	0.41	0.85	762	842	40	71
ICM 3	9.4	0.46	0.92	444	504	30	45
ICM 4	12.8	0.17	0.72	288	438	75	15
ICM 5	16.0	0.16	0.66	226	376	75	23
ICM 6	17.0	0.33	0.78	226	286	30	30

[a]ICM's are numbered in increasing frequency as in Fig. 4.
[b]ν_{res} is the frequency of maximum response ±0.15 cm^{-1}.
[c]T is the peak transmission ±0.03.
[d]L, g, a, b are the grid parameters as defined in Fig. 1. They are measured in micrometers. Estimated errors are ±5 μm for dimensions > 100 μm and ±3 μm for dimensions of < 100 μm.

frequency are used interchangeably; $\nu = 1/\lambda$ is given in inverse centimeters and λ is given in centimeters; ν and λ are a convenient Fourier transform pair.

2. Models of the ICM

Although simple models for the transmittance of both capacitive grid[5,6] and inductive mesh[11] filters in multimoded systems agree fairly well with experiment, the same cannot be said for ICM's. Here one must rely on empirical findings or involved computer programs. There are three ways to interpret an ICM: (1) model the mesh with lumped circuit elements,[16] (2) model it as an array of crossed dipoles,[17] or (3) compute the transmittance by solving the complete boundary value problem.[18,19] While λ_{res} ($=1/\nu_{res}$), $\delta\lambda/\lambda$ ($=\delta\nu/\nu$), the high-frequency rejection, and the transmittance are all important design parameters, only the prediction of λ_{res} is considered in this section; the other parameters are discussed in Section 5.

The first picture, which was pioneered by Ulrich, is the most intuitive. The flat wire of width $2a$ and length $2b$ between two crosses acts as an inductor, and the metal around the arms of a cross acts as a capacitor. Estimates for the actual L and C as a function of the geometry may be found in Marcuvitz.[20] The resonant wavelength is then proportional to $[L(g, a, b)C(g, a, b)]^{1/2}$ where g, a, and b are shown in Fig. 1. Cunningham's[21] results demonstrate the scaling of λ_{res} with the grid parameters. Anderson[16] computed λ_{res} for the case of Jerusalem crosses and found a frequency that is 7% lower than the experimental results of Arnaud and Pelow.[22] Using an appropriately modified version of Anderson's formula, we find our predictions to be approximately 35% too low. In the lumped element method, corrections are made for diffraction but not for fringing fields and the dielectric substrate. Ulrich's model is most useful for predicting the sense of a design alteration, for example, the presence of a dielectric increases the capacitance leading to a reduced resonant frequency. If the dielectric substrate were included in the computation, there would be less discrepancy between model and results.

Chase and Joseph[17] interpreted the ICM as an array of crossed flat strip dipole antennas. The resonant wavelength of a thin slot is $\lambda_{res} \approx 2L$. Figure 2 shows a stronger correlation between λ_{res} and L than between λ_{res} and g, which lends support to this picture; however, our resonant wavelength is considerably different for the same grid parameters. The best fit to our data is obtained with $\lambda_{res} = 2.1L +$ 180 μm. Cunningham gave the empirical formula $\lambda_{res} = 2.2g - 3.1(1.1a + b) = 2.2L + a - 3.1b$. The scaling with L is consistent, but there is a considerable difference in the dependence on b and a. We believe that this is due to the thickness of the Mylar substrate. Our substrate is 25 μm thick, which is a good fraction of the cross diameter, whereas Cunningham's was only 2.5 μm thick. Chase and Joseph used a variety of thicknesses, 1.5, 10, and 15 μm, which clouds the interpretation of their results. More dielectric in the field implies a greater capacitance and thus a higher λ_{res}. We therefore expect to find a higher λ_{res} than either of these two; this is borne out in Table 3 below.

All the grids discussed by Ulrich fall under the rubric of frequency-selective surfaces, where the shape of the periodically repeated element can be almost anything.[22] Numerically solving a frequency-selective-surface boundary value problem is computationally intensive; however, the predictions are in excellent agreement with the data.[19,23] In this sense the transmittance problem has been solved. Unfortunately, results for only a limited number of grid dimensions have been published. These computer programs take into account the dielectric substrate, the thickness of the metal, and an arbitrary incident angle. A commercially available program[24] solves

Table 2. DQW Characteristics

DQW	ICM Grid Type[a]	ν (cm^{-1})[b]	$\delta\nu/\nu$	T[c]
1	1	4.7	0.23	0.69
2	2	5.7	0.26	0.93
3	3	9.2	0.24	0.84
4	5	16.2	0.14	0.19

[a]DQW's are numbered in increasing frequency as shown in Fig. 7.
[b]ν is the central frequency of the passband.
[c]T is the peak transmission ±0.03.

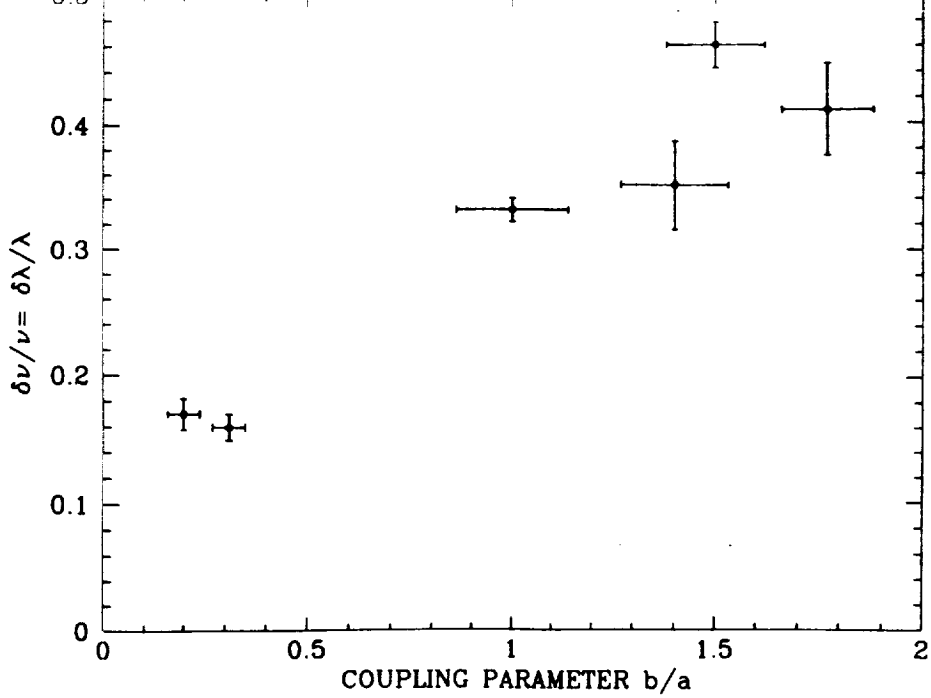

Fig. 3. Plot of the fractional bandwidth versus the coupling parameters b/a for single sheets of ICM. A linear least-squares fit yields $\delta\lambda/\lambda = 0.11 + 0.21b/a$. $\delta\lambda/\lambda$ is reduced when these are used in DQW's as shown in Table 2.

for an arbitrary periodic shape and multiple grids at a variety of spacings. By varying the spacing and aperture shape, one may optimize the filters for a given application.

3. Fabrication

In this section the fabrication of the individual resonant meshes and the DQW configurations are described. In essence, cross-shaped holes are etched in

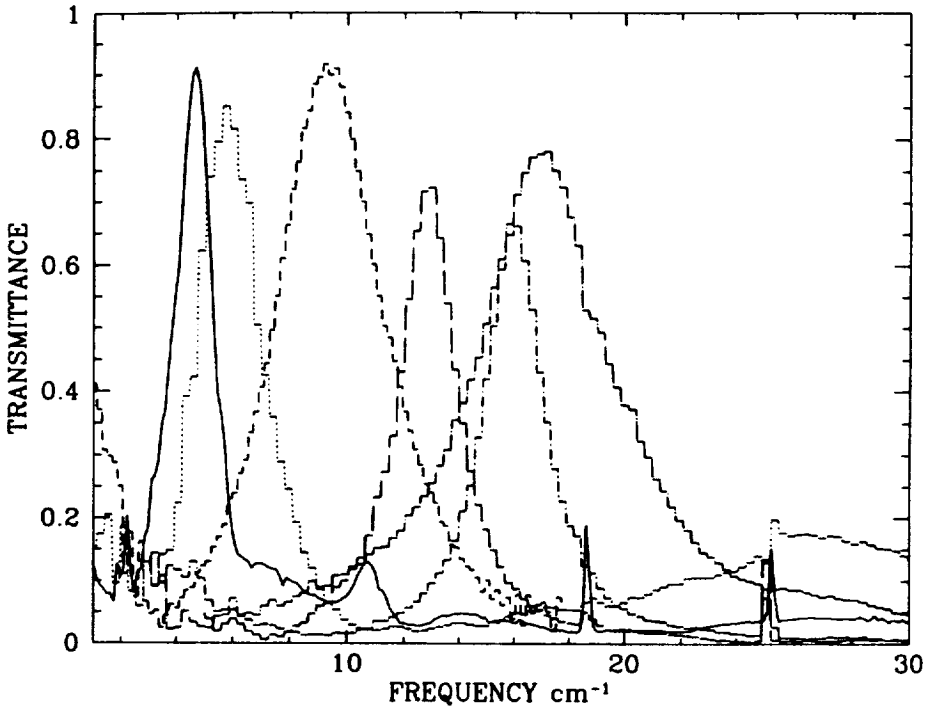

Fig. 4. Plots of the transmission of ICM's 1–6. The grids are labeled as in Table 3. Note the large transmission in the diffraction region for ICM 2. For a given frequency the transmission is worse for a smaller bandwidth. These data were taken with an $f/1.7$ system with the filters at ambient temperature: The grids are labeled with increasing frequency as in Table 1; the solid curve that peaks at 4.6 cm^{-1} is ICM 1; the dashed–dotted curve that peaks at 17 cm^{-1} is ICM 6.

Table 3. Comparison of Predictions of λ_{res}

ICM Grid[a]	λ_{res} This Work[b,c]	Cunningham[b,d,f]	Chase and Joseph[b,e,g]
1	2170	1830	1740
2	1720	1500	1490
3	1060	870	670
4	780	660	610
5	630	500	480
6	590	430	460

[a]ICM's are numbered as in Table 1.
[b]All dimensions are in micrometers.
[c]Mylar thickness, 25 μm.
[d]Mylar thickness, 2.5 μm.
[e]There is considerable error in the prediction caused by the scatter in the data. It is not clear for which grids which of the three mentioned Mylar thicknesses, 1.5, 10, 15 μm, is used. The values above are from Fig. 6 of Ref. 21.
[f]Ref. 21.
[g]Ref. 17.

aluminum evaporated onto 25-μm aluminized Mylar to make the resonant mesh, and then three of these are stacked with a $\lambda_{res}/4$ spacing to make a DQW.

The thickness of the aluminum on commercially available aluminized Mylar is typically 250 Å.[25] For a good passband definition, it should be of the order of skin depth thick ($\approx$1000 Å at 5 cm^{-1} at 300 K and $\approx$100 Å at 5 K). Thick metal, for example, with freestanding grids at high frequency, may lead to undesirable transmission characteristics as shown in Fig. 5 of Compton *et al.*[18] We evaporated aluminum onto Mylar until light from a 60-W incandescent bulb at a 2-m distance was completely blocked; the resultant thickness is estimated to be $\approx$800 Å. There are some tiny holes in the aluminization, but they have no effect on the filter properties.

The aluminized Mylar is processed at the Massachusetts Institute of Technology (MIT) microelectronics laboratory by standard photolithographic techniques. To guide the wafers through the commercial machines, the Mylar is plastered to 5.1-cm silicon wafers with vacuum grease. Shipley AZ 1350 positive photoresist is spun onto the Mylar-clad wafers at 5000 rpm and baked at 90 °C for 25 min. Next the wafers are exposed to UV radiation for 5 s through a 12.7 cm × 12.7 cm chrome plated-glass mask. The wafers are then developed for 60 s in a 1:1 solution of 312 developer and deionized water. The unwanted aluminum is etched off in a solution of 85 mL of 12M phosphoric acid, 20 mL of 12M nitric acid, and 15 mL of deionized water. The etch time ranges between 2 and 3 min, depending on the thickness of the aluminum. It is essential that the holes have well-defined features and that the quality is checked after each step. Rounded corners alter the design frequency, and fuzzy edges deteriorate the transmittance.

Individual meshes are put together to make a DQW with spacers made of punched brass. Since Mylar contracts $\approx$0.5% when it is cooled from 300 to 5 K, a material with a smaller thermal contraction coefficient is used so that on cooling the Mylar is stretched. The spacers are shaped like washers with a 2.9-cm i.d. and a 4.1-cm o.d. The thickness of one of the spacers is $\lambda_{res}/4$; the others is $\lambda_{res}/4 - nt$ to compensate for

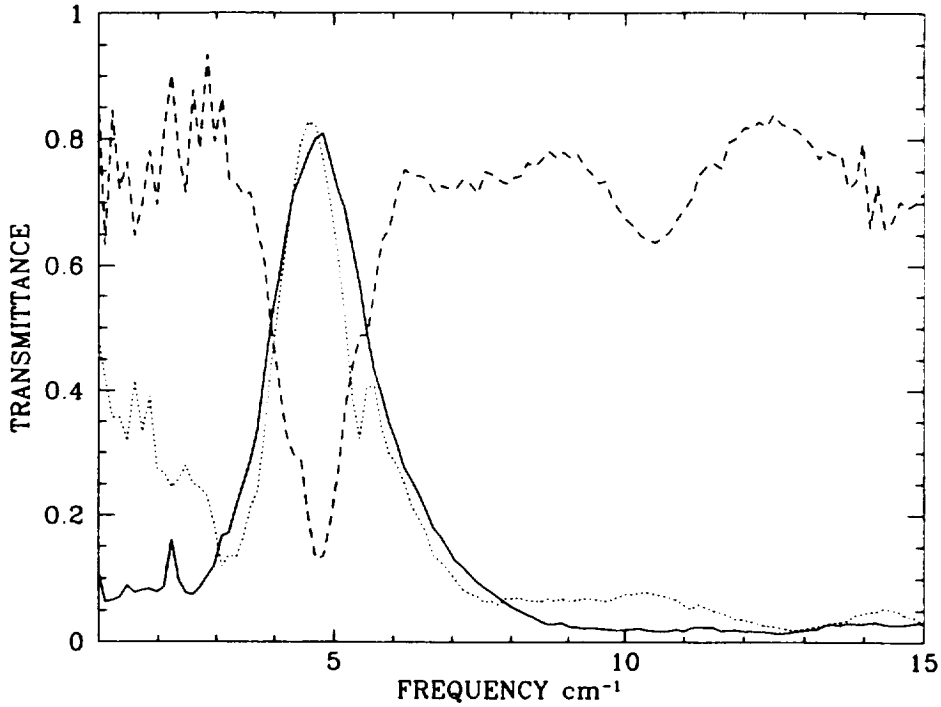

Fig. 5. Transmission of ICM 1 with radiation at normal incidence (solid curve) and with radiation incident at 45° (dotted curve). The small bump near 6 cm^{-1} is due to an incorrect orientation of the ICM. The dashed curve is the reflection spectrum with radiation incident at 45°. These spectra were taken with the filters at ambient temperature with $f/1.7$ optics.

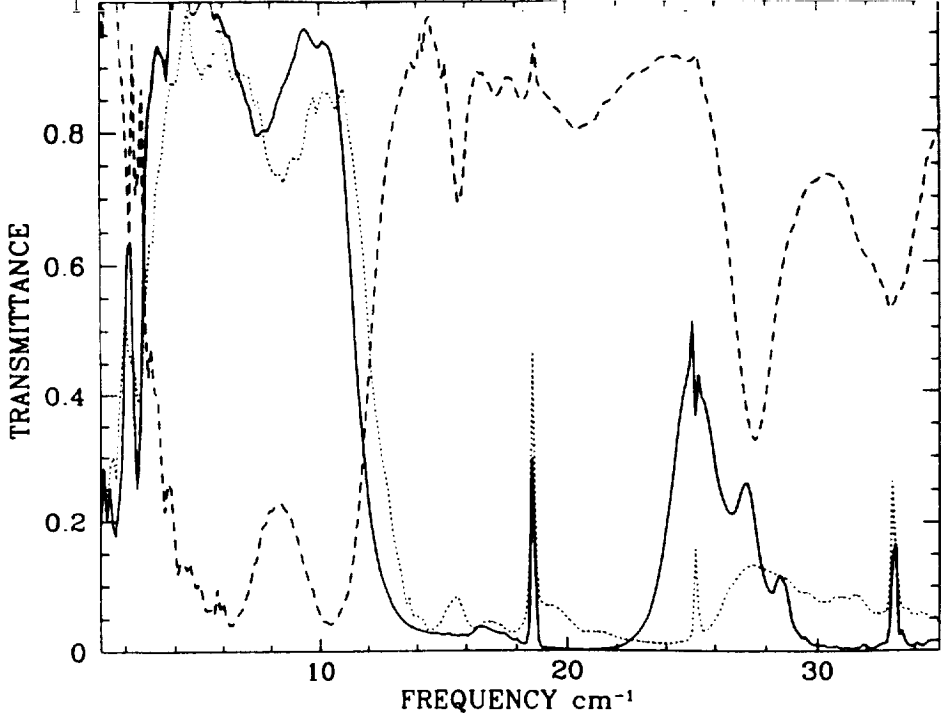

Fig. 6. Transmission of a capacitive grid filter with radiation at normal incidence (solid curve) and with radiation incident at 45° (dotted curve). The dashed curve is the reflection spectrum with radiation incident at 45°. Water vapor lines are clearly seen at 18.6, 25, and 33 cm^{-1}. This filter was made following Ulrich.[7] Four grids were combined in the pattern: $s1$–$g1$–$s2$–$g2$–$s3$–$g2$–$s2$–$g1$–$s1$, where $s1$, $s2$, and $s3$ are polyethylene spacers with thicknesses of 0.02, 0.0135, and 0.011 cm, respectively. The grids are arrays of copper squares; the lattice spacing for $g1$ is 0.0137 cm, and for $g2$ it is 0.0277 cm; the spacing between squares for $g1$ is 0.0023 cm, and for $g2$ it is 0.0043. The stack of grids was hermetically laminated, which resulted in a rugged monolithic filter. In one configuration of the radiometer, this filter replaces the chopper in Fig. 10 below. These spectra were taken at ambient temperature with $f/1.7$ optics.

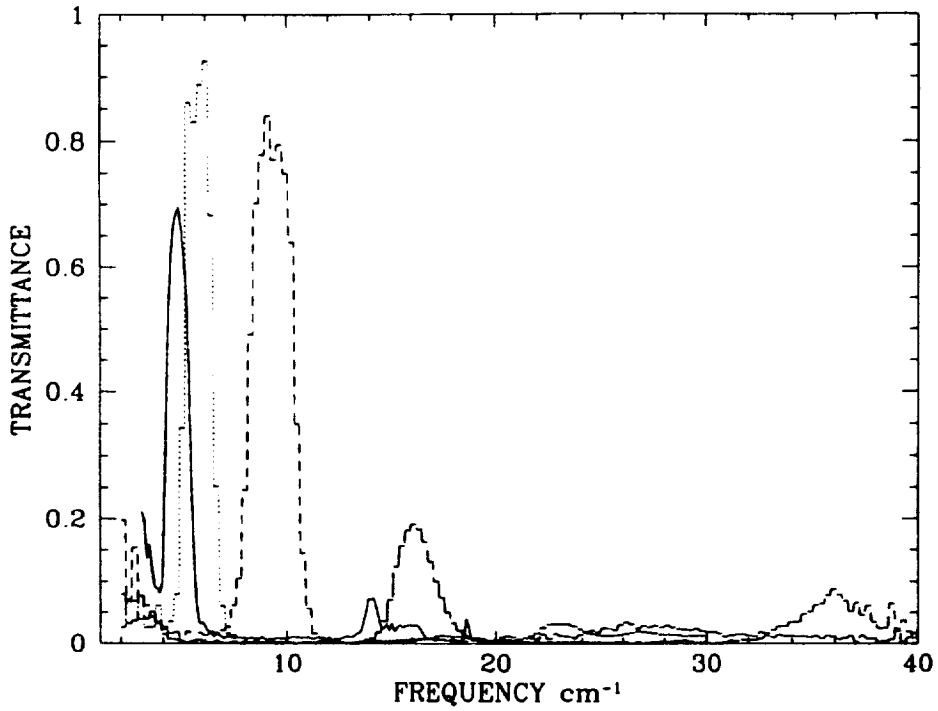

Fig. 7. Transmission of the four DQW's in Table 2. These spectra were taken at ambient temperature with $f/1.7$ optics. The solid curve that peaks near 4.7 cm^{-1} is DQW 1, the dotted curve is DQW 2, the short-dashed curve is DQW 3, and the long-dashed curve is DQW 4.

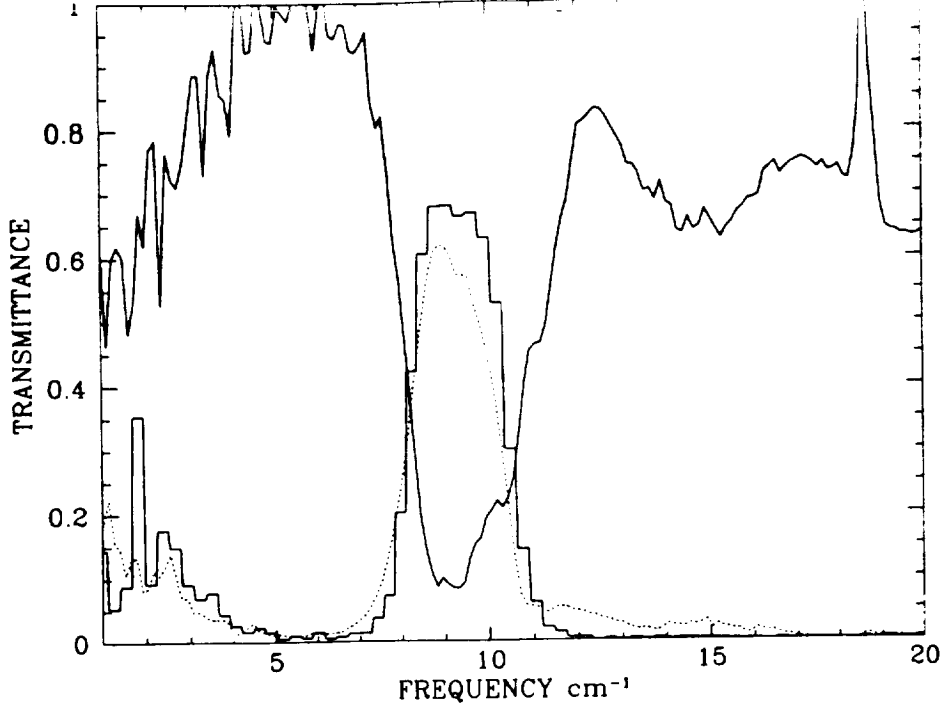

Fig. 8. Transmission of a DQW with radiation at normal incidence (solid curve) and with radiation incident at 45° (dotted curve). The curve with a minimum at 9 cm^{-1} is the reflection spectrum with radiation incident at 45°. These spectra were taken at ambient temperature with $f/1.7$ optics.

the thickness t and index ($n = 1.68$) of the Mylar. The punched shim is first sanded flat, then heated in a stainless-steel vise to flatten it further, and then etched in a 1:1 solution of distilled water and 12-M nitric acid until it is the correct thickness. The error on the thickness is ± 7 μm. Although we maintain a tight tolerance on the shim thickness, the $\lambda_{res}/4$ spacing is not critical; losses in the ICM alter the optimal spacing. In one test the spacing was increased to $\lambda_{res}/3$ with little degradation in performance.

The processed Mylar sheets are glued to the brass shims with a small amount of Stycast[26] 1266 epoxy. A customized vise and masking tape help to keep the film taut and flat while the epoxy sets. Two brass shims are then glued together in the same vise to produce the DQW. Holes poked through the filter with a hot needle permit air to escape when the radiometer is evacuated. The Mylar-covered spacers are arranged to keep as much of the Mylar as possible out of the region between the aluminized surfaces. The relative rotational orientation of the separate grids is arbitrary; the passband characteristics of aligned and unaligned meshes are the same.

4. Measurement

The filters are measured with a polarizing Fourier transform spectrometer (FTS) built at MIT,[27] similar to the one on-board NASA's Cosmic Background Explorer. One port is matched to an Infrared Industries[28] blackbody at 1200 K; the radiometer input is in another port. The other two ports are filled with a nonreflecting absorber at ambient temperature. The position of the carriage, which provides the variable delay, is controlled with a Michelson-type interferometer.

The FTS is used in two modes. For measuring the response of an individual filter, first we take a series of reference spectra with the filter out of the beam, then we take a series of data spectra with the filter in the beam, and finally we take a second series of reference spectra. The power spectra in each of the three series are averaged. We divide the two references to check for systematic problems, and then we divide the filter spectrum by the average of the reference spectra. The result is the absolute spectral response. Since the power spectra are used throughout, the noise does not reduce with averaging. For these measurements the detector is a 4.2-K bolometer[29] in a Dewar with $f/1.7$ optics matched to the FTS. The filters are at ambient temperature. All the results except for those in Fig. 11 are obtained with this method.

A more precise method than that discussed above is needed for measuring the total radiometer response. Here one averages the individual interferograms from each carriage scan to reduce the noise. In addition the detector response function, which is essentially a low-pass filter, is divided out. The time constant is found with the radiometer mounted on the FTS. A variety of couplings between the radiometer and the FTS were tried with negligibly different results. Since there is no reference spectrum, they are normal-

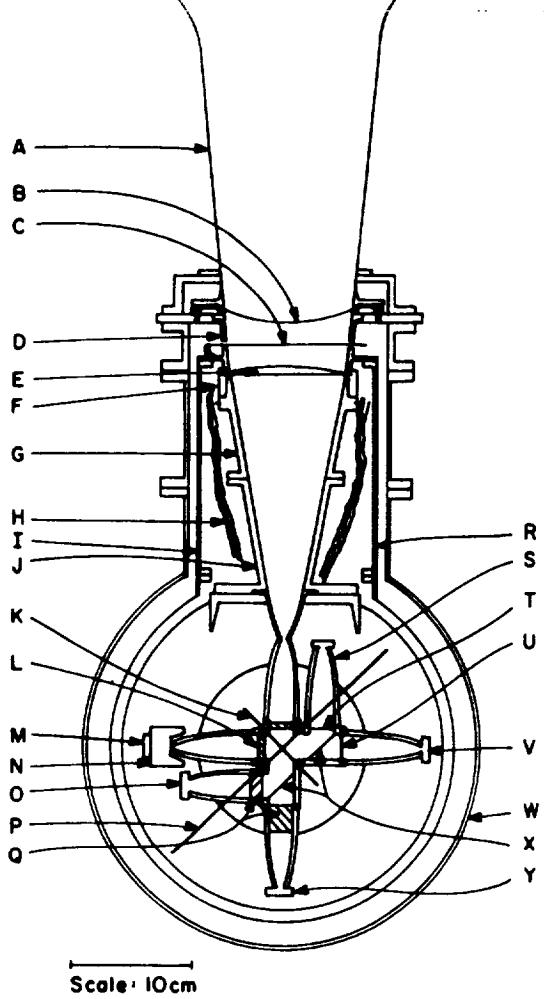

Fig. 9. Optical and cryogenic schematic of the radiometer. The chopper blade K oscillates about the axle P to direct radiation alternately from the input horn J and then the reference load M, N onto the detectors Y, O, V, and S, called channels 1–4, respectively. A, shielding horn to guard against stray radiation; it is outside the main beam. B, 375-μm polypropylene vacuum window. C, chopper shutter at 100 K; this is removed during observation. D, break between 300 and 77 K is covered with aluminized Mylar fingers. E, plano–convex polyethylene lens. F, flexible copper heat sinks for the lens. G, J, beam forming horn at 7 and 5 K. H, superinsulation. I, R, thermal shield at 85 K. L, Fluorogold filter on reference to match the load to the sky. The input blocking filters are shown at the wide end of the Winston cone attached to the input horn. Q, additional Fluorogold blocking for channels 1 and 2. The DQW's sit directly on top of the Fluorogold. T, Cochise inductive mesh filter. U, DQW 4. W, vacuum jacket. X, ICM dichroic beam splitters. The innermost of the concentric circles is the outline of the 0.24 K stage on which all the optics associated with the individual channels are mounted. The Winston cones for the input and reference arms and the chopper are at 4.2 K.

ized to 1.0. For these measurements the passband filters are at a temperature of 0.24 K.

Because the humidity of Cambridge can cause substantial absorption, the FTS is in a dry-nitrogen purged Plexiglas enclosure; despite this, water line features are seen at 18.6 and 25 cm^{-1}.

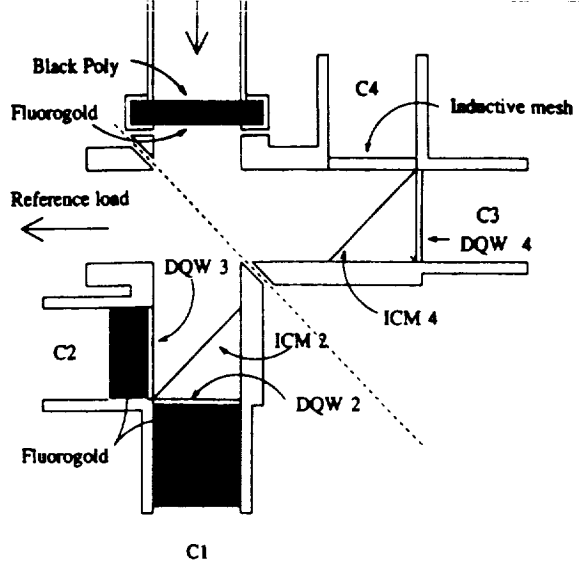

Fig. 10. More detailed view of the filter layout. The black polyethylene and Fluorogold nearest the incident radiation are at 4.2 K; all other optics in this figure are at 0.24 K. The detectors for each channel are in the focal region of Winston cones; only the first 3 cm of the Winston cones are shown. The dotted line indicates where the chopper blade moves. When the chopper blade fills the light pipe, the incident radiation is reflected onto channels C3 and C4, while radiation from the reference load is reflected into channels C1 and C2. The numbers on the DQW's and the ICM's are those used in the text.

5. Performance of Individual Filters

A summary of the performance and grid sizes for the ICM is given in Table 1; Table 2 gives the characteristics of the DQW made from the elements in Table 1. Not all ICM's were turned into DQW's. In selecting the grid dimensions, we followed the general observations of previous researchers: (1) The wavelength of the peak transmittance scales with L as shown in Fig. 2. (2) The half-power bandwidth increases with b/a as shown in Fig. 3. We find that $\delta\lambda/\lambda = 0.11 + 0.21b/a$. (3) The smaller b/L is, the better the high-frequency rejection. Plots of λ_{res}/L versus b/L and a/L were not illuminating.

Figure 4 shows the transmittance of a grid for each set of dimensions given in Table 1 for normal incidence ($f/1.7$). The Wood anomaly,[18] which should be at $\lambda_{res} = g$, is not seen, presumably because of the finite resolution of the measurement and the large range of incident angles. Table 3 gives a comparison of our results with those of Cunningham[21] and Chase and Joseph.[17] A simple model can explain the difference between our results. Assume that a greater fraction of the field in the cross arms is in the Mylar; consequently the capacitance is greater and λ_{res} is higher. That is, $\lambda_{res} \propto \sqrt{C} \propto [(1 + n^2)/2]^{1/2}$ (see Ref. 9) where $n = 1.68$ is the index of Mylar.

Chase and Joseph point out that as the coupling between crosses increases (a decreases or b increases), the mutual reactance decreases. At resonance the net reactance, $X_{mut} + X_{self}$, is equal to zero. Thus the

self-reactance must increase; this occurs at slightly shorter wavelengths than $2L$. The result is a decrease in λ/L with increasing b/a, an effect that is evident in our data.

Figure 5 shows how an ICM can be used as a diplexer; both the transmittance and reflectance are shown for radiation incident at 45°. The best transmittance occurs when the crosses are oriented so that the projections of the arm lengths onto the plane of incidence are equal. The small bump on one side shows that this criterion was not quite met. Note that the resonant frequency does not change appreciably with incident angles up to 45°. In one configuration of the experiment, a capacitive grid filter is used as a diplexer; its transmittance is shown in Fig. 6.

The DQW's are shown in Fig. 7. In general, the filters are narrow and have quite high transmittance. A striking feature is the relatively poor transmittance of the 16-cm^{-1} filter despite the quality of the individual meshes. This poor transmittance is most likely due to the strong absorption of the Mylar being multiplied by the Q of the resonant cavity as can be seen with a crude model. When a power absorption coefficient for Mylar of $\alpha(\nu) = 0.16\nu + 0.0051\nu^2$ is used,[30] $\alpha(16) \approx 4$ cm^{-1}. With three 25-μm sheets and a Q of 20, the filter absorbs ≈ 0.6 of the incident radiation. All the DQW's show a broad pronounced hump in the diffraction-dominated region ($\nu > 1/g$) as predicted by Compton *et al.*[18] The hump is also evident in the individual grids shown in Fig. 4 and has been observed in commercially available ICM grid filters as well. For out-of-band rejection, this hump is a more serious problem than the steepness of the skirt; the hump must be blocked with additional filters. DQW's may be used as diplexers, but the results are not spectacular. An example is shown in Fig. 8.

Although the transmittance of the individual ICM's was never measured at cryogenic temperatures, the peak of the set of cold filters was within 0.2 cm^{-1} of the value computed by multiplying the measured responses of the individual room-temperature filters for channels 1, 2, and 3. For channel 4, ν_{res} dropped 0.7 cm^{-1} on cooling, a similar effect was seen by Holah *et al.*[31]

Optical Elements	Channel 1	2	3	4
Common elements				
Vacuum window[a]	0.93	0.96	0.93	0.90
0.038 cm of polypropylene				
Horn lens[a]	0.92	0.90	0.86	0.83
1 cm of polyethylene				
Low pass[a]	0.88	0.85	0.60	0.27
0.32 cm of Fluorogold				
0.32 cm of black polyethylene				
Low-frequency channels				
Dichroic,[b] ICM 2	0.82T	0.62R	—	—
Low pass	0.90 (2.54 cm)	0.78 (1 cm)	—	—
Fluorogold				
DQW[c] 2	0.92	—	—	—
DQW[c] 3	—	0.84	—	—
High-frequency channels				
Dichroic,[b] ICM 6	—	—	0.72T	0.90R
DQW[c] 4	—	—	0.19	—
Cochise[d]	—	—	—	0.68
Optical element efficiency[e]	0.51	0.30	0.07	0.12

[a]Fluorogold and black polyethylene are at 4.2 K, polyethylene is at 100 K, and polypropylene is at ambient temperature. Some transmissions are greater than $1 - (n-1)^2/(n+1)^2$, where n is the index, because of constructive interference. The values quoted are for the average transmission.

[b]The radiation on the dichroics is incident at 45°; T denotes the transmission and R the reflection. The ICM characteristics are given in Table 1. The values are for peak transmission.

[c]These filters are shown in Fig. 7. The values are for the peak transmission.

[d]Cochise is a commercial inductive mesh filter.[15]

[e]Product of the column entries. It does not include the coupling to the bolometers (≈ 0.7) or the efficiency of the lightguide (≈ 0.5), both of which are frequency dependent.

6. Assembly of the Radiometer Optics

Many of the filters described above are used in the radiometer as shown in Figs. 9 and 10; Table 4 lists the filter elements for each channel. The DQW's are thermally sunk to the 0.24-K stage with a small piece of indium, and the ICM's are held in place with aluminum tape. Since the loading on the detectors does not change over a period of days, we deduce that the filter elements reach a steady temperature.

As noted above, the blocking of high-frequency radiation is critical. While the passbands are defined by the ICM's and DQW's, the blocking is provided by absorption filters. Black polyethylene,[32] 0.32 cm thick, is used to block radiation from 100 cm^{-1} through the visible, while Fluorogold,[33] 0.32 cm thick, is used for the lower frequencies. (Fluorogold, glass-fiber impregnated Teflon, is known to have a transmission window somewhere above 200 cm^{-1}.[34]) Both are thermally sunk to 4.2 K with an indium gasket. In a separate experiment with a 1.53-cm-diameter lightguide and the same filter combination, the center of the Fluorogold was measured to be 4.3 K. Further high-frequency blocking for channels 1 and 2 is provided by 2.54 and 1.0 cm of Fluorogold, respectively, these filters are thermally sunk to 0.24 K.

7. Performance of the Filter Set

The performance of the filter system as a whole must be carefully characterized for our CMB anisotropy experiment because the passbands lie in a spectral region of low astrophysical flux. At frequencies below 1.4 cm^{-1}, transmittance is cut off by the geometric size of the optics. Additionally, the flux from known astrophysical sources is negligible. At fre-

quencies greater than 20 cm^{-1}. Sky dust have surface brightnesses that rise faster than ν^3 and are strong sources through the entire IR band. To provide sufficiently good upper limits on filter leakage throughout the IR, several types of measurement must be combined.

In the 2–30-cm^{-1} range the FTS provides measurements that have a dynamic range of $\sim 10^4$ from which upper limits on the out-of-band rejection are obtained. To supplement the FTS measurements, additional filters have been used. In particular, a thick grill filter can block the passband and transmit at high frequencies.[35] Using one of these between the radiometer and a modulated 1200-K source permits us to place sensitive upper limits on the leakage from 30 cm^{-1} to the visible. Even this technique cannot provide us with a sufficiently low limit to the leakage to guarantee that we are not sensitive to interplanetary dust in the form of zodiacal light at 500 cm^{-1}. The best limit comes from an analysis of the inflight data from the zodiacal plane.

To quantify the filter performance, we model the radiometer response to various sources. For the sake of bookkeeping the expected response is divided into an in-band portion, which comes from a healthy swath around the response maximum, and a full-band portion, which ranges from 1.4 cm^{-1} up to a partition is motivated by the observation that the integral of a source spectrum over the noise in the measurement at frequencies above the passband even at the 10^{-4} level may not be negligible. The possibility of a contribution at levels below the sensitivity of the FTS measurements must be accounted for in the determination of the response. The term high-frequency leakage is reserved for describing a response to radiation outside the spectral region measured with the FTS.

The response integrals given in Table 5 are of the form

$$R = \int_{\nu_l}^{\nu_u} I(\nu)F(\nu)\mathrm{d}\nu,$$

where $F(\nu)$ is the measured, normalized filter response, $I(\nu)$ is the source spectrum, and ν_l and ν_u are the lower and upper frequency limits. The source spectra are (1) a Rayleigh–Jeans emitter,

$$B(\nu, T) = 2kcT\nu^2, \qquad \frac{\mathrm{d}B(\nu, T)}{\mathrm{d}T} = 2kc\nu^2,$$

(2) a Rayleigh–Jeans emitter times $\epsilon_0\nu^2$, where $\epsilon_0 = 1$

Table 5. Passband Characteristics

	Channels			
	1	2	3	4
	In-Band[a] (cm^{-1})			
Integrals[b]	4–8	6–13.5	11–20	19–26
Over dCMB/dT				
In-band (W/cm^2 sr K)	1.78×10^{-11}	2.94×10^{-11}	6.07×10^{-12}	—
$\langle\nu\rangle$ [$\Delta\nu$] (cm^{-1})	5.67 (1.34)	9.27 (2.24)	16.0 (1.84)	—
Limit on % out of band[c]	<1	<1	19	—
Value for data analysis[d]	1.79×10^{-11}	2.96×10^{-11}	6.57×10^{-12}	—
Error	$\pm 0.07 \times 10^{-11}$	$\pm 0.07 \times 10^{-11}$	$\pm 0.5 \times 10^{-12}$	—
$\langle\nu\rangle$ (cm^{-1})	5.68 ± 0.07	9.26 ± 0.07	15.2 ± 0.8	—
Over dRJ/dT				
In-band (W/cm^2 sr K)	3.61×10^{-11}	1.67×10^{-10}	4.22×10^{-10}	5.56×10^{-10}
$\langle\nu\rangle$ [$\Delta\nu$] (cm^{-1})	5.73 (1.33)	9.51 (2.23)	16.4 (1.90	22.5 (1.33)
Limit on % out of band[c]	2	<1	3	<1
Value for data analysis[d]	3.63×10^{-11}	1.68×10^{-10}	4.27×10^{-10}	5.67×10^{-10}
Error	$\pm 0.15 \times 10^{11}$	$\pm 0.07 \times 10^{-10}$	$\pm 0.17 \times 10^{-10}$	$\pm 0.23 \times 10^{-10}$
$\langle\nu\rangle$ (cm^{-1})	5.78 ± 0.07	9.54 ± 0.07	16.5 ± 0.1	22.5 ± 0.1
Over d(ν^2RJ)/dT				
In-band (W/cm^2 sr K)	1.20×10^{-9}	1.52×10^{-8}	1.13×10^{-7}	2.82×10^{-7}
$\langle\nu\rangle$ ($\Delta\nu$) (cm^{-1})	5.83 (1.25)	9.68 (2.09)	16.5 (1.86)	22.6 (1.32)
Limit on % out of band[c]	11	5	7	3
Value for data analysis[d]	1.24×10^{-9}	1.55×10^{-8}	1.17×10^{-7}	2.85×10^{-7}
Error	$\pm 0.05 \times 10^{-9}$	$\pm 0.06 \times 10^{-8}$	$\pm 0.05 \times 10^{-7}$	$\pm 0.11 \times 10^{-7}$
$\langle\nu\rangle$ (cm^{-1})	6.08 ± 0.25	9.87 ± 0.2	16.9 ± 0.4	22.7 ± 0.1

[a]Defined in text: full-band − in-band = out-of-band.
[b]dCMB/dT is the derivative of the Planck function evaluated at $T = 2.735$, dRJ/dT is the derivative of a Rayleigh–Jeans emitter, and dν^2RJ/dT is simply ν^2 times dRJ/dT. The units of all are in W/cm^2 sr K.
[c]The value is 100× full-band response minus in-band response divided by in-band response.
[d]The value for data analysis includes our estimate of the proper weighting for the in-band and out-of-band integrals as discussed in Section 7.

$$B(\nu, T) = 2hc^2\nu^3 \frac{1}{[\exp(hc\nu/kT) - 1]},$$

$$\frac{dB(\nu, T)}{dT} = \frac{2h^2c^3\nu^4}{kT^2} \frac{\exp(hc\nu/kT)}{[\exp(hc\nu/kT) - 1]^2},$$

where $T = 2.735$ K, the temperature of the CMB; $[dB(\nu, T)]/dT$ is maximum at 7 cm^{-1}. In all expressions, k is Boltzmann's constant, h is Planck's constant, c is the speed of light, ν is in inverse centimeters, and the units are in W/cm^2 srK. The effective frequency and bandwidth are computed. They are given by

$$\langle\nu\rangle = \frac{\int \nu F(\nu) I(\nu) d\nu}{\int F(\nu) I(\nu) d\nu}, \qquad \Delta\nu = \frac{\int I(\nu) F(\nu) d\nu}{I(\langle\nu\rangle)}.$$

The errors in the integrals can come from frequency errors, insufficient resolution in the FTS, and insufficient sensitivity. To estimate the first two errors, we shifted the spectra by one resolution bin and recalculated the integrals. In all cases the values changed by less than 4%. The errors resulting from the finite sensitivity are more difficult to compute because the full-band integrals are an upper true value of the integral we choose $0.65I_{in} + 0.35I_{full}$ with an uncertainty of $0.7(I_{full} - I_{in})/2$. The prefactors are our estimate of the proper weighting. The determination of $\langle\nu\rangle$ and $\Delta\nu$ are treated in a similar fashion.

The choice of the cutoff frequency is crucial. Using a thick grill filter, we find that there is no response to radiation with $\nu > 24$ cm^{-1} in channel 1. In addition, from the product of the responses of the individual filters, we find that radiation with $\nu > 24$ cm^{-1} is cut off. For channels 2, 3, and 4 the cutoff is where the high-frequency blocking filter transmittance is computed to be less than the noise level of the FTS spectrum. When we use the Fluorogold characteristics in Halpern *et al.*[1] and our own measured black polyethylene characteristics [power absorption coefficient $\alpha(\nu) = 0.0015\nu^2$], the resulting cutoff frequencies are 32, 48, 48 cm^{-1}. At 48 cm^{-1} the transmittance of 0.32 cm of cold Fluorogold drops ≈ 4 dB/wave number.

The finite transmittance of channel 3 between 20 and 35 cm^{-1} is real, as one verifies by measuring the spectrum with the $\nu_c = 24$-cm^{-1}-thick grill filter in place. It is also easy to see the second harmonic of channel 4 with this method. Additional tests with a $\nu_c = 40$-cm^{-1}-thick grill filter reinforce these results and show that there is no high-frequency leakage in channel 2.

Table 5 shows that the in-band integrals are repre-

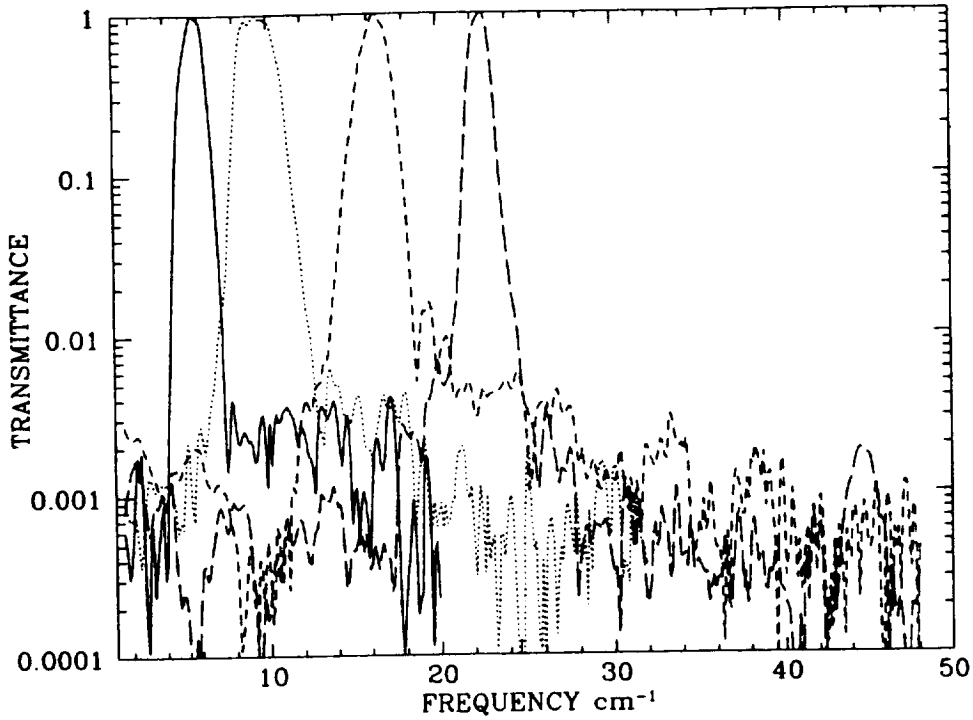

Fig. 11. Normalized transmittance of the radiometer depicted in Fig. 9. The response to a Rayleigh–Jeans source is shown. The band-defining filters are at 0.24 K. Solid curve, channel 1; dotted curve, channel 2; dashed curve, channel 3; long-dashed curve, channel 4. The long high-frequency slope of channel 3 and the second harmonic of channel 4 are evident. The noise level of the measurement is under 1 part in 1000, and the resolution is 0.125 cm^{-1}. These data have been corrected for the time constants of the bolometer. We obtained the numbers in Table 5 by integrating the various sources over these spectra.

sentative of the total response with two exceptions. The channel 3 response to the CMB has a possible 19% contribution from low frequencies. To improve the limit, the normalized response at 2 cm^{-1} would have to be lower than the measured value of 0.003 (see Fig. 11). We cannot be certain that there is no low-frequency leakage. The channel 1 response to a ν^4 emitter can have a contribution of as high as 11% from frequencies near 20 cm^{-1} based on the noise level of the direct measurements. Ideally one would test for a response with a 15-cm^{-1}-thick high-pass grill filter, but this has not been done.

The flight data provide another limit on the high-frequency leakage. The rotation of the instrument modulates any interplanetary dust signal. The expected level of dust emission in our passbands is small.[1,36] Since the blocking properties of Fluorogold are measured to be as high as 100 cm^{-1}, any leakage must come from above this. Thus, if there is no signal correlated with ecliptic latitude, there is a strong case that there is no leakage. An analysis of 9 min of data from channel 3 and 4 from a flight made in October 1989 shows that any such signal is less than ≈ 0.07 of the in-band galactic signal at $b_{II} = 0°$, $l_{II} = 45°$. In other words the integral of all emissions from $\nu > 50$ cm^{-1} contributes less than 7% of the expected in-band signal.

8. Conclusions

We have presented results on cryogenic ICM's that are in spirit similar to but in detail differ from the results of previous researchers. Most of the difference is attributed to the thickness of the Mylar substrate. These data aid in choosing optimal design parameters and provide tests for the frequency-selective-surface programs.

We have also shown that for far-IR experiments it is barely adequate to measure the filter response to 1 part in 1000 to constrain contributions from IR astrophysical sources. High-frequency leakage has plagued a number of experiments; methods for measuring it and detecting it have been presented.

Research on the individual filters and measurements of the composite set have been in progress at MIT since 1983. Many people contributed to the effort. We thank Lynn K Deutsch, Bob Radway and the MIT Microelectronics Laboratory, Deborah Dougherty, David Shoemaker, Ron Dagistino, Nergis Maleva, and Jason Puchalla. Mark Dragovan and Jeff Patterson of Princeton University kindly loaned their set of thick grill filters. We thank Ed Wollack and John Kovac for a number of useful conversations.

Lyman Page was generously supported by a NASA Graduate Student Research Program fellowship during much of this research. This research was also supported in part by NASA grant NAGW-1841 and the National Science Foundation.

References and Notes

1. M. Halpern, R. Benford, S. Meyer, D. Muehlner, and R. Weiss, "Measurements of the anisotropy of the cosmic background radiation and diffuse galactic [illegible] submillimeter wavelengths," Astrophys. J. **332**, 596–614 (1988).
2. P. de Bernardis, S. Masi, B. Melchiorri, F. Melchiorri, and G. Moreno, "Diffuse galactic and extragalactic radiation in the far-infrared," Astrophys. J. **278**, 150–155 (1984).
3. M. L. Fischer, D. C. Alsop, E. S. Cheng, A. C. Clapp, D. A. Cottingham, J. O. Gundersen, T. C. Koch, E. Kreysa, P. R. Meinhold, A. E. Lange, P. M. Lubin, P. L. Richards, and G. F. Smoot, "A bolometric millimeter-wave system for observations of anisotropy in the cosmic microwave background radiation on medium angular scales," Astrophys. J. **388**, 242–252 (1992).
4. L. A. Page, E. S. Cheng, and S. S. Meyer, "A large-scale cosmic microwave background anisotropy measurement at millimeter and submillimeter wavelengths," Astrophys. J. Lett. **355**, L1–L4 (1990).
5. R. Ulrich, "Far-infrared properties of metallic mesh and its complementary structure," Infrared Phys. **29**, 37–55 (1967).
6. R. Ulrich, "Effective low-pass filters for far infrared frequencies," Infrared Phys. **7**, 65–74 (1967).
7. R. Ulrich, "Interference filters for the far infrared," Appl. Opt. **7**, 1987–1996 (1968).
8. D. D. Nolte, A. E. Lange, and P. L. Richards, "Far-infrared dichroic bandpass filters," Appl. Opt. **24**, 1541–1545 (1985).
9. T. Timusk and P. L. Richards, "Near millimeter wave bandpass filters," Appl. Opt. **20**, 1355–1360 (1981).
10. G. D. Holah, B. Davis, and N. D. Morrison, "Narrow-bandpass filters for the far-infrared using double-half-wave designs," Infrared Phys. **19**, 639–647 (1979).
11. M. Dragovan, "Cryogenic metal mesh bandpass filters for submillimeter astronomy," Appl. Opt. **23**, 2798–2802 (1984).
12. J. E. Davies, "Bandpass interference filters for very far infrared astronomy," Infrared Phys. **20**, 287–290 (1980).
13. S. S. Meyer, E. S. Cheng, and L. A. Page, "A measurement of the large-scale cosmic microwave background anisotropy at 1.8-millimeter wavelength," Astrophys. J. Lett. **371**, L7–L9 (1991).
14. L. A. Page, E. S. Cheng, and S. S. Meyer, "Resonant cryogenic chopper," Appl. Opt. **31**, 95–100 (1992).
15. Cochise Instruments, P.O. Box 744, Sierra Vista, Ariz. 85636.
16. I. Anderson, "On the theory of self-resonant grids," Bell Syst. Tech. J. **54**, 1725–1731 (1975).
17. S. T. Chase and R. D. Joseph, "Resonant array bandpass filters for the far infrared," Appl. Opt. **22**, 1775–1779 (1983).
18. R. C. Compton, R. C. McPhedran, G. H. Derrick, and L. C. Botten, "Diffraction properties of a bandpass grid," Infrared Phys. **23**, 239–245 (1983).
19. T. R. Schimert, A. J. Brouns, C. H. Chan, and R. Mittra, "Investigations of millimeter-wave scattering from frequency selective surfaces," IEEE Trans. Microwave Theory Tech. **39**, 315–322 (1991).
20. N. Marcuvitz, *Waveguide Handbook* (Peter Peregrinus Ltd. on behalf of the Institution of Electrical Engineers, London, 1986).
21. C. T. Cunningham, "Resonant grids and their use in the construction of submillimeter filters," Infrared Phys. **23**, 207–215 (1983).
22. J. A. Arnaud and F. A. Pelow, "Resonant-grid quasi-optical diplexers," Bell Sys. Tech. J. **54**, 263–283 (1975).
23. R. C. Compton and R. C. McPhedran, "Bandpass filters: theory and experiment," Appl. Opt. **22**, 3920–3921 (1983).
24. RM Associates, 1009 Woodfield Road. Champaign, Ill. 61821-6724.
25. Metallized Products, Inc., 37 East Street, Winchester, Mass. 01890.
26. Emerson & Cuming Inc., Canton, Mass. 02021.
27. D. H. Shoemaker, "A Fourier transform spectrometer for

millimeter and submillimeter wavelengths," M.S. thesis (MIT, Cambridge, Mass., 1980).
28. Infrared Industries, Inc., P.O. Box 989, Santa Barbara, Calif. 93102.
29. P. M. Downey, A. D. Jeffries, S. S. Meyer, R. Weiss, F. J. Bachner, J. P. Donnelly, W. T. Lindly, R. W. Mountain, and D. J. Silversmith, "Monolithic silicon bolometers," Appl. Opt. **23**, 910–914 (1984).
30. L. A. Page, "Absorbtivity of Mylar between 3 and 35 cm^{-1}," to be submitted to Appl. Opt.
31. G. D. Holah, B. Davis, and N. D. Morrison, "Low temperature narrow-bandpass interference filters," Infrared Phys. **18**, 621–625 (1978).
32. J. M. Blea, W. F. Parks, P. A. R. Ade, and R. J. Bell, "Optical properties of black polyethylene from 3 to 4000 cm^{-1}," J. Opt. Soc. Am. **60**, 603–606 (1970).
33. M. Halpern, H. P. Gush, E. Wishnow, and V. De Cosmo, "Far-infrared transmission of some dielectrics at cryogenic various plastics," Appl. Opt. **25**, 565–570 (1986).
34. M. Halpern, "Measurement of the anisotropy of the cosmic background radiation at millimeter wavelengths," Ph.D. dissertation (MIT, Cambridge, Mass., 1983).
35. See Refs. 9 and 20. Thick grill filters are simply aluminum plates with holes drilled in them. Only frequencies with $\nu > 0.586/d$, with d the diameter of the hole in centimeters, will propagate. For example, for $\nu_c = 24\ cm^{-1}$, $d = 0.0244$ cm. Frequencies below ν_c are attenuated at ~30 dB/hole diameter. For all measurements the edges of the filters were sealed in indium to prevent light leaks. We tried these filters as dichroics at 45° incidence. The passband transmittance is only ≈ 0.2 as opposed to ≈ 0.8 for normal incidence.
36. A. Salama, P. Andreani, G. Dall'Oglio, P. deBernardis, S. Masi, B. Melchiorri, F. Melchiorri, G. Moreno, B. Nisini, and K. Shivanandan, "Measurements of near- and far-infrared zodiacal dust emission," Astrophys. J. **92**, 467–474 (1987).

THE ASTROPHYSICAL JOURNAL, 410:L57–L60, 1993 June 20

CROSS-CORRELATION BETWEEN THE 170 GHz SURVEY MAP AND THE *COBE* DIFFERENTIAL MICROWAVE RADIOMETER FIRST-YEAR MAPS

KEN GANGA,[1] ED CHENG,[2] STEPHAN MEYER,[3] AND LYMAN PAGE[1]
Received 1993 January 28; accepted 1993 April 8

ABSTRACT

This *Letter* describes results of a cross-correlation between the 170 GHz partial-sky survey, made with a 3°.8 beam balloon-borne instrument, and the *COBE* DMR "Fit Technique" reduced galaxy all-sky map with a beam of 7°. The strong correlation between the data sets implies that the observed structure is consistent with thermal variations in a 2.7 K emitter. We describe a number of tests of the correlation: (1) A χ^2 analysis applied to the correlation function rules out the assumption that there is no structure in either of the two maps. (2) A second test shows that if the DMR map has structure but the 170 GHz map does not, the probability of obtaining the observed correlation is small. (3) Further analyses support the assumption that both maps have structure and that the 170 GHz–DMR cross-correlation is consistent with the analogous DMR correlation function. (4) Maps containing various combinations of noise and Harrison-Zel'dovich power spectra are simulated and correlated to reinforce the result. Because these two experiments use completely different observing strategies, observing frequencies, and data reduction methods, the correlation provides compelling evidence that both instruments have observed fluctuations consistent with anisotropies in the cosmic microwave background.

Subject heading: cosmic microwave background

1. INTRODUCTION

The recent discovery of anisotropy in the cosmic microwave background (CMB) by the differential microwave radiometer (DMR) aboard NASA's *COBE* satellite (Bennett et al. 1992, hereafter B92; Smoot et al. 1992, hereafter S92; and Wright et al. 1992) provides strong evidence for primordial structure in the CMB. Supporting this claim is an exhaustive battery of checks for possible systematic effects and foreground sources (B92; Kogut et al. 1992).

The 170 GHz survey map (Meyer, Cheng, & Page 1991), covering roughly one-third of the sky with an angular resolution of 3°.8, is an independent set of data with enough sensitivity to confirm the *COBE* DMR detection. We find significant cross-correlation between the survey map and the CMR "Fit Technique" reduced galaxy map (hereafter simply DMR; see B92, § 5.2). Since the 170 GHz map is made with a different observing strategy, uses different data reduction methods, and is sensitive to different Galactic contaminants, the correlation supports the argument for the cosmic origin of the structure seen in the DMR maps. Because of the higher frequency and finer angular resolution, these data may be used to set bounds on the spectrum of the fluctuations, probe the angular dependence of the anisotropy down to 3°.8, and find a more precise value of $Q_{\rm rms-PS}$; future work will address these questions specifically (Bond et al. 1993).

2. THE DATA

The 170 GHz survey experiment and instrument are described in Meyer et al. (1991), Page (1990), Page, Cheng, & Meyer (1990, 1992), and Page et al. (1993). The data were collected in a single balloon flight in 1989 October. The map used in this analysis has had an offset, a dipole, and a model of the Galaxy subtracted in a five-parameter fit of the data with $|b| > 15°$ (see Fig. 1 [Pl. L14]). The best-fit dipole is in the direction of $\alpha = 169°$ and $\delta = -7°.3$ ($l = 267°$, $b = 49°$) in the solar rest frame. A dipole magnitude of 3.25 mK (3.36 mK plus corrections for Earth's motion) is used to calibrate the data. To model the Galaxy, we use a version of the *IRAS* 100 μm map which has had a model of zodiacal dust emission removed (Boulanger 1989) and has been convolved with the survey map beam. The autocorrelation function of the *IRAS* map, scaled by the fit parameter, indicates that interstellar emission is not significant. A similar analysis with the survey's highest frequency channel confirms this. We are confident that Galactic emission accounts for less than 200 $(\mu K)^2$ in the first bin of the correlation function (Fig. 2).

The DMR data used here is the "Fit Technique" reduced galaxy map described in B92, § 2 with a 15° galactic cut. This map and galactic cut are used to minimize the influence of the Galaxy at small Galactic latitudes, as demonstrated in Figure 2 of S92. The total weight of these data is 0.118 $(\mu K)^{-2}$, roughly twice that of the 170 GHz map.

To compare the 170 GHz and DMR data sets, we make a new map called "masked DMR." It is a partial sky map made with only those DMR pixels within the 170 GHz survey coverage. The total weight of the masked DMR map is 0.024 $(\mu K)^{-2}$, about half that of the 170 GHz map.

3. ANALYSIS

The correlation function is given by $C(\theta_A) = (\Gamma_A)^{-1} \sum_{i,j \in A} t_i t'_j w_i w'_j$, where $\Gamma_A = \sum_{i,j \in A} w_i w'_j$, t_i and w_i are the temperature and weight of pixel i in one map, t'_j and w'_j are the temperature and weight of pixel j in the second map, and the sum is taken over all pixels i and j such that the angle between pixels i and j is θ_A. When the autocorrelation is

[1] Joseph Henry Laboratories, Jadwin Hall, Princeton University, Princeton, NJ 08544.
[2] Laboratory for Astronomy and Solar Physics, NASA/Goddard Space Flight Center, Greenbelt, MD 20771.
[3] Massachusetts Institute of Technology, Department of Physics, Room 20F-001, Cambridge, MA 02139.

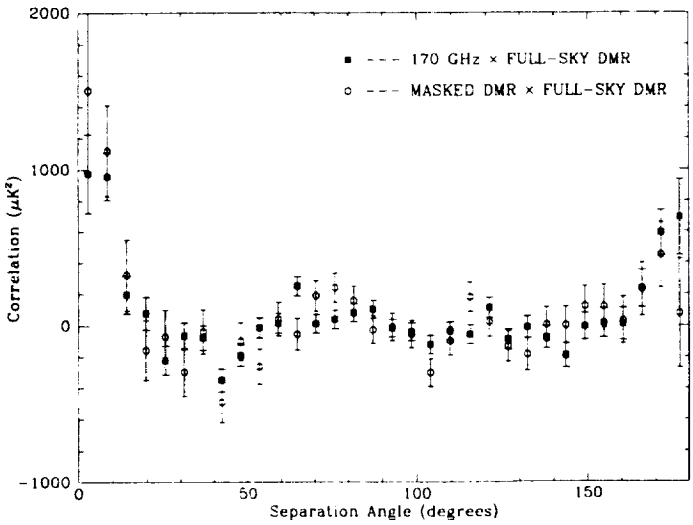

FIG. 2.—The squares are the cross-correlation between the 170 GHz survey map and the *COBE* DMR "Fit Technique" reduced galaxy map for $|b| > 15°$. The circles represent the correlation between the masked DMR map and the full-sky DMR map. The 1 σ error bars reflect pure noise only.

formed, $t'_j = t_j$ and $w'_j = w_j$. The bin size for the correlation function is $180°/32 = 5.^{\circ}63$.

The statistical distribution of $t_i t_j$ for a single pair of pixels is shown in Appendix B to be approximated by a zero-order, modified Bessel function of the second kind. The value of $C(\theta)$ is the weighted mean of data drawn from these distributions; by the central limit theorem, the distribution of $C(\theta)$ is sufficiently Gaussian for our purposes (Bond 1992; see also Cayón, Martínez-González, & Sanz 1991).

The covariance matrices of the correlation functions, the diagonal terms of which are the variances σ_A^2 of the correlation functions, are (see Appendix A)

$$\sum_{AB} = \frac{\delta_{AB}}{\Gamma_A} + \frac{1}{\Gamma_A \Gamma_B} \sum_{i,j \in A} w_i w'_j \times \left(t'_j \sum_{l:i,l \in B} w'_l t'_l + t_i \sum_{k:j,k \in B} w_k t_k \right), \quad (1)$$

and

$$\sum_{AB} = \frac{\delta_{AB}}{\Gamma_A}\left(1 + \frac{\Gamma_A^*}{\Gamma_A}\right) + \frac{1}{\Gamma_A \Gamma_B}\left[\sum_{i,j \in A} w_i w'_j \left(t'_j \sum_{l:i,l \in B} w'_l t'_l + t_i \sum_{k:j,k \in B} w_k t_k \right) + \sum_{j \in 1 \cap 2} w_j^* \sum_{i:i,j \in A} w_i t_i \sum_{l:j,l \in B} w'_l t'_l + \sum_{i \in 1 \cap 2} w_i^* \sum_{j:i,j \in A} w'_j t'_j \sum_{k:i,k \in B} w_k t_k \right]. \quad (2)$$

Equation (1) applies to a cross-correlation, while equation (2) is used for a correlation between two maps in which overlapping pixel values are the same in both maps. Equation (2) thus applies to an autocorrelation as well as to a correlation between a map and a subset of the same map, such as the correlation between the masked DMR map and the full-sky DMR map. $\sum_{j \in 1 \cap 2} w_j^*$ is the sum of w_j over the common coverage of the two maps, and Γ_A^* is the Γ_A one gets for the autocorrelation of the intersection of the two maps. As outlined in the Appendix, these expressions are the convariances if one assumes that both maps have structure in them. If both maps are assumed to have no signal other than noise, only the first (diagonal) terms should be used.

Figure 2 shows the correlation between the 170 GHz survey map and the DMR map along with that of the masked DMR map and the full-sky DMR map. The errors shown are obtained under the assumption that neither map has any real structure. If this assumption is valid, $\chi_\nu^2 = (1/N_{\rm bins}) \sum_A C(A)/\sigma^2(A)$ is about one. The actual value is 5.2. This indicates that the probability of getting the observed level of cross-correlation if both maps have only Gaussian noise is less than 0.5%. This result is reinforced with simulations.

We create maps containing nothing but Gaussian noise following the 170 GHz map weights and correlate them with maps containing nothing but noise following the DMR map weights. The thinnest of the three shaded swaths centered on zero in Figure 3 represents the 1 σ range of results for these correlations, again demonstrating that the observed correlation is quite improbable if both maps simply contain pure noise. From this we infer that our assumption was incorrect and that there must be structure in at least one of the maps.

Next, we assume that the DMR map has structure, but that the 170 GHz map does not. In this case we must use the first two of the three terms in the covariance matrix of equation (1) (we associate the DMR map with the primed weight and temperature values). Because the covariance matrix is no longer diagonal, the simple χ^2 analysis used previously is not valid, since different bins in the correlation function are now correlated. In order to apply a χ^2 test, we find the matrix **T** which diagonalizes the covariance matrix and transform to get a new, diagonal covariance matrix $\mathbf{\Sigma}' = \mathbf{T}^{-1}\mathbf{\Sigma}\mathbf{T}$, and a new correlation function $\mathbf{C}' = \mathbf{TC}$. The errors in the new correlation

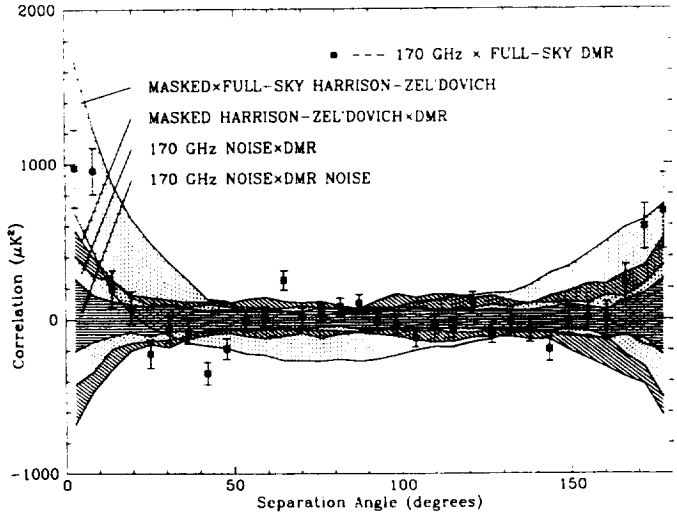

FIG. 3.—The 170 GHz–DMR cross-correlation along with 1 σ distribution of results from simulating and correlating (1) noise governed by the 170 GHz map weights with noise governed by the DMR map weights, (2) noise governed by the 170 GHz map weights with the real DMR map, (3) simulated $Q_{\rm rms-PS} = 17\ \mu$K Harrison-Zel'dovich skies with 170 GHz weights and noise with the real DMR map, and (4) simulated $Q_{\rm rms-PS} = 17\ \mu$K Harrison-Zel'dovich skies with 170 GHz weights and noise and skies with the same underlying structure and DMR weights and noise. These simulations are intended for qualitative comparison with the data.

function are, as before, the square roots of the diagonal terms in the new covariance matrix. In this new space, since the covariance matrix is diagonal, the errors in separate bins of the correlation function are independent, and we can apply a χ^2 test. We find a χ^2_ν of 5.7 for the transformed 170 GHz–DMR cross-correlation, once again indicating that our assumption is incorrect—there must be structure in the survey map. This is the primary conclusion in Meyer et al. (1991). Figure 3 reinforces this result. The second of the three bands centered on zero represents the 1 σ range of results of correlations between the simulated maps with nothing but noise and the real DMR map. Again we see that the observed correlation is quite unlikely if it is assumed that the 170 GHz map has only noise, although because of the covariances a quantitative comparison of the real and simulated correlation functions is not possible.

This leads us to the assumption that there is structure in both maps and requires use of the full covariance matrix for the correlation function. Transforming again as outlined above, we get a χ^2_ν of 2.6, indicating that the function is still inconsistent with zero, this time in accordance with our assumption.

Are the two correlation functions in Figure 2 consistent with each other? To address this question we calculate the full covariance matrices for both correlation functions and transform both according to the transformation that diagonalizes the 170 GHz–DMR correlation function covariance matrix. We now have two transformed correlation functions and corresponding covariance matrices. The covariance matrix corresponding to the 170 GHz–DMR correlation function is diagonal, while the off-diagonal terms in the covariance matrix associated with the masked DMR–full-sky DMR correlation are small. We then define a statistic similar to the χ^2:

$$\xi^2_\nu = \frac{\xi^2}{\nu} = \frac{1}{N_{\rm bins}} \sum_A \frac{[C'_1(A) - C'_2(A)]^2}{\sigma'_1(A)^2 + \sigma'_2(A)^2} ,$$

where $C'_j(A)$ and $\sigma'_j(A)$ are the value and error of the jth transformed correlation function at bin A. ξ^2 is χ^2 distributed; if the statistic is small, the two functions are consistent with each other. We find $\xi^2_\nu = 0.6$, indicating that there is a 90%–95% chance of getting a higher ξ^2. Transforming so that the masked DMR–full-sky DMR covariance matrix is diagonalized again yields $\xi^2_\nu = 0.6$. As a further test of the consistency, Figure 3 shows that the observed cross-correlation is consistent with the 1 σ range of results obtained when simulated Harrison-Zel'dovich skies with $Q_{\rm rms-PS} = 17$ μK and 170 GHz map noise are correlated with the same underlying skies and DMR map noise. A quantitative comparison of the actual cross-correlation and the simulations would be misleading, in this case because the simulations contain "cosmic variance" in the covariance, while the real cross-correlation function does not (see Appendix A).

The widest path about zero in Figure 3 is the result of the same simulated Harrison-Zel'dovich skies with the 170 GHz sky coverage and noise cross-correlated with the DMR map. It indicates that even if two maps have underlying structure with the same rms temperature variations, they still do not correlate as well as the 170 GHz and DMR maps. For a strong correlation, the structure in the two maps must have the same phases and amplitudes.

We are indebted to Dick Bond, Steve Boughn, and David Cottingham for enlightening discussions on statistics and map making. Appendix A grew out of notes Steve Boughn shared with us. We would also like to thank the *COBE* team, especially Chuck Bennett, Gary Hinshaw, Charley Lineweaver, and George Smooth for independently checking the results presented in Figure 2 and thoroughly reading an earlier manuscript. In addition, Gary Hinshaw checked our galaxy subtraction.

This work was supported by the NSF and NASA grant NAGW-1841.

APPENDIX A

COVARIANCE MATRIX OF THE CORRELATION FUNCTION

The standard expression for the covariance matrix of the correlation function $C(\theta_A)$ (see § 3) is $\sum_{AB} = \langle [C(\theta_A) - \langle C(\theta_A)\rangle][C(\theta_B) - \langle C(\theta_B)\rangle]\rangle$, where $\langle \ldots \rangle$ denotes an ensemble average over experiments and all possible universes. In an ideal experiment, the temperature measured in a pixel is the true sky temperature t_i for a particular manifestation of the CMB fluctuations and n_i is the noise in the measurement, $\sqrt{1/w_i}$. To avoid a profusion of symbols, let $t_i \to t_i + n_i$, $t'_j \to t'_j + n'_j$, substitute in $\langle C(\theta_A)\rangle$, and expand fourth-order terms with $\langle x_i x'_j x_k x'_l\rangle = \langle x_i x'_j\rangle\langle x_k x'_l\rangle + \langle x_i x_k\rangle\langle x'_j x'_l\rangle + \langle x_i x'_l\rangle\langle x'_j x_k\rangle$, to obtain

$$\sum_{AB} = \frac{1}{\Gamma_A \Gamma_B} \sum_{i,j\in A;\, k,l\in B} w_i w'_j w_k w'_l (\langle t_i t_k\rangle\langle t'_j t'_l\rangle + \langle t_i t'_l\rangle\langle t'_j t_k\rangle + \langle t_i t_k\rangle\langle n'_j n'_l\rangle + \langle t_i t'_l\rangle\langle n'_j n_k\rangle + \langle t'_j t'_l\rangle\langle n_i n_k\rangle + \langle t'_j t_k\rangle\langle n_i n'_l\rangle + \langle n_i n_k\rangle\langle n'_j n'_l\rangle + \langle n_i n'_l\rangle\langle n'_j n_k\rangle) . \quad (3)$$

The first two terms in the above expression are the "theory-theory" or "cosmic variance" terms, the next four are the "theory-noise" terms, and the last two are the "noise-noise" terms.

If the noise in the two maps is uncorrelated and the noise within the maps is uncorrelated from bin to bin, as in a cross-correlation, then $\langle n_i n'_j\rangle = 0$ and $\langle n_i n_j\rangle = \delta_{ij}/w_i$, and equation (3) reduces to

$$\sum_{AB} = \frac{1}{\Gamma_A \Gamma_B} \left\{ \sum_{i,j\in A} w_i w'_j \left[\sum_{k,l\in B} w_k w'_l (\langle t_i t_k\rangle\langle t'_j t'_l\rangle + \langle t_i t'_l\rangle\langle t'_j t_k\rangle) + \sum_{k;j,k\in B} w_k \langle t_i t_k\rangle + \sum_{l;i,l\in B} w'_l \langle t'_j t'_l\rangle \right] \right\} + \frac{\delta_{AB}}{\Gamma_A} . \quad (4)$$

If the two maps have common values, as in an autocorrelation or when we correlate a map with a subset of the same map, equation (3) becomes

$$\sum_{AB} = \frac{1}{\Gamma_A \Gamma_B}\left\{\sum_{i,j\in A} w_i w_j'\left[\sum_{k,l\in B} w_k w_l'(\langle t_i t_k\rangle\langle t_j' t_l'\rangle + \langle t_i t_l'\rangle\langle t_j' t_k\rangle) + \sum_{k;j,k\in B} w_k\langle t_i t_k\rangle + \sum_{l;i,l\in B} w_l\langle t_j t_l\rangle\right]\right.$$
$$\left. + \sum_{i\in 1\cap 2} w_i^* \sum_{j,k;i,j\in A;\, i,k\in B} w_j' w_k\langle t_j' t_k\rangle + \sum_{j\in 1\cap 2} w_j^* \sum_{i,l;i,j\in A;\, j,l\in B} w_i w_l'\langle t_i t_l'\rangle\right\} + \frac{\delta_{AB}}{\Gamma_A}\left(1 + \frac{\Gamma_A^*}{\Gamma_A}\right). \quad (5)$$

The differences in equations (4) and (5) reflect the fact that in a cross-correlation there are twice as many independent pairs of pixels as in an auto-correlation.

As noted above, these expressions are obtained by hypothesizing an ensemble of universes and therefore contain cosmic variance terms. While this is useful for comparing data to models, herein we are concerned only with comparing two data sets, both of which are maps of the same underlying structure. In this case we average not over an ensemble of universes and experiments, but only over an ensemble of experiments. The results are equations (1) and (2). Note that we are using the measured temperature value of a pixel as an approximation of its true (noiseless) value. This consistently overestimates the diagonal terms of the covariance matrix.

APPENDIX B

ALTERNATE DERIVATION CORRELATION FUNCTION NOISE ERRORS

If a map contains only noise, the correlation function is the average of a number of products of temperatures, each of which is drawn from a Gaussian distribution. The probability of getting a certain t_A and t_B within the ranges Δt_A and Δt_B is then

$$D(t_A, t_B)\Delta t_A \Delta t_B = \frac{e^{-t_A^2/2\sigma_B^2}}{\sigma_A\sqrt{2\pi}}\Delta t_A \frac{e^{-t_B^2/2\sigma_B^2}}{\sigma_B\sqrt{2\pi}}\Delta t_B .$$

By transforming such that $v = t_A t_B$, $|u| = t_A^2$ and integrating over u, one can show that $D(t_A t_B) = K_0(|t_A t_B|/\sigma_A\sigma_B)/\pi\sigma_A\sigma_B$ (see Gradshteyn & Ryzhik 1980, p. 340), K_0 being a zero-order, modified Bessel function of the second kind.

The distribution of a sum of terms $D(\sum_{i=1}^N f_i) = (\sqrt{2\pi})^{N-1} D(f_1) * D(f_2) * D(f_3) * \ldots * D(f_N)$, where $*$ denotes a convolution (see, for example, Butkov 1968). The convolution theorem states that the Fourier transform of the distribution of this sum is

$$\mathcal{F}\left\{D\left(\sum_{i=1}^N f_i\right)\right\}\{k\} = (\sqrt{2\pi})^{N-1}\prod_{i=1}^N \mathcal{F}\{D(f_i)\}\{k\} ,$$

where $\mathcal{F}\{D(f)\}\{k\}$ denotes the Fourier transform of $D(f)$. Thus,

$$\mathcal{F}\left\{D\left(\sum_{i=1}^N t_{Ai} t_{Bi}\right)\right\}\{k\} = (\sqrt{2\pi})^{N-1}\prod_{i=1}^N \mathcal{F}\left\{\frac{1}{\pi\sigma_{Ai}\sigma_{Bi}} K_0\left(\frac{|t_{iA} t_{Bi}|}{\sigma_{iA}\sigma_{Bi}}\right)\right\}\{k\} .$$

The central limit theorem requires that the convolution of a large number of functions approach a Gaussian. We can write the Fourier transform of this as $\mathcal{F}\{D(\sum_{i=1}^N f_i)\}\{k\} = (2\pi)^{-1/2} e^{-k^2\sigma^2/2}$. Recall that multiplying a Gaussian by a constant c changes σ to $c \times \sigma$, and that $\mathcal{F}\{a\pi^{-1}K_0(ax)\}\{k\} = \{2\pi[1 + (k/a)^2]\}^{-1/2}$. We can expand both expressions for the Fourier transform of the sum and, equating terms of second order in k, find that $\sigma = \sqrt{1/\Gamma}$, just the "noise-noise" errors found in Appendix A.

REFERENCES

Bennett, C. L., et al. 1992, ApJ, 396, L7 (B92)
Bond, J. R. 1992, private communication
Bond, J. R., et al. 1993, in preparation
Boulanger, F. 1989, IPAC (Infrared Processing and Analysis Center, CIT), private communication
Butkov, E. 1968, Mathematical Physics (Reading, MA: Addison-Wesley)
Chan, F. K., & O'Neill, E. M. 1975, EPRF technical report 2-75 (CSC)
Cayón, L., Martínez-González, E., & Sanz, J. L. 1991, MNRAS, 253, 599
Gradshteyn, I. S., & Ryzhik, I. M. 1980, Table of Integrals, Series, and Products (New York: Academic)
Kogut, A., et al. 1992, ApJ, 401, 1
Meyer, S. S., Cheng, E. S., & Page, L. 1991, ApJ, 371, L7
O'Neill, E. M., & Laubscher, R. E. 1976, NEPRF technical report 3-76 (CSC)
Page, L. A. 1990, Ph.D. thesis, Massachusetts Inst. of Technology
Page, L. A., Cheng, E. S., & Meyer, S. S. 1990, ApJ, 355, L1
———. 1991, Appl. Opt., 31,
Page, L. A., et al. 1993, Appl. Opt., submitted
Smoot, G. F., et al. 1992, ApJ, 396, L1 (S92)
Torres, S., et al. 1989, in Data Analysis in Astronomy 1989, ed. V. Di Gesù, L. Scarsi, & M. C. Maccarone (New York: Plenum), 319
Wright, E. L., et al. 1992, ApJ, 396, L13

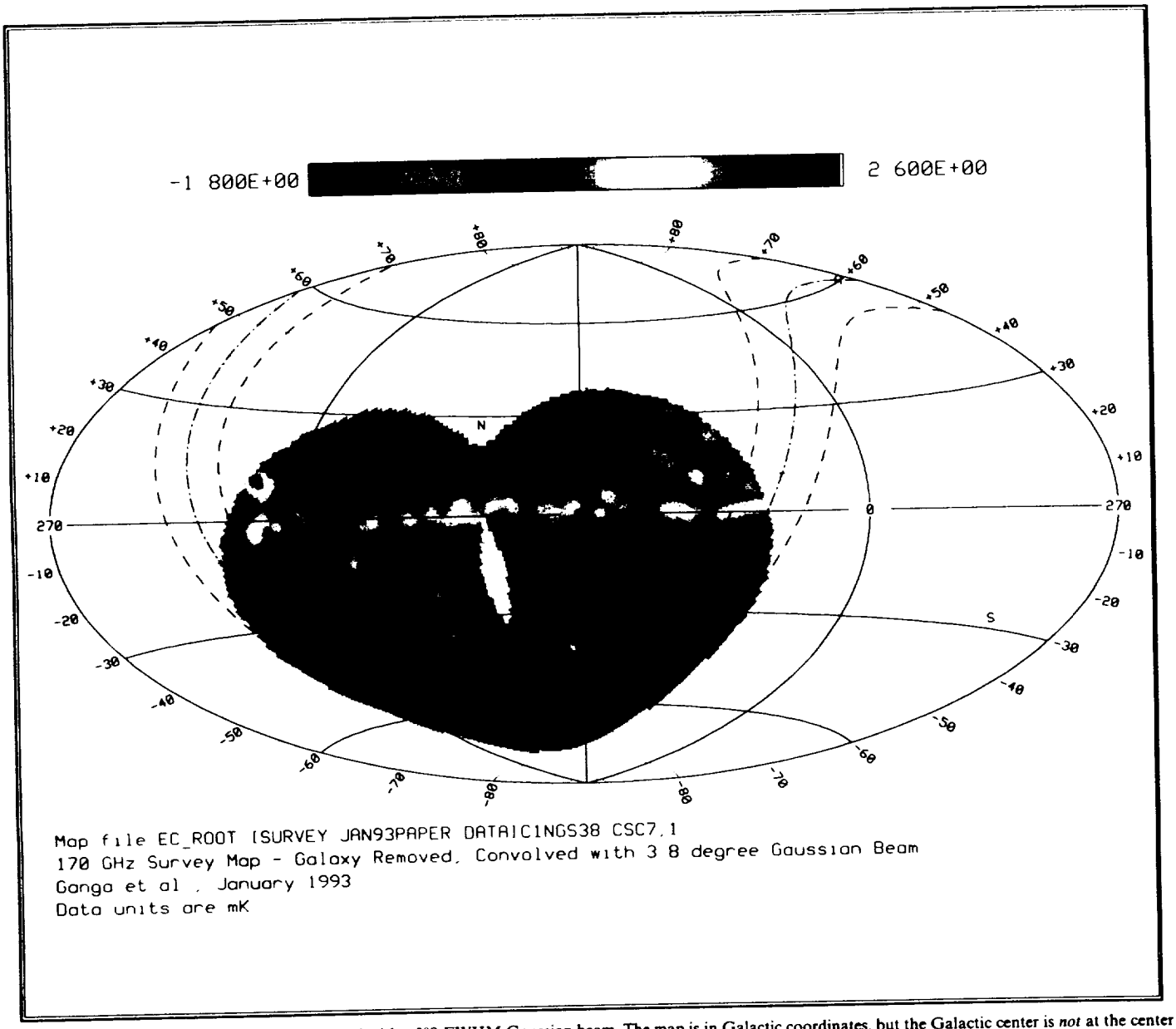

FIG. 1.—The 170 GHz survey data convolved with a 3°8 FWHM Gaussian beam. The map is in Galactic coordinates, but the Galactic center is *not* at the center of the map. A number of gaps in the map due to periodic calibrations have been smeared over by the convolution. The map is binned on the sky in equatorial coordinates with the spherical cube scheme ("CSC format"; Chan & O'Neill 1975, O'Neill & Laubscher 1976, and Torres et al. 1989) in 1°3 × 1°3 pixels, yielding a set of points on the sphere, each with an associated temperature and a statistical weight, $1/\sigma^2$. The total weight, the sum of the individual pixel weights, for $|b| > 15°$, is 0.051 $(\mu K)^{-2}$. The map is not weighted evenly; most of the perceptible variation is due to variation in the weights. The map has greatest sensitivity near the north celestial pole, marked with an "N," and at a declination of $-10°$, marked by the lower dotted line. The bright spot at $l \sim 190°$, $b \sim 10°$ is Jupiter. In the cross-correlation analysis, the data were not smeared, and only data with $|b| > 15°$ are considered. The residual Galactic signal at $|b| < 15°$ indicates that the index and/or temperature of the dust for $|b| > 15°$ is different from that of the dust on the plane.

THE ASTROPHYSICAL JOURNAL, 422:L37–L40, 1994 February 20

A MEASUREMENT OF THE MEDIUM-SCALE ANISOTROPY IN THE COSMIC MICROWAVE BACKGROUND RADIATION

E. S. CHENG,[1] D. A. COTTINGHAM,[2] D. J. FIXSEN,[3] C. A. INMAN,[4] M. S. KOWITT,[1] S. S. MEYER,[4]
L. A. PAGE,[5] J. L. PUCHALLA,[4] AND R. F. SILVERBERG[1]
Received 1993 May 19; accepted 1993 November 24

ABSTRACT

Observations from the first flight of the Medium Scale Anisotropy Measurement (MSAM) are analyzed to place limits on Gaussian fluctuations in the cosmic microwave background radiation (CMBR). This instrument chops a 30′ beam in a three-position pattern with a throw of ±40′; the resulting data is analyzed in statistically independent single- and double-difference data sets. We observe in four spectral channels at 5.6, 9.0, 16.5, and 22.5 cm^{-1}, allowing the separation of interstellar dust emission from CMBR fluctuations. The dust component is correlated with the IRAS 100 μm map. The CMBR component has two regions where the signature of an unresolved source is seen. Rejecting these two source regions, we obtain a detection of fluctuations which match CMBR in our spectral bands of $0.6 \times 10^{-5} < \Delta T/T < 2.2 \times 10^{-5}$ (90% CL interval) for total rms Gaussian fluctuations with correlation angle 0°.5, using the single-difference demodulation. For the double difference demodulation, the result is $1.1 \times 10^{-5} < \Delta T/T < 3.1 \times 10^{-5}$ (90% CL interval) at a correlation angle of 0°.3.

Subject headings: cosmology: cosmic microwave background — cosmology: observations

1. INTRODUCTION

Measurements of the anisotropy of the cosmic microwave background radiation (CMBR) on 0°.5 angular scales have received greater attention (Efstathiou, Bond, & White 1992; Gorski 1993; Kashlinsky 1992) after the *COBE* detection on large angular scales (Smoot et al. 1992). The large-scale measurement sets an amplitude for the unperturbed primeval density fluctuation spectrum; at scales between 0°.5 and 2°, the anisotropy could be enhanced through Doppler and heating effects. The first flight of the Medium Scale Anisotropy Measurement (MSAM) has led to a detection of brightness fluctuations at 0°.5 which are consistent with a CMBR spectral signature. The instrument, observations, analysis, and results are described below.

2. INSTRUMENT DESCRIPTION

MSAM is a balloon-borne 30° off-axis Cassegrain telescope consisting of a 1.4 m aluminum primary, a 0.27 m nutating secondary, and a four-channel radiometer previously flown in the Far Infra-Red Survey experiment (Page 1989; Page, Cheng, & Meyer 1990; Meyer, Cheng, & Page 1991). The beam size of the telescope is 30′. The secondary executes a 2 Hz, four-position, square-wave chop (i.e., center, left, center, right) with an amplitude of ±40′ on the sky. Each position consists of a 23 ms transition and a 102 ms stable integration where the rms position jitter is less than 4″. The bolometric detectors have bandpass central frequencies of 5.6, 9.0, 16.5, and 22.5 cm^{-1} each with ~ 1 cm^{-1} bandwidth (Page et al. 1993). The bolometer output is sampled synchronously at 32 Hz with an integrating A/D converter.

The telescope is shielded with aluminized panels so that the dewar horn, the secondary, and the geometrically illuminated portion of the primary have no view of Earth or the lower part of the flight train. The edge of the balloon, as seen by the telescope, extends about 25° from the zenith. Ground-based measurements of the sidelobe pattern show the response to the ground to be less than −60 dB of the central lobe of the antenna pattern.

3. OBSERVATIONS

The package was launched from Palestine, Texas at 0059 UT 1992, June 5 and reached float altitude of 38 km at 0507 UT. The flight ended with sunrise on the package at 1056 UT. During the flight, we scanned Jupiter and Saturn to calibrate the instrument and to map the antenna pattern, scanned over the center of the Coma Cluster to search for the Sunyaev-Zel'dovich effect (which will be reported in a future *Letter*), and integrated for 4.9 hr on a patch of sky near the north celestial pole to search for CMBR anisotropy.

The CMBR observations are made by looking 8° above the north celestial pole, and holding elevation constant while scanning in azimuth ±45′ with a period of 1 minute. We start with the center of the scan 21′ to the east of the meridian and track for 20 minutes; at this point the center of the scan is 21′ to the west of the meridian. We then pause for about 40 s to record an image with the star camera and correct for gyro drift, and begin a new 20 minute scan 42′ to the east of the previous scan. Thus, half of each 20 minute scan overlaps the following scan. This observation strategy minimizes motion of the telescope relative to Earth and the atmosphere and therefore also minimizes any systematic contribution from these sources. We completed six scans from 0419 to 0622 UT, observed the Coma Cluster for 40 minutes, and completed an additional eight scans from 0701 to 0950 UT, for a total of 14 scans. This covers two strips at declination 82°.0, from right ascension 14^h.44 to

[1] NASA/Goddard Space Flight Center, Code 685.0, Greenbelt, MD 20771.
[2] Global Science and Technology, Inc., NASA/GSFC Code 685.0, Greenbelt, MD 20771.
[3] Applied Research Corporation, NASA/GSFC Code 685.3, Greenbelt, MD 20771.
[4] Massachusetts Institute of Technology, Room 20B-145, Cambridge, MA 02139.
[5] Princeton University Physics Department, Princeton, NJ 08544.

16^{h}89, and from 17^{h}18 to 20^{h}33 (J1992.5). We refer to these two segments as the two halves of the flight.

4. DATA ANALYSIS

4.1. *Calibration, Deglitching, and Demodulation*

The instrument is calibrated by in-flight observations of Jupiter before the CMBR scans, and of Saturn after the CMBR scans. We use Jupiter as our definitive calibration, with Saturn as a comparison. For the night of observation, the apparent diameter of Jupiter is 35″, and the diameter of the disk of Saturn is 17″.6. We take the spectrum of Jupiter from Griffin et al. (1986), from which we derive antenna temperatures for our four channels of 172, 170, 148, and 148 K, respectively. We assume that in our spectral region Saturn has a Rayleigh-Jeans spectrum with a temperature of 133 ± 20 K (Harwit 1988; Lang 1980). No correction is made for the rings of Saturn, which at this frequency add less than 10% in brightness (Hanel et al. 1981). The calibrations on Jupiter and Saturn are consistent in channels 1, 3, and 4. In channel 2, Saturn is dimmer than we expected by a factor of 2. In addition, the offset in channel 2 drifts downward by the same factor over the same period, and the noise also follows this drift. We assume that a postdetection gain drift is responsible for this behavior, and we correct this by multiplying the channel 2 data by a linear function of time to make the Jupiter and Saturn calibrations consistent. With this correction, the offset stability in channel 2 becomes consistent with that of the other channels. The uncertainty in the calibration is 10% (Griffin et al. 1986).

The data contain large spikes, or glitches, at a rate of once per 2–5 s, consistent with cosmic rays striking the detectors (Charakhch'yan et al. 1978). To remove these glitches, we perform a first cut at 10 σ, and then deconvolve with a model of the transfer function of the detectors. The average offset signal in a chop cycle for each half of the flight is then subtracted from all chop cycles in that half, after which two cuts at 3.5 σ are made. About 5% of the data is cut this way.

We estimate instrument noise by forming the autocorrelation of the deglitched data, filtering out 0 Hz and harmonics of 2 Hz, where sky signals appear. This estimate is therefore unaffected by any optical signal. We form this estimate for each 20 minute segment of data which is then propagated through the remaining processing. All χ^2 reported below are with regard to these error bars.

The data are demodulated in two different ways. The first corresponds to summing the periods when the secondary is in the central position, and subtracting the periods when it is to either side; we call this the double-difference demodulation. This demodulation is insensitive to atmospheric gradients. The second demodulation corresponds to differencing the periods when the secondary is to the right from those when it is to the left, and ignoring the periods when the secondary is in the center; we call this the single-difference demodulation. These two demodulations of the data yield statistically independent measurements of the sky. We use the scan over Jupiter to deduce an optimal demodulation of the infrared signal. Each group of four complete chopper cycles (2 s) is averaged together to form a "record." Records for which there are too few samples to form a robust average, due to deglitching or telemetry dropouts, are deleted. The procedure results in a 2% data loss. Each record is then demodulated to produce one single and one double difference observation every 2 s.

This demodulated signal has had a constant offset removed from it in the deglitching process. The size of this offset is approximately 10 mK Rayleigh-Jeans in all four bands, and in both the single- and double-difference demodulation. To remove the drift in this offset, we subtract a slowly varying function of time to minimize the variance of observations of each point in the sky made at different times. The function of time is implemented as a cubic spline with a knot every 2.5 minutes. Each channel and demodulation is treated separately. The two halves of the flight are also treated separately, as they are separated in time and do not overlap on the sky. The drift is $\lesssim$400 μK Rayleigh-Jeans and significant at the 3–8 σ level; thus the offset is constant to about 4%. The reduced χ^2 of these fits range from 0.92 to 1.21.

The data are binned by position on the sky, and by relative angular orientation of the antenna beam with respect to the local tangent to the circle of constant declination at the central beam location. The bin size is 0°.12 in position, and 10° in angular orientation. Records which differ from the median in the bin by more than 3 σ are deleted. Following this, bins containing fewer than 10 records are deleted. The reduced χ^2 of the binned data after removing a mean from each bin ranges from 0.88 to 1.04 for the various channels and demodulations, indicating that our observations of the sky are consistent. The binned data contain 86% of all the data originally taken, with an achieved sensitivity in each of the four channels of 400, 210, 140, and 330 μK s$^{1/2}$ Rayleigh-Jeans. For channels 1 and 2 this is 810 and 1190 μK s$^{1/2}$ CMBR.

4.2. *Spectral Model of the Sky*

To extract the part of the signal due to variations in the CMBR, we fit the data t_{ck} for each channel c and sky bin k to a two-component model:

$$t_{ck} = \int dv F_c(v) \left[D_k \left(\frac{v}{v_0} \right)^{\alpha} B_v(T_D) + t_k \left. \frac{dB_v}{dT} \right|_{T_{\rm CMBR}} \right], \quad (1)$$

where $F_c(v)$ is the spectral response of the instrument, $B_v(T)$ is the Planck function at temperature T, $T_D = 20$ K is the dust temperature, $\alpha = 1.5$ is the spectral index of the dust, $v_0 = 22.5$ cm^{-1} is the reference frequency, $T_{\rm CMBR} = 2.73$ K is the temperature of the CMBR, and D_k and t_k are free parameters. The result is a component sensitive to the CMBR (t_k) and a component sensitive to the dust (D_k). The χ^2 for the fit is 237/292 for the single-difference data, and 454/294 for the double-difference data. T_D and α are fixed for this analysis since varying these parameters by reasonable amounts does not significantly change the CMBR component. Figure 1 shows the dust channel. The superposed curve is an approximation of the expected dust emission produced by convolving our antenna pattern with *IRAS* 100 μm measurements (Wheelock et al. 1991; Wheelock et al. 1993). For the most part, agreement is quite good, but in a few places they differ quite significantly. The scaling of the *IRAS* data is determined by fitting to the dust channel; this scaling is equivalent to an average spectral index between 100 μm and 444 μm (22.5 cm^{-1}) of 1.5 ± 0.2. Figure 2 shows the CMBR component. For clarity, these plots are binned more coarsely than the data we analyzed and do not distinguish between points taken at slightly different declination or antenna orientation.

There are two candidate unresolved sources visible in the CMBR spectral component, ΔT_k, for both the single- and double-difference data. The more prominent source (MSAM 15+82) is located at R.A. 14^{h}92 ± 0^{h}03 in a dust-free region

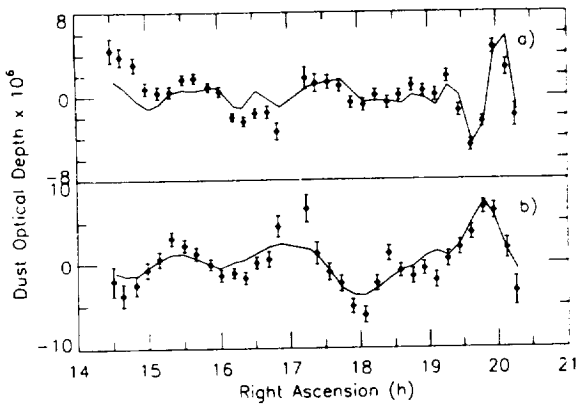

FIG. 1.—Optical depth at 22.5 cm^{-1} of dust component D_k; (*a*) double difference demodulation, (*b*) single difference. Superposed curve is *IRAS* 100 μm data convolved with our antenna pattern; scale is set by fit to our observations.

and has a measured flux density of 4.5 ± 0.7 Jy at 5.6 cm^{-1} (error bar includes calibration uncertainty of 10%). The second, dimmer, candidate (MSAM 19+82) is located at R.A. $19^h29 \pm 0^h03$ and has a measured flux density of 3.6 ± 0.6 Jy at 5.6 cm^{-1}. It is in a region that is somewhat confused by foreground dust emission. We observe at a fixed declination so the declination coordinate for these sources is less well determined, but it is most likely within a beamwidth of the declination of observation, $82°.00 \pm 0°.25$. Each of these sources has a signal which is stationary with respect to the sky (as determined by the various levels of chopping built into our observation strategy) and is detected in multiple channels. The compactness of these sources makes it implausible that they are due to diffraction or sidelobe effects.

We cannot rule out the possibility that these are Galactic bremsstrahlung sources; observations at lower frequency ($\lesssim 3$ cm^{-1}) will shed light on this question. It would be somewhat unexpected for CMBR fluctuations obeying Gaussian statistics to produce such features, and we have performed simulations that indicate that these features are not consistent with the correlation functions considered here. For the detailed discussion in this *Letter*, we have made the assumption that these are indeed unresolved foreground sources. The regions which are contaminated by these sources have been removed from consideration pending further analysis. In particular, only the region $15^h.69 <$ R.A. $< 18^h.55$ is included in the main CMBR

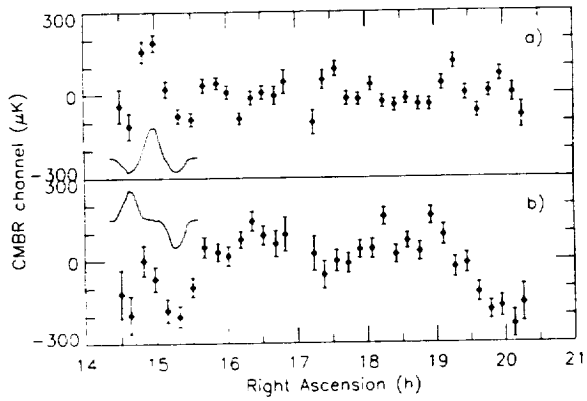

FIG. 2.—CMBR component t_k; (*a*) double difference, (*b*) single difference. Antenna pattern is superposed for reference.

results, though we also include results based on the entire data set. A future *Letter* will address the detailed spectra and possible identification of these sources.

4.3. *Limits on CMBR Anisotropy*

To set limits on the anisotropy of the CMBR, we model the anisotropy $\Delta T(x)$ as a Gaussian random field described by a correlation function $C(|x_1 - x_2|) = \langle \Delta T(x_1) \Delta T(x_2) \rangle$. Our observations have been binned by orientation of the antenna pattern; call the antenna pattern as oriented for the kth observation $H_k(x)$. (Clearly all the functions H_k are translations and rotations of one function H.) Then the signal s_k from CMBR is $s_k = \int dx H_k(x) \Delta T(x)$, and consequently the covariance of the s_k is

$$\langle s_k s_l \rangle = \int dx_1\, dx_2\, H_k(x_1) H_l(x_2) C(|x_1 - x_2|) . \qquad (2)$$

To this signal our instrument adds noise n_k, which has the covariance $\langle n_k n_l \rangle = \delta_{kl} \sigma_k^2$. The instrument noise and sky signal are uncorrelated with each other, so the covariance of our observations $t_k \equiv s_k + n_k$ is just the sum of the covariances of s_k and n_k.

We set limits on the overall amplitude of the correlation function C by using the likelihood ratio statistic (Martin 1971). Let $(W_{kl})^{-1} = \langle s_k s_l \rangle + \sigma_k^2 \delta_{kl}$, and $(W^0_{kl})^{-1} = \sigma_k^2 \delta_{kl}$; then the likelihood ratio λ is

$$\lambda = \left(\frac{\det W}{\det W^0} \right)^{1/2} \exp \left[-\frac{1}{2} \sum_{kl} t_k (W_{kl} - W^0_{kl}) t_l \right] . \qquad (3)$$

Let $\rho_C(\lambda)$ be the probability density function of λ under the hypothesis that the fluctuations obey the correlation function C, and let λ^* be the value of the statistic for our observations. Note that λ, λ^*, and ρ_C all depend on the correlation function, and in particular on its amplitude. Then the 95% confidence level upper limit on the amplitude is that amplitude for which the cumulative distribution function is

$$\int_0^{\lambda^*} d\lambda \rho_C(\lambda) = 0.95 . \qquad (4)$$

Similarly, the 95% lower limit is that amplitude for which this integral is 0.05, if such an amplitude exists. Taken together, these two limits form a 90% confidence interval. We perform the integral in equation (4) by Monte Carlo integration (Press et al. 1986). The amplitudes we quote here are total rms fluctuation, i.e., $[C(0)]^{1/2}$.

Figure 3 shows the upper and lower limits for total rms anisotropy as a function of correlation angle and assuming a Gaussian-shaped correlation function. This uses only the data in the region $15^h.69 <$ R.A. $< 18^h.55$. The single-difference data are most sensitive at $\theta_c = 0°.5$ with a 90% confidence interval of $0.6 \times 10^{-5} < \Delta T/T < 2.2 \times 10^{-5}$. For the double-difference data, the most sensitive result is at $\theta_c = 0°.3$, where $1.1 \times 10^{-5} < \Delta T/T < 3.1 \times 10^{-5}$. We have analyzed various subsets of the data, dividing the flight into unequal quarters. The first quarter is the region near MSAM 15+82; the second, the following data up to the point where we moved off to observe the Coma Cluster, the third, the source-free data after the break; and the fourth, the data near MSAM 19+82. Table 1 gives the upper and lower limits for each quarter of the flight as well quarters 2 and 3 on which these results are based. We emphasize that our observation strategy allows for independent measurements using the single and double difference demodulations.

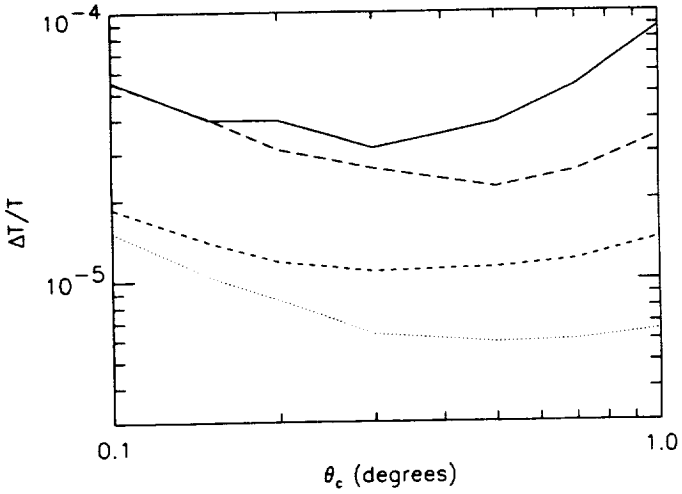

FIG. 3.—Upper and lower limits on CMBR anisotropy for Gaussian-shaped power spectra with correlation length θ_c, based on data between right ascensions $15^h.69$ and $18^h.55$. Ninety-five per cent CL upper limit for double difference (*solid*) and single difference (*long-dashed*); 95% CL lower limit for double difference (*dashed*) and single difference (*dotted*).

TABLE 1

UPPER AND LOWER BOUNDS ON CMBR ANISOTROPY

θ_c	Quarter	R.A.	Upper Bound (μK)	Lower Bound (μK)
		Single Difference		
0°.5.....	1	$14^h.44$–$15^h.69$	221	39
	2	15.69–16.89	99	...
	3	17.18–18.55	102	15
	4	18.55–18.33	221	62
	2 + 3	15.69–18.55	61	16
	All	14.44–20.33	116	53
		Double-Difference		
0.3.....	1	14.44–15.69	336	91
	2	15.69–16.89	139	33
	3	17.18–18.55	127	21
	4	18.55–20.33	121	37
	2 + 3	15.69–18.55	85	30
	All	14.44–20.33	97	50

5. CONCLUSIONS

The results from both the single- and double-difference data for this flight (decl. 82° and $15^h.69 < \text{R.A.} < 18^h.55$) show positive detections of sky brightness variations which are consistent with a CMBR spectrum. The placement of our spectral passbands allows for strong discrimination of warm Galactic dust from CMBR fluctuations, but some cold dust models at low levels are difficult to rule out. We cannot strongly rule out the spectrum of bremsstrahlung, though it is highly unlikely that that could cause a signal of the measured amplitude. Meinhold et al. (1993) have previously reported an upper limit ($\Delta T/T < 2.5 \times 10^{-5}$) at this angular scale.

The presence of the two unresolved sources in the data is clearly very interesting and could imply a significantly different scenario for CMBR anisotropy measurements on 0°.5 angular scales at the $\Delta T/T \sim 1 \times 10^{-5}$ level. If the extrapolations of Franceschini et al. (1989) are correct, then it is not likely that this detection is due to unresolved extragalactic sources. However, the two sources in these data may indicate that there is a previously unsuspected population for which neither the spatial distribution nor the spectral signature is well determined by existing data. Alternatively, if these sources are true CMBR fluctuations, then we need to investigate the compatibility of these highly peaked features with various models. Clearly, a more complete understanding of these sources is central to further improvements in sensitivity to CMBR anisotropies.

Files containing the data on which Figure 2 is based along with the antenna pattern will be made available. For information on how to obtain these data, fetch the file

/pub/data/msam-jun92/README

by anonymous FTP from cobi.gsfc.nasa.gov.

We would like to thank the staff of the National Scientific Balloon Facility in Palestine, Texas, who valiantly maintain the original can-do spirit of NASA. W. Folz provided electronics support and accompanied us on our observing run in Palestine. We would like to thank C. Lisse, J. Mather, H. Moseley, and R. Weiss for helpful discussions. The NSF Research and NASA Science Internet, which we take for granted too often, makes our long-distance collaboration possible without exorbitant expenditure of travel funds. This work made extensive use of the Free Software Foundation of Cambridge, MA. The National Aeronautics and Space Administration supports this research through grants NAGW 1841, RTOP 188-44, NGT 50908, and NGT 50720. Lyman Page is supported by a grant from the National Science Foundation.

REFERENCES

Charakhch'yan, A. N., Bazilevskaya, G. A., Stozhkov, Yu. I., & Charakhch'yan, T. N. 1978, in Cosmic Rays in the Stratosphere and in Near Space (Proc. P. N. Lebedev Physics Inst., 88) (New York: Consultants Bureau), 1
Efstathiou, G., Bond, J. R., & White, S. D. M. 1992, MNRAS, 258, 1
Franceschini, A., Toffolatti, L., Danese, L., & De Zotti, G. 1989, ApJ, 344, 35
Gorski, K. 1993, ApJ, submitted
Griffin, M. J., et al. 1986, Icarus, 65, 244
Hanel, R. A., et al. 1981, J. Geophys. Res., 86, 8705
Harwit, M. 1988, Astrophysical Concepts (2d ed.; New York: Springer-Verlag)
Kashlinsky, A. 1992, ApJ, 387, L1
Lang, K. R. 1980, Astrophysical Formulae (2d ed.; New York: Springer-Verlag)
Martin, B. R. 1971, Statistics for Physicists (London: Academic)
Meinhold, P., et al. 1993, ApJ, 409, L1
Meyer, S. S., Cheng, E. S., & Page, L. A. 1991, ApJ, 371, L7
Page, L. A. 1989, Ph.D. thesis, MIT
Page, L. A., Cheng, E. S., Golubovic, B., Gundersen, J., & Meyer, S. M. 1993, Appl. Opt., in press
Page, L. A., Cheng, E. S., & Meyer, S. S. 1990, ApJ, 355, L1
Press, W. H., et al. 1986, Numerical Recipes: The Art of Scientific Computing (Cambridge: Cambridge Univ. Press)
Smoot, G. F., et al. 1992, ApJ, 396, L1
Wheelock, S., et al. 1991, *IRAS* Sky Survey Atlas, $|\beta| > 50°$, Explanatory Booklet (Pasadena: JPL)
Wheelock, S., et al. 1993, Explanatory Supplement to the *IRAS* Sky Survey Atlas (Pasadena: JPL), in press

The Amplitude and Spectral Index of the Large Angular Scale Anisotropy in the Cosmic Microwave Background Radiation

KEN GANGA[1], LYMAN PAGE[2]

Joseph Henry Laboratories, Physics Department, Jadwin Hall, Princeton University, Princeton, NJ 08544-0708

ED CHENG

NASA/Goddard Space Flight Center, Code 685.0, Greenbelt, MD 20771

STEPHAN MEYER

Room Acc F100, Enrico Fermi Institute, University of Chicago, 5640 South Ellis Ave., Chicago, IL 60637

Received: _____; *Accepted:* _____

Abstract

In many cosmological models, the large angular scale anisotropy in the cosmic microwave background is parameterized by a spectral index, n, and a quadrupolar amplitude, Q. For a Peebles-Harrison-Zel'dovich spectrum, $n = 1$. Using data from the Far Infra-Red Survey (FIRS) and a new statistical measure, a contour plot of the likelihood for cosmological models for which $-1 < n < 3$ and $0 \leq Q \leq 50$ μK is obtained. We find that the likelihood is maximum at $(n, Q) = (1.0, 19$ μK). For constant n the likelihood falls to half its maximum at $Q \approx 14$ μK and 25 μK and for constant Q the likelihood falls to half its maximum at $n \approx 0.5$ and 1.4. Regardless of Q, the likelihood is always less than half its maximum for $n < -0.4$ and for $n > 2.2$, as it is for $Q < 8$ μK and $Q > 44$ μK.

Subject headings: cosmology: cosmic microwave background

---

[1]E-Mail: ganga@pupgg.Princeton.EDU

[2]E-Mail: page@pupgg.Princeton.EDU

1 Introduction

With the *COBE*/DMR detection of anisotropy in the cosmic microwave background radiation (CMB) (Bennett et al. 1992; Smoot et al. 1992; Wright et al. 1992), followed by the FIRS–*COBE*/DMR cross-correlation (Ganga et al. 1993) and a host of recently reported detections on smaller angular scales, we have moved from searching for the anisotropy to characterizing it.

The inflationary scenario predicts a spectrum of primordial density perturbations of form $P(k) \propto k$ for large angular scales (Steinhardt & Turner 1984), while popular variants of cold dark matter predict $P(k) \propto k^n$ with $0.7 < n < 1$ (see Turner (1993) for a review). Textures will also appear scale-invariant (i.e., $n = 1$; Pen et al. 1993), while cosmic strings may mimic an n of 1.35–1.5 (Perivolaropoulos 1993). Thus, by limiting the range of n allowed by the data we can constrain theories of structure formation. It should be pointed out, however, that many theories are not well parameterized this way (*e.g.*, Ratra & Peebles (1994)) and that in this work we consider models with *Gaussian* fluctuations only.

If one assumes this power law spectrum for density perturbations in an Einstein-DeSitter universe, then the angular power spectrum of anisotropies in the CMB is given by (Bond & Efstathiou 1987):

$$C_l = Q^2 \frac{4\pi}{5} \frac{\Gamma\big((2l+n-1)/2\big)\Gamma\big((9-n)/2\big)}{\Gamma\big((2l+5-n)/2\big)\Gamma\big((3+n)/2\big)}, \tag{1}$$

where $Q = \sqrt{5C_2/4\pi}$ is a parameter that sets the amplitude of the theoretical angular power spectrum and correlation function at the angular scale of the quadrupole. Smoot et al. (1992) use the notation Q_{rms-PS} to denote the parameter, but for the sake of brevity we follow the notation of Wright et al. (1994) and use Q. Note that Q is *not* the root-mean-squared amplitude of the quadrupole in our universe, which Bennett et al. (1994) give as 6 ± 3 μK; it is not possible to measure the intrinsic quadrupole given the limited sky coverage

of the FIRS survey. The discrepancy between values for Q quoted here and 6 ± 3 μK may be due to cosmic variance (see, for example, White, Krauss & Silk 1993 and Bond, Davis & Steinhardt 1994), but the situation is not yet clear. Note also that equation 1 does not account for microphysical process that can change the power spectrum of anisotropies and thus alter the effective n; for example, "standard" scale invariant CDM has an effective n of 1.15 for $l \lesssim 30$ (Bond 1994).

The first estimate of n using large scale CMB anisotropy data was made by fitting the theoretical auto-correlation function (ACF) derived from equation 1 directly to the auto-correlation function of the *COBE*/DMR first year data. The result was $n = 1.15^{+0.45}_{-0.65}$ and $Q = 16.3 \pm 4.6$ μK (Smoot et al. 1992). Seljak and Bertschinger (1993). using a maximum-likelihood analysis again on the first-year *COBE*/DMR data, found that $Q = (15.7 \pm 2.6) e^{0.46(1-n)}$ μK. Additionally, Smoot et al. (1994) and Torres (1994) have both done topological analyses of these data to limit n to $1.7^{+0.3}_{-0.6}$ and 1.2 ± 0.3, respectively. Bond (1994) has extracted the index from an analysis of the power spectrum of both FIRS and DMR. He finds $n = 1.8^{+0.6}_{-0.8}$ for FIRS and $n = 2.0^{+0.4}_{-0.4}$ for the first-year DMR maps. Wright et al. (1994), using a power spectrum analysis with the two year DMR maps, find $n = 1.46^{+0.41}_{-0.44}$. Bennett et al. (1994), also using the DMR two year maps, perform a maximum-likelihood analysis with Monte Carlo simulations and find $n = 1.59^{+0.49}_{-0.55}$. Finally, Górski et al. (1994) use a power spectrum based method to compute the likelihood of models. Applying it to the DMR two year data, they obtain a maximum likelihood at $(n, Q) = (1.2, 17\ \mu\text{K})$ and a maximum in the marginal likelihood for n at 1.1 ± 0.3.

This range of results, often with the same data, indicates the difficulties involved in these analyses. There is clearly a need for more data and robust statistical techniques. In this *Letter*, we describe a method for analyzing CMB anisotropy maps and apply it to the Far Infra-Red Survey (FIRS). This method uses the correlation function of anisotropy maps. Thus, it is relatively insensitive to noise contamination that can infect analyses based upon

the χ^2 or the power spectrum of a map (Bond 1994).

2 The Far Infra-Red Survey

FIRS is a balloon-borne, bolometric anisotropy experiment that observes in four channels at 170, 290, 500 and 680 GHz. It has a beam full-width-at-half-maximum (FWHM) of 3.°8 and has been flown successfully twice, resulting in coverage over most of the northern hemisphere. The data used here are from the 170 GHz channel of the October, 1989 flight and cover roughly one quarter of the sky. The data are shown in Ganga et al. (1993). The experiment and map are described more fully in Meyer et al. (1991) and Page et al. (1989, 1990, 1991, 1994).

For the purposes of this *Letter*, it is sufficient to note that the map is a set of pixels i, each with an associated residual temperature t_i and statistical weight w_i. The t_is are the average temperatures of all measurements made within pixel i after the best fit offset, dipole and Galactic model (the *IRAS* 100 μm map smeared to a 3.°8 beam width) are removed. The statistical weights are the reciprocals of the variances of the measurements for each pixel. A 15° galactic cut has been imposed on these data and on the simulations described below to minimize the effects of residual dust emission near the Galactic plane. For this analysis, we assume that all the correlations in the map are due to correlations in the CMB. In Page et al. (1994), the data reduction and known systematic errors are discussed. There are no *known* systematic effects that introduce significant correlations into the data.

3 Analysis

The correlation function of the CMB is estimated from the data with

$$C(\theta_A) = \frac{1}{\Gamma_A} \sum_{i,j \in A} w_i w_j t_i t_j, \tag{2}$$

where the sum is over all pixels i and j for which the angle between them is θ_A and where

$$\Gamma_A = \sum_{i,j \in A} w_i w_j. \tag{3}$$

$C(\theta_A)$ is presented in figure 1. The correlation function is divided into 64 2.°8 bins, of which, because these data do not cover the entire celestial sphere, only $n_c = 58$ contain data. Also, correlations for which $\theta_A = 0$ are excluded from the analysis, as they are affected most by instrumental noise.

Simulations of the sky are made for each n from 0.9 to 2.9 in steps of 0.1 following the methods of Cottingham (1987) and Boughn et al. (1993). Specifically, maps of unit amplitude are made with underlying temperatures at each pixel i defined by

$$T_i = \sum_{l=2}^{l_{max}} \sum_{m=-l}^{l} a_{l,m} \sqrt{W_l} Y_{l,m}(\theta_i, \phi_i), \tag{4}$$

where W_l is related to the Legendre transform of the experiment's beam response. If one assumes that the response is Gaussian, as we do here, then this window function can be approximated by

$$W_l = e^{-l(l+1)\sigma^2} \tag{5}$$

can be used (but see Wright et al. (1993)). With a FWHM of 3.°8, W_l falls to 1/2 at $l = 29$. For these simulations, l_{max} is 150 or the highest l for which $W_l C_l / W_2 C_2 > 10^{-7}$, whichever is lowest. Each $a_{l,0}$ is drawn from a normal distribution with a variance of $C_l/(4\pi Q^2/5)$ and for $m > 0$ both the real and imaginary parts of $a_{l,m}$ are drawn from normal distributions with variances of $C_l/(8\pi Q^2/5)$. Finally, $a_{l,-m} = (-1)^m a^*_{l,m}$. We call these signal maps. In order to include experimental uncertainties, separate noise maps are created. The temperature at each pixel i is drawn from a normal distribution with a variance of $1/w_i$. The pixels in both the signal and noise maps have the same weights as the real data. In order to match the processing done on the real data, an offset and a dipole are removed from each map separately in a least-squares fit.

Note that if the maps contain nothing but statistical noise, Γ_A is the reciprocal of the variance in bin A. That is, $\sigma^2_{C(\theta_A)} = 1/\Gamma_A$ (see Ganga et al. (1993) for a derivation and Smoot et al. (1994) for a discussion of weighting schemes for different statistics over CMB maps).

With this prescription, we form $C_{SS}(\theta)$, the ACF of a signal map, $C_{SN}(\theta)$, the cross-correlation between a signal map and its associated noise map, and $C_{NN}(\theta)$, the ACF of a noise map. We note that the full ACF of a single sky realization with a particular value of Q and noise will be

$$C(\theta) = Q^2 \frac{4\pi}{5} C_{SS}(\theta) + 2Q\sqrt{\frac{4\pi}{5}} C_{SN}(\theta) + C_{NN}(\theta). \tag{6}$$

This scaling allows one to reduce the number of simulations made, though a set of simulations at each value of n to be tested is still required.

For each simulation we make the statistic

$$R = \sqrt{\frac{1}{\sum_A \Gamma_A} \sum_A \Gamma_A \Big(C_F(\theta_A) - C_D(\theta_A)\Big)^2}, \tag{7}$$

where $C_F(\theta_A)$ is the value of the ACF of a simulation at bin A and $C_D(\theta_A)$ is the value of the ACF of the data at correlation bin A. If $R = 0$, the ACF of the simulation is the same as that of the data.

We calculate the likelihood, $P(D|n,Q)$, or the relative probability of a obtaining the FIRS data ACF given a model parametrized by n and Q, by choosing a limiting value of R and finding the number of simulations, N, for which $R < R_{lim}$. We then normalize by dividing by the maximum N for all different models, N_{max}. The *a posteriori* probability that the universe is parameterized by a certain n and Q can then be found by invoking Bayes's theorem with a suitable *a priori* probability distribution for (n, Q) (see, for example, Martin (1971)).

In essence, we are treating the correlation functions as vectors in an n_c dimensional ACF space. The various Rs represent the weighted magnitude of the difference between the data ACF vector and a simulation ACF vector. If the Γ_As were all the same, R_{lim} would define the radius of an n_c dimensional sphere centered upon the data ACF. When the Γ_A are different, the sphere is deformed into an ellipsoid. By counting the number of simulations with R less than some chosen R_{lim}, we are calculating the density of simulated ACF's in the neighborhood of the measured ACF. This density is proportional to the likelihood. The method accounts for non-uniform sky coverage, instrumental noise, cosmic variance and the effects of removing an offset and dipole from an the data.

4 Results and Discussion

Figure 2 shows the results of the analysis for $-1 < n < 3$ and $0\ \mu\mathrm{K} < Q < 50\ \mu\mathrm{K}$. In this case, $R_{lim} = 430\ \ \mu\mathrm{K}$, resulting in $N = 171$ simulations at the most likely combination of (n, Q) with $R \leq R_{lim}$. The likelihood contours for 0.05, 0.25, 0.5 and 0.75 are plotted with solid lines along with a large $\times$ at the maximum. The inner broken line in figure 2 marks the $P(D|n,Q) = e^{-1/2}$ likelihood contour, while the outer broken line corresponds to $P(D|n,Q) = 0.34$. They are shown for comparison to other analyses. If one were to extract only the $n = 1$ portion of figure 2, in the limit that the extracted likelihood is Gaussian, the $P(D|n,Q) = e^{-1/2}$ points would equal the 1σ credible limits assuming a uniform prior. The $P(D|n,Q) = 0.34$ contour represents the 68% credible limits if we use a prior of one for the models considered here and zero for all others. In other words, the the sum of the likelihoods within the 0.34 contour is 68% of the sum of all the likelihoods in figure 2.

For each model, the number of simulations within our limiting radius is governed by the binomial distribution. The probability of a particular simulation falling within the test volume is much smaller than that of it falling outside the volume. We can, therefore, ap-

proximate the variance in the estimate of the various Ns by N itself. Hence, the uncertainty in the probability for those models with $P(Q,n|D) \approx 1$ is approximately $\sqrt{2/N_{max}}$, and the error in the estimates of the likelihoods near the maximum likelihood in figure 2 is approximately 11% (with $N_{\max} = 171$). This is borne out by figure 3, which shows that the (n,Q) with the maximum likelihood depends slightly on the values of R_{lim}, but not by amounts in excess of what is expected statistically.

Bond (1994) has noted that the FIRS data contain "white noise." In principle, this noise affects only the $\theta_A = 0$ bin of the correlation function, which is not included in this analysis. To check the possibility that the noise has 'leaked' out of the zero ACF bin, the analysis was repeated after excising the bin at $\theta_A = 1.^\circ 4$ (effectively eliminating all correlations on angular scales less than $2.^\circ 8$). The results are consistent with those quoted above. If the data contained only white noise, figure 2 would have a maximum at n = 3. Clearly, it does not contaminate these results. Again, this is because this method is primarily sensitive to spatial correlations in the data.

The robustness of this method has been checked in a number of ways. Figure 3 shows that there are small changes in the likelihood contours as R_{lim} is increased. This indicates that a smaller value of R_{lim} is desirable. With this number of simulations, however, reducing R_{lim} degrades the plot to the point where it is no longer useful. ~~Note though that~~ The likelihood is stable for $n \approx 1$ and that for other n's the likelihood values are conservative (that is, the likelihood is *overestimated*).

We have also checked that changing the weighting in the definition of R does not affect the results. Redefining R such that

$$R = \sqrt{\frac{1}{\sum_A W_A} \sum_A W_A \Big(C_S(\theta_A) - C_D(\theta_A)\Big)^2}, \tag{8}$$

where W_A is now defined as 1, $\sqrt{\Gamma_A}$, Γ_A^2 or Γ_A^3 yields consistent results, though, the bounds are not as strict.

To check that this method is unbiased, the mean of 500 simulated CMB anisotropy skies with $(n, Q) = (1.0, 20\ \ \mu\mathrm{K})$ was computed. The result is $(n, Q) = (0.8, 16.5\ \ \mu\mathrm{K})$. Other values of (n, Q) have also been tested. Though this is not a rigorous test because some of the simulations would prefer an $n < -0.9$ or an $n > 2.9$, the method is unbiased to within the uncertainties in estimating the mean.

The approximation of the FIRS beam by a 3.°8 Gaussian is adequate. Results from simulations made with a Legendre transform of the measured profile do not differ substantially. If a Gaussian of width 4.°2 is assumed to account for smearing, then the value for Q at $n = 1$ increases by 1 μK.

Figure 2 implies that for the FIRS data $n \approx 1$ is favored. We point out, however, that only a fraction of the total ACF space has been tested. Many other possibilities exist. Wright et al. (1992) found the ACF of the *COBE*/DMR first-year data to be well described by a Gaussian with a coherence angle, θ_c, of 13.°5; that is, the correlation function of the DMR data was fit well by a function of form $C(\theta) = C(0)e^{-0.5(\theta/\theta_c)^2}$ with adjustments for offset and dipole removal, where $C(0)$ is the variance of the intrinsic sky fluctuation. This statistical method is well suited to testing this possibility. Retaining the normalization used in figure 2, we find the likelihood of such a model with $C(0) \approx (44\ \ \mu\mathrm{K})^2$ to be 1.4. That is, 40% more likely than the most likely model based on a power law spectrum. Thus, while $n \approx 1$ may be preferred compared to other models with a power spectrum of density perturbations that follows a power law, we are still not sure it is the best model.

Finally we note that using the FIRS data alone we cannot prove that all the correlated signal is due to the CMB. By calculation and modeling, all other known sources (galactic, instrumental, and algorithmic) of correlation can be ruled out. In addition, the FIRS autocorrelation function is like that of *COBE*/DMR, albeit not as statistically significant, and the cross-correlation with DMR is very significant. The similarity of the results from these

two independent experiments strongly suggests that the correlations in the FIRS data are due to the CMB. This method may be generalized to find the most likely (n, Q) for the FIRS/DMR cross correlation and, as noted above, to test a variety of theories. This work is underway.

5 Acknowledgements

We would like to thank Steve Boughn and Dick Bond for insights and suggestions. We also thank E. Bertschinger, D. Cottingham, K. Górski, G. Hinshaw, B. Ratra, and N. Turok for helpful comments and conversations. KMG would also like to thank Ed Hsu for insights into Monte Carlo methods. This work was supported under NASA grants NAGW-1841 and NAG5-2412, NSF grant PH 89-21378, and an NSF NYI grant to L. Page.

REFERENCES

Bennett, C.L. et al. 1992, ApJ, 396(1):L7-L12

Bennett, C.L. et al. 1994, submitted to ApJ

Bond, J.R. 1994, In *Proceedings of the 1994 Capri CMBR Conference*

Bond, J.R., Davis, R.L. & Steinhardt, P.J. 1994, Penn Preprint UPR-0604T

Bond, J.R. & Efstathiou, G. 1987, MNRAS, 226:665

Boughn, S.P. et al. 1993, ApJ, 391(2):L49-L52

Cottingham, D. 1987, PhD thesis, Princeton University

Ganga, K. et al. 1993, ApJ, 410:L57

Górski, K. et al. 1994, In preparation

Martin, B.R. 1971, *Statistics for Physicists*, Academic Press

Meyer, S.S., Cheng, E.S. & Page, L.A. 1991, ApJ, 371(1):L7–L9

Page, L.A., Cheng, E.S. & Meyer, S.S. 1991 *Applied Optics*

Page, L.A. et al. 1994, *Applied Optics*, 33(1):11–23

Page, L.A. 1989, PhD thesis, Massachusetts Institute of Technology

Page, L.A., Cheng, E.S. & Meyer, S.S. 1991 ApJ, 355(1):L1–L4

Pen, U. et al. 1993, *Princeton Observatory Preprint*; Accepted by *Physical Review D*

Perivolaropoulos, L. 1993, Center for Astrophysics preprint CfA–3796

Ratra, B. & Peebles P.J.E. 1994, Princeton University Physics preprint PUPT-1444; Submitted to *Phys. Rev. D*

Seljak, U. & Bertschinger, E. 1993, ApJ, 417(1):L9–L12

Smoot, G.F. et al 1992, ApJ, 396(1):L1–L5

Smoot G.F. et al. 1994, submitted to ApJ

Steinhardt P.J. & Turner, M.S. 1984, *Physical Review D*, 29:2162

Torres, S. 1994, ApJ, 423(1):L9–L12

Turner, M.S. 1993, FERMILAB-Conf-92/313-A

White, M., Krauss, L.M. & Silk, J. 1993, ApJ, 418(2):535–543

Wright, E.L. et al. 1992, ApJ, 396(1):L13–L18

Wright, E.L. et al. 1993, ApJ, 420(1):1–8

Wright, E.L. et al. 1994, submitted to ApJ

This manuscript was prepared with the AAS WGAS LaTeX macros v2.2

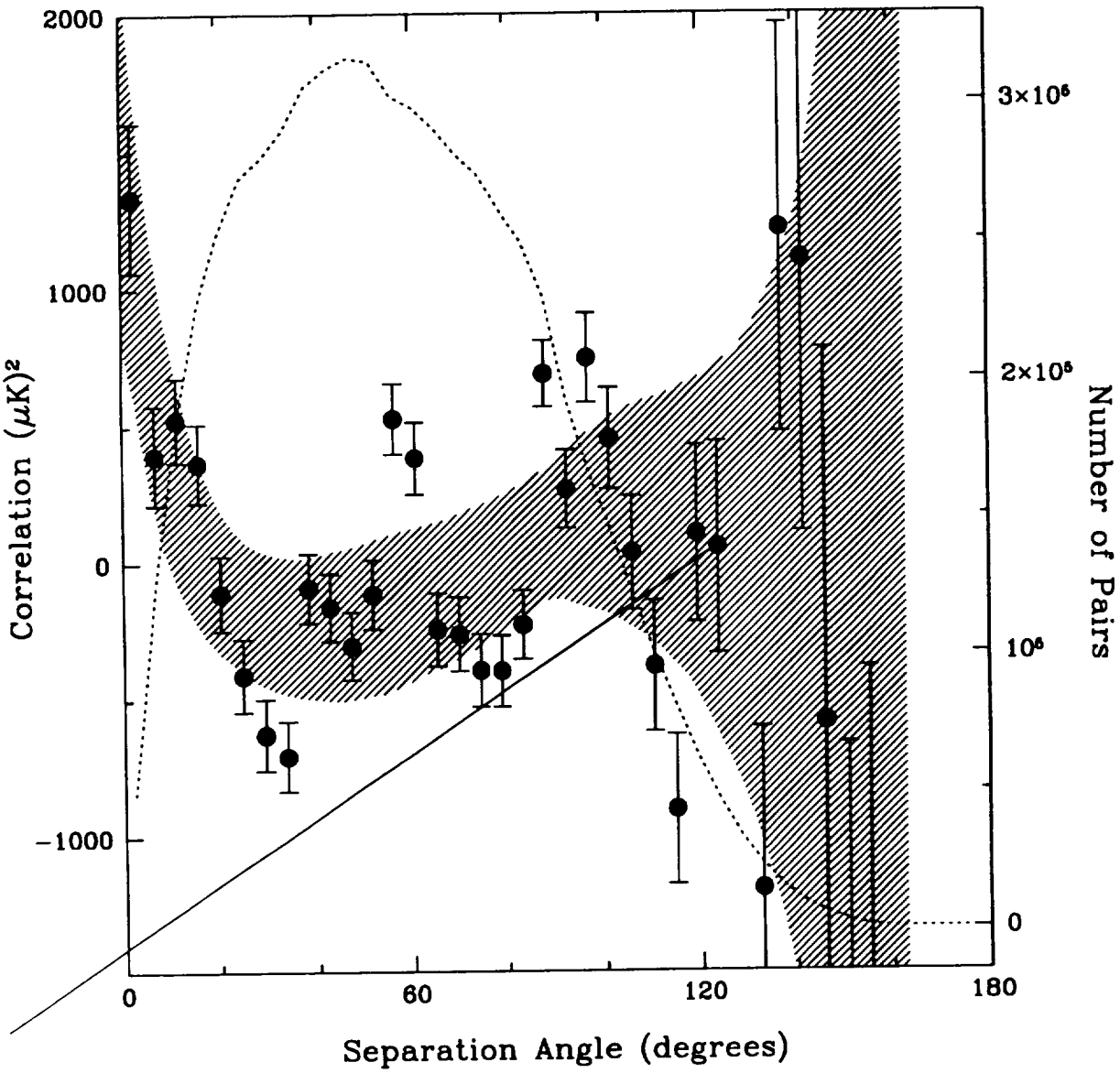

Figure 1: The FIRS auto-correlation function. The error bars represent the variations due to experimental noise only. The 180° span of θ_A is divided into 40 bins each of width 4.°5. Due to the limited sky coverage, only 36 bins contain data. The shaded area shows the *rms* in the 20000 simulated auto-correlation functions for $n = 1$ with an amplitude of $Q = 19\ \mu K$. The broken curve (corresponding to the right axis) shows the number of pairs of pixels contributing to the correlation function at each correlation function bin.

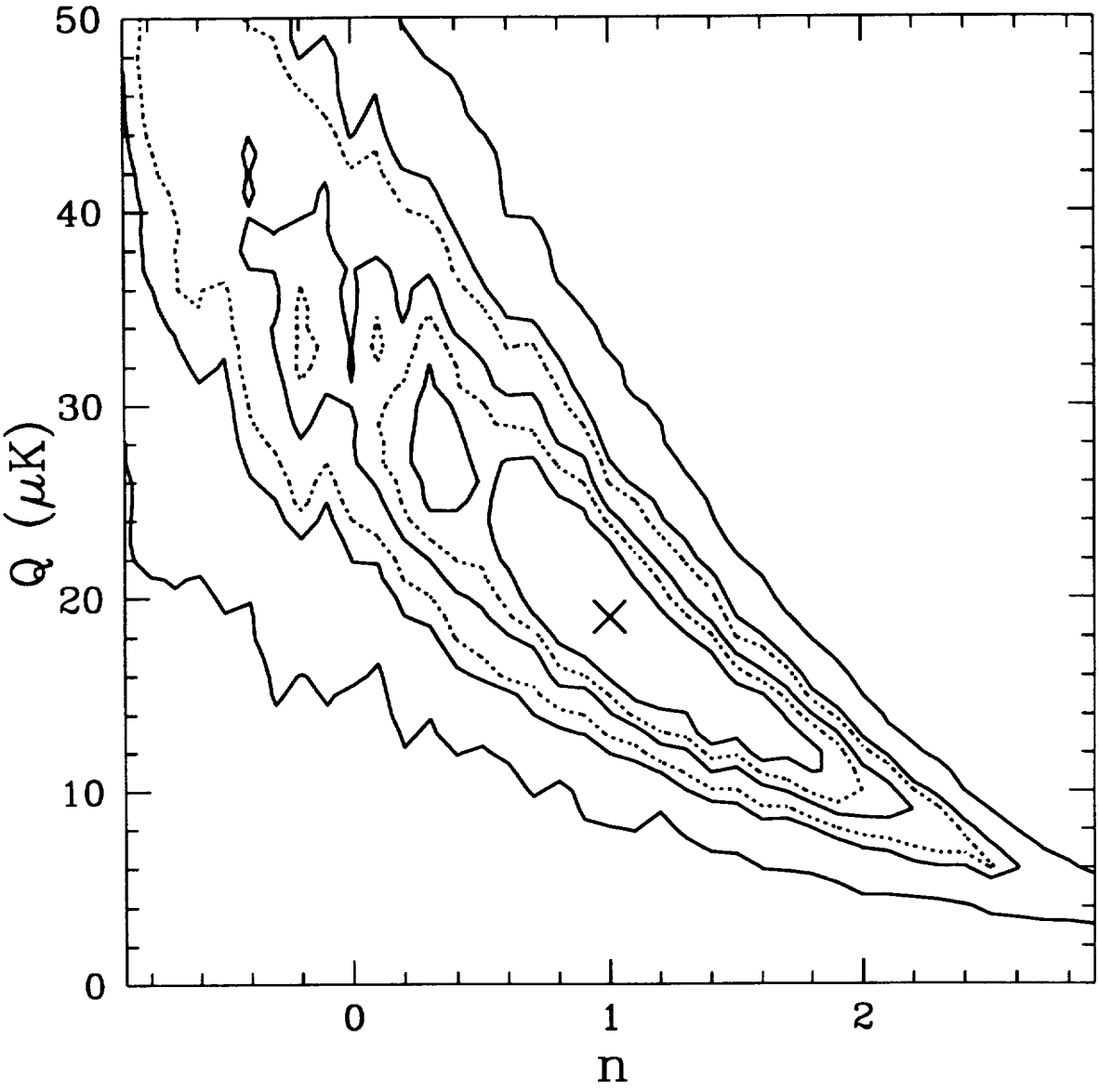

Figure 2: Likelihood contours for $R_{lim} = 430$ μK, corresponding to a maximum of 171 simulations included within the ellipse. The solid contours correspond to likelihoods of 0.05, 0.25, 0.5, and 0.75. The $\times$ at $(n, Q) \approx (1.0, 19$ μK) is the maximum and the broken lines correspond to likelihoods of 0.34 and 0.68.

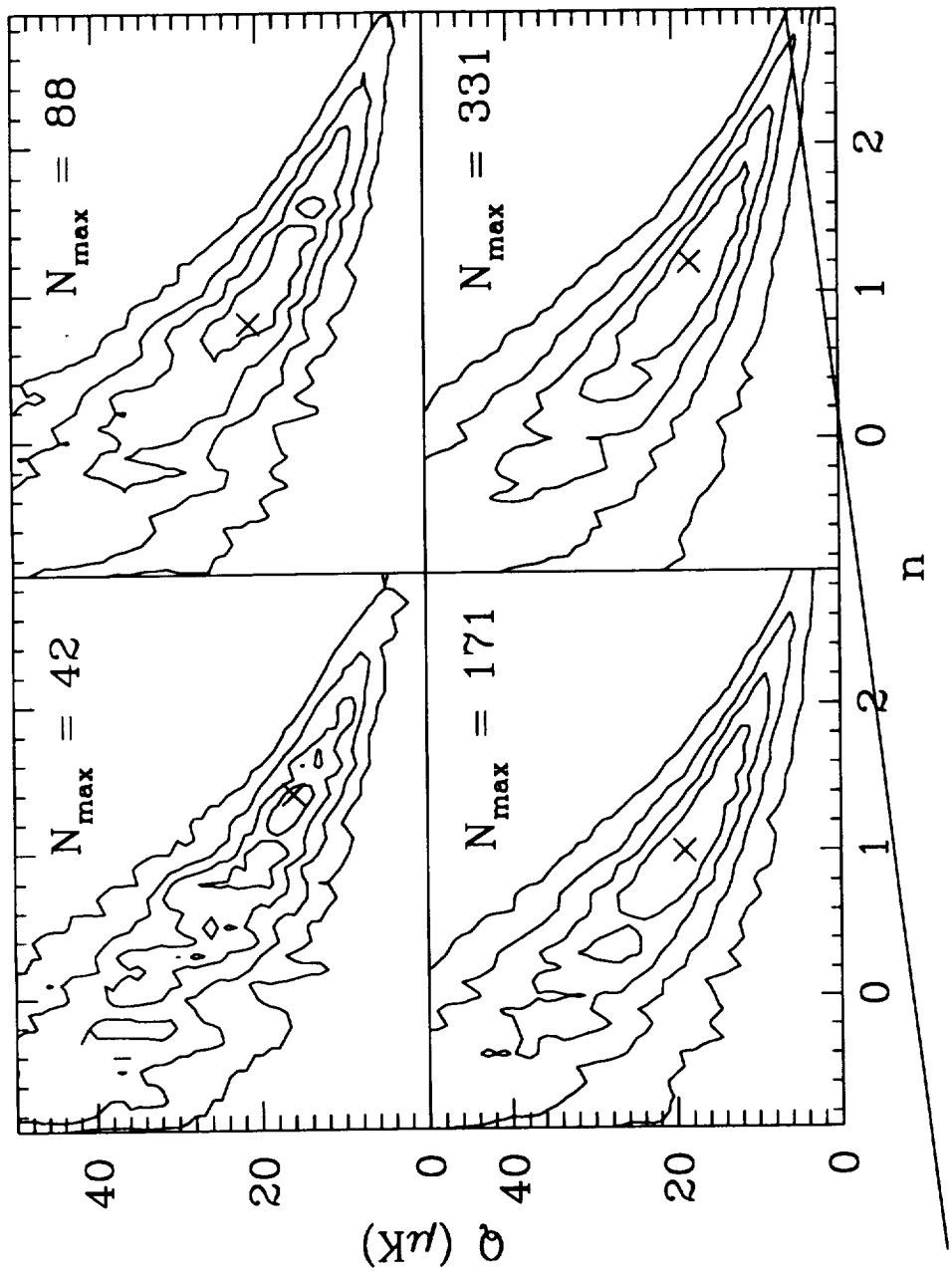

Figure 3: Likelihood contours for various values of R_{lim}. The values of R_{lim} are 410 μK, 420 μK, 430 μK and 440 μK, moving clockwise from the top left. The maximum number of simulations within the test volumes for each case is indicated on the plots.

Final report for NAGW-1841
"Astronomy In the Region Between 1mm and 0.1 mm Wavelength"

May 25, 1994

The research under this grant resulted in the measurement of anistotropy of the Cosmic Microwave Background Radiation (CMBR) on angular scales from 90 degrees to 0.3 degrees. A bolometric radiometer was built with a sensitivity of better than 500 $\mu K/\sqrt{Hz}$.

The measurements complement the COBE anisotropy measurement in two ways. The large scale measurements were shown to cross-correlate with the COBE DMR anisotropy detection, confirming the results. The small scale measurements further the understanding of the structure in the CMBR on scales where we can begin to model the early stages in galaxy and galaxy cluster formation.

No patented inventions were created under this grant.

Papers published in refereed journals are listed here.

1. "A large-Scale Cosmic Microwave Background Anisotropy Measurement At Millimeter and Submillimeter Wavelengths" L. A. Page, E. S. Cheng and S. S. Meyer. (1990) Ap. J. Lett. 355:L1

2. " A Measurement of the Large-Scale Cosmic Microwave Background Anisotropy at 1.8 Millimeter Wavelength" S. Meyer, E. Cheng and L. Page (1991) Ap J. Lett 371:L7

3. "Resonant Cryogenic Chopper" L. Page, E. Cheng and S. Meyer (1992) Appl. Optics 31,95

4. " Cross-Correlation Survey Map and the *COBE* Differential Microwave Radiometer First-Year Maps" (1993) Ap J. Lett. 410,L57

5. "Millimeter-submillimeter m" L. Page, E. Cheng, B Golubovic, J Gundersen, and S. Meyer (1994) Appl. Optics 33,11

6. " A Measurement of the Medium-Scale Anisotropy in the Cosmic Microwave Background Radiation" E. Cheng, C. Cottingham, D. Fixsen, C. Inman, M. Kowitt, S. Meyer, L. Page J. Puchalla, R. Silverberg (1994) Ap J. Lett 422,L37

7. " The Amplitude and Spectral Index of the Large Angular Scale Anisotropy in the Cosmic Microwave Background Radiation" K. Ganga, L.Page, E. Cheng, S. Meyer (1994 accepted) Ap J. Lett